

# Optimization of Type-I Clathrates for Thermoelectric Properties

by

Suk-kyung Jeung

A thesis

presented to the University of Waterloo

in fulfillment of the

thesis requirement for the degree of

Master of Science

in

Chemistry

Waterloo, Ontario, Canada, 2012

© Suk-kyung Jeung 2012

## **Declaration**

I hereby declare that I am the sole author of this thesis. This is a true copy of the thesis, including any required final revisions, as accepted by my examiners.

I understand that my thesis may be made electronically available to the public.

Suk-kyung Jeung

## Abstract

The increase in waste heat after consuming energy or burning fossil fuels is an issue environmentally and economically. Thermoelectric (TE) materials are developed to use in various applications because of their ability in converting waste heat into electricity. However, the applications are limited due to a low efficiency of materials, and research on thermoelectric materials is an on-going project for future use. Type-I clathrates are one of the TE materials which are studied in depth since the proposal of Slack's PGEC (Phonon-Glass-Electron-Crystal) concept in 1995 due to their excellent thermoelectric properties. In this study, development and optimization of quaternary type-I clathrates will be the focus because double substitution often leads to better figure-of-merit,  $ZT$ , but it hasn't really been studied. Higher  $ZT$  value is necessary because the energy conversion efficiency of TE materials is depending on the  $ZT$  value along with a larger temperature difference. Addition of lanthanoid elements as 2<sup>nd</sup> guest atoms to the main type-I clathrate structure, realized in  $\text{Ba}_8\text{Ga}_{16}\text{Ge}_{30}$ , will be attempted to form quaternary compounds. The formation of the quaternary clathrates will be analyzed through powder X-ray diffraction, single crystal analysis and energy dispersive X-ray analysis. Also, as the performance of TE materials is examined through the figure of merit,  $ZT = TS^2\sigma/\kappa$ , various techniques will be used to determine the Seebeck coefficient, the electrical conductivity and the thermal conductivity.

The quaternary clathrates,  $\text{Ba}_{8-x}\text{Ln}_x\text{Ga}_{16}\text{Ge}_{30}$  and  $\text{Ba}_{8-x}\text{Ln}_x\text{Ga}_{16+x}\text{Ge}_{30-x}$ , where Ln = La, Ce and Eu were synthesized from the pure elements in stoichiometric ratios at 1000 °C with slow cooling to room temperature. The products were then annealed at 600 °C to acquire homogeneous samples for analyses. The various compositions of lanthanoid were

intercalated into the structure of clathrates, which resulted in the quaternary clathrates with homogeneity. The crystal structure of quaternary clathrates with the space group of  $Pm\bar{3}n$  exhibited the same structure type as the ternary clathrates. The successfully formed products were refined with Rietveld refinements to understand their structures.

The Eu containing clathrates crystallized with a lattice parameter  $a = 10.78251(6)$  Å,  $V = 1253.60(2)$  Å<sup>3</sup>, for  $x = 0.3$ . The Ce containing clathrates also adopted the same space group with a lattice parameter  $a = 10.77331(6)$  Å,  $V = 1250.40(2)$  Å<sup>3</sup>, for  $x = 0.3$ . The La containing clathrates formed with a lattice parameter  $a = 10.78494(6)$  Å,  $V = 1254.45(2)$  Å<sup>3</sup>, for  $x = 0.3$ . Between 0.2 and 1.0 lanthanoid elements per formula unit were substituted with decreasing amount of barium where the actual amount of Ln in clathrates was lower than nominal amount. All these quaternary clathrates were found to be n-type semiconductors as determined through the Seebeck coefficient and electrical conductivity measurements.

**Keywords: Thermoelectric materials, Type-I clathrates, PGEC, Zintl Concept,**

## **Acknowledgements**

I would like to express my hearty gratitude to my supervisor, Prof. Holger Kleinke for his encouragement, advice and great support during the study at Waterloo. He has inspired me with the research where I can not only gain the knowledge of solid state chemistry, but also to think like a real chemist. His advice always helped me to step forward whenever there was a problem with the research.

I also want to mention about my colleagues in Kleinke's group, Abdul, Bryan, Nader, Nagaraj, Quansheng, and Savi. I always have been happy to be one of Kleinke's group, where we share memories and friendship together. I also want to thank Katja, Dr. Assoud, and Dr. Sankar for their help and support as I learned a lot from them.

I would like to thank my committee members: Professor Linda Nazar and Professor Richard Oakley for their valuable comments.

At last, I thank my family and friends for their love and support always.

Suk-kyung Jeung

# Table of Contents

Author's Declaration .....	ii
Abstract .....	iii
Acknowledgements .....	v
Table of Contents .....	vi
List of Figures .....	ix
List of Tables .....	xii
1 Introduction .....	1
1.1 Thermoelectric phenomena .....	1
1.2 Thermoelectric application .....	3
1.3 Thermoelectric efficiency and parameters involved in the research .....	6
1.3.1 Figure-of merit (ZT) and thermoelectric efficiency .....	6
1.3.2 Seebeck coefficient .....	9
1.3.3 Electrical conductivity .....	9
1.3.4 Thermal conductivity .....	10
2 Motivation and research background .....	12
2.1 Type-I clathrates .....	12
2.2 Developmements in type-I clathrates .....	18
2.3 Overview .....	21
3 Experimental techniques and physical property measurements .....	23
3.1 Synthesis .....	23
3.2 Analysis .....	24

3.2.1	Powder X-ray diffraction (XRD) analysis .....	24
3.2.2	Energy dispersive X-ray analysis (EDX) .....	29
3.2.3	Thermal analysis .....	30
3.3	Physical property measurements .....	33
3.3.1	Seebeck coefficient and electrical conductivity measurements .....	33
3.3.1	Thermal conductivity measurements .....	36
4	Preparation of new quaternary clathrate compounds: $Ba_{8-x}Ln_xGa_{16}Ge_{30}$ and $Ba_{8-x}Ln_xGa_{16+x}Ge_{30-x}$ .....	38
4.1	Syntheses and analyses .....	42
4.2	Structure and properties of $Ba_{8-x}Eu_xGa_{16}Ge_{30}$ .....	42
4.2.1	Crystal structure .....	42
4.2.2	Thermal analysis and EDX analysis .....	51
4.2.3	Physical property measurements .....	53
4.2.4	Conclusions .....	58
4.3	Structure and properties of $Ba_{8-x}Ce_xGa_{16+x}Ge_{30-x}$ .....	59
4.3.1	Crystal structure .....	59
4.3.2	Thermal analysis and EDX analysis .....	66
4.3.3	Physical property measurements .....	68
4.3.4	Conclusions .....	71
4.4	Structure and properties of $Ba_{8-x}La_xGa_{16+x}Ge_{30-x}$ .....	72
4.4.1	Rietveld refinements .....	72
4.4.2	Thermal analysis and EDX analysis .....	77

4.4.3	Physical property measurements .....	79
4.4.4	Conclusions .....	83
5	Conclusions .....	84
	Appendix A .....	87
	Bibliography .....	89



## List of Figures

Figure 1.1 Schemes of a) Peltier effect for cooling and b) Seebeck effect for power generation. ....	2
Figure 1.2 A module of thermoelectric power generator. ....	3
Figure 1.3 a) Vehicle with a thermoelectric generator device. b) A scheme of a thermoelectric generator for spacecrafts. ....	4
Figure 1.4 Typical energy path of fuel usage in vehicle. ....	5
Figure 1.5 Comparison of thermoelectric parameters, $S$ , $\sigma$ , $\kappa$ , $S^2\sigma$ , and $ZT$ . ....	7
Figure 1.6 The power generation efficiency dependence of the $ZT$ and $T_H$ based on the calculation. ....	8
Figure 2.1 The structures of individual types; a) type-I b) type-II c) type-III d) type-VIII e) type-IX f) type-X g) type-H. ....	14
Figure 2.2 The crystal structure of type-I clathrates where blue balls are host atoms and yellow balls are guest atoms. ....	17
Figure 3.1 Equipment used in the syntheses: a) an argon-filled glove box, b) programmable box furnaces with $T_{\max} = 1050^\circ\text{C}$ . ....	24
Figure 3.2 Bragg's Law – Diffraction of X-rays. ....	25
Figure 3.3 INEL XRG 3000 powder diffractometer ....	27
Figure 3.4 LEO 1530 FESEM integrated with EDX Pegasus 1200. ....	30
Figure 3.5 Scheme of DSC curve for endothermic and exothermic reactions. ....	31
Figure 3.6 NETZSCH STA 409PC Luxx differential scanning calorimetry (DSC). ....	32

Figure 3.7 ULVAC-RICO ZEM-3 for the Seebeck coefficient and the electrical conductivity measurements. ....	33
Figure 3.8 Hot pressing instrument of high temperature vacuum furnace system with 30 ton press capability by Oxy-Gon industries. ....	34
Figure 3.9 Schematic view of measuring the electrical resistivity with the dimensional parameters of a sample pellet shown. ....	35
Figure 3.10 Flash Line 3000 thermal diffusivity system under argon (ANTER Corporation, viz). ....	36
Figure 4.1 Crystal structure of $Ba_{8-x}Eu_xGa_{16}Ge_{30}$ . ....	43
Figure 4.2 Rietveld refinement of $Ba_{7.7}Eu_{0.3}Ga_{16}Ge_{30}$ . ....	44
Figure 4.3 Rietveld refinement of $Ba_{7.5}Eu_{0.5}Ga_{16}Ge_{30}$ . ....	45
Figure 4.4 Eu composition dependence of the lattice parameter $a$ (Å) of $Ba_{8-x}Eu_xGa_{16}Ge_{30}$ . ....	47
Figure 4.5 DSC curves of $Ba_{8-x}Eu_xGa_{16}Ge_{30}$ . ....	51
Figure 4.6 Electrical conductivity of $Ba_{8-x}Eu_xGa_{16}Ge_{30}$ . ....	53
Figure 4.7 Electrical conductivity of cold-pressed and hot-pressed $Ba_{7.5}Eu_{0.5}Ga_{16}Ge_{30}$ . ..	54
Figure 4.8 Seebeck coefficient of $Ba_{8-x}Eu_xGa_{16}Ge_{30}$ . ....	55
Figure 4.9 Seebeck coefficient of cold-pressed and hot-pressed $Ba_{7.5}Eu_{0.5}Ga_{16}Ge_{30}$ . ....	56
Figure 4.10 Power factor of $Ba_{8-x}Eu_xGa_{16}Ge_{30}$ . ....	57
Figure 4.11 Power factor of cold-pressed and hot-pressed $Ba_{7.5}Eu_{0.5}Ga_{16}Ge_{30}$ . ....	57
Figure 4.12 Rietveld refinement of $Ba_{7.7}Ce_{0.3}Ga_{16.3}Ge_{29.7}$ . ....	61
Figure 4.13 DSC curves of $Ba_{8-x}Ce_xGa_{16+x}Ge_{30-x}$ when $x = 0.3, 0.5, \text{ and } 1.0$ . ....	66

Figure 4.14 Electrical conductivity of $\text{Ba}_{8-x}\text{Ce}_x\text{Ga}_{16+x}\text{Ge}_{30-x}$ . .....	69
Figure 4.15 Seebeck coefficient of $\text{Ba}_{8-x}\text{Ce}_x\text{Ga}_{16+x}\text{Ge}_{30-x}$ . .....	70
Figure 4.16 Power factor of $\text{Ba}_{8-x}\text{Ce}_x\text{Ga}_{16+x}\text{Ge}_{30-x}$ . .....	71
Figure 4.17 Rietveld refinement of $\text{Ba}_{7.8}\text{La}_{0.2}\text{Ga}_{16.2}\text{Ge}_{29.8}$ . .....	73
Figure 4.18 DSC curves of $\text{Ba}_{8-x}\text{La}_x\text{Ga}_{16+x}\text{Ge}_{30-x}$ when $x = 0.3$ and $0.4$ . .....	77
Figure 4.19 Electrical conductivity of $\text{Ba}_{8-x}\text{La}_x\text{Ga}_{16+x}\text{Ge}_{30-x}$ . .....	80
Figure 4.20 Physical properties of $\text{Ba}_{7.0}\text{La}_{1.0}\text{Ga}_{17}\text{Ge}_{29}$ where a) electrical conductivity, b) Seebeck coefficient and c) power factor where $\times$ marks are reproduced data. ....	81
Figure 4.21 Seebeck coefficient of $\text{Ba}_{8-x}\text{La}_x\text{Ga}_{16+x}\text{Ge}_{30-x}$ . .....	82
Figure 4.22 Power factor of $\text{Ba}_{8-x}\text{La}_x\text{Ga}_{16+x}\text{Ge}_{30-x}$ . .....	83
Figure A.1 The electrical conductivity of $\text{Ba}_{8-x}\text{Ln}_x\text{Ga}_{16}\text{Ge}_{30}$ and $\text{Ba}_{8-x}\text{Ln}_x\text{Ga}_{16+x}\text{Ge}_{30-x}$ . ....	87
Figure A.2 The Seebeck coefficient of $\text{Ba}_{8-x}\text{Ln}_x\text{Ga}_{16}\text{Ge}_{30}$ and $\text{Ba}_{8-x}\text{Ln}_x\text{Ga}_{16+x}\text{Ge}_{30-x}$ . ....	88
Figure A.3 The power factor of $\text{Ba}_{8-x}\text{Ln}_x\text{Ga}_{16}\text{Ge}_{30}$ and $\text{Ba}_{8-x}\text{Ln}_x\text{Ga}_{16+x}\text{Ge}_{30-x}$ .....	88

## List of Tables

Table 2.1 Polyhedra forming clathrates. ....	16
Table 2.2 $ZT_{max}$ values of various type-I clathrates .....	19
Table 2.3 Physical properties ( $S$ , $\sigma$ , and $\kappa$ ) at room temperature for different Ba <sub>8</sub> Ga <sub>16</sub> Ge <sub>30</sub> samples along with the sample type. ....	20
Table 4.1 Refinement details of Ba <sub>8-x</sub> Eu <sub>x</sub> Ga <sub>16</sub> Ge <sub>30</sub> when x = 0.2, 0.3 and 0.4. ....	46
Table 4.2 Refinement details of Ba <sub>8-x</sub> Eu <sub>x</sub> Ga <sub>16</sub> Ge <sub>30</sub> when x = 0.5, and 1.0. ....	46
Table 4.3 Atomic coordinates, equivalent thermal displacement parameters and occupancy factors of Ba <sub>7.54(1)</sub> Eu <sub>0.46(1)</sub> Ga <sub>16</sub> Ge <sub>30</sub> . ....	48
Table 4.4 Atomic coordinates, equivalent thermal displacement parameters and occupancy factors of Ba <sub>7.54(1)</sub> Eu <sub>0.46(1)</sub> Ga <sub>16</sub> Ge <sub>30</sub> . ....	49
Table 4.5 Selected interatomic distances [ $\text{\AA}$ ] of Ba <sub>8-x</sub> Eu <sub>x</sub> Ga <sub>16</sub> Ge <sub>30</sub> . ....	50
Table 4.6 Atomic percentages of elements from EDX data for Ba <sub>7.5</sub> Eu <sub>0.5</sub> Ga <sub>16</sub> Ge <sub>30</sub> . ....	52
Table 4.7 Average element composition of the Ba <sub>8-x</sub> Eu <sub>x</sub> Ga <sub>16</sub> Ge <sub>30</sub> compounds. The actual composition was obtained by EDX analysis. ....	52
Table 4.8 Refinement details of Ba <sub>7.7</sub> Ce <sub>0.3</sub> Ga <sub>16.3</sub> Ge <sub>29.7</sub> and Ba <sub>7.0</sub> Ce <sub>1.0</sub> Ga <sub>17.0</sub> Ge <sub>29.0</sub> . ....	61
Table 4.9 Atomic coordinates, equivalent thermal displacement parameters and occupancy factors of Ba <sub>7.7</sub> Ce <sub>0.3</sub> Ga <sub>16.3</sub> Ge <sub>29.7</sub> . ....	62
Table 4.10 Atomic coordinates, equivalent thermal displacement parameters and occupancy factors of Ba <sub>7.0</sub> Ce <sub>1.0</sub> Ga <sub>17.0</sub> Ge <sub>29.0</sub> . ....	63
Table 4.11 Selected interatomic distances [ $\text{\AA}$ ] of Ba <sub>8-x</sub> Ce <sub>x</sub> Ga <sub>16+x</sub> Ge <sub>30-x</sub> . ....	64
Table 4.12 Atomic percentages of elements from EDX data for Ba <sub>7.5</sub> Ce <sub>0.5</sub> Ga <sub>16.5</sub> Ge <sub>29.5</sub> . ..	67

Table 4.13 Average element composition of the $\text{Ba}_{8-x}\text{Ce}_x\text{Ga}_{16+x}\text{Ge}_{30-x}$ compounds. The actual composition was obtained by EDX analysis. ....	67
Table 4.14 Refinement details of $\text{Ba}_{7.8}\text{La}_{0.2}\text{Ga}_{16.2}\text{Ge}_{29.8}$ and $\text{Ba}_{7.7}\text{La}_{0.3}\text{Ga}_{16.3}\text{Ge}_{29.7}$ . ....	74
Table 4.15 Atomic coordinates, equivalent thermal displacement parameters and occupancy factors of $\text{Ba}_{7.8}\text{La}_{0.2}\text{Ga}_{16.2}\text{Ge}_{29.8}$ . ....	74
Table 4.16 Atomic coordinates, equivalent thermal displacement parameters and occupancy factors of $\text{Ba}_{6.85(1)}\text{Eu}_{1.20(1)}\text{Ga}_{16}\text{Ge}_{30}$ . ....	75
Table 4.17 Selected interatomic distances [ $\text{\AA}$ ] of $\text{Ba}_{8-x}\text{La}_x\text{Ga}_{16+x}\text{Ge}_{30-x}$ when $x = 0.2$ and $0.3$ . ....	76
Table 4.18 Atomic percentages of elements from EDX data for $\text{Ba}_{7.7}\text{La}_{0.3}\text{Ga}_{16.3}\text{Ge}_{29.7}$ . ...	78
Table 4.19 Average element composition of the $\text{Ba}_{8-x}\text{La}_x\text{Ga}_{16+x}\text{Ge}_{30-x}$ compounds. The actual composition was obtained by EDX analysis. ....	78

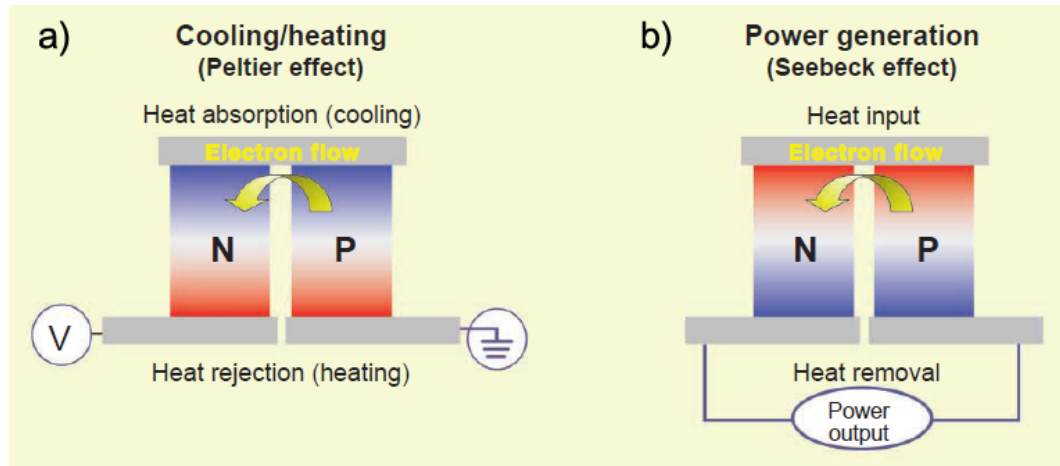
# **1 Introduction**

Currently, energy is one of the biggest issues economically and environmentally. Approximately 60% of produced energy via natural resources such as burning fossil fuels is lost through waste heat, while the consumption of energy kept increasing globally.<sup>1, 2</sup> Thermoelectric technology, which provides a potential method for converting waste heat into electricity, can be applied to various fields such as automobiles, and manufacturing plants.<sup>2,3</sup> Moreover, materials which show the thermoelectric effect have a great potential in extensive use for Peltier coolers and heating devices, and successful replacement can save fossil fuels and reduce green house emission.<sup>2</sup>

## **1.1 Thermoelectric phenomena**

Thermoelectric concepts are described using three identified effects: the Seebeck effect, the Peltier effect and the Thomson effect. The concept of thermoelectric was first brought up by Estonian-German physicist, Thomas Johann Seebeck in 1821, which was later named as the Seebeck effect.<sup>4</sup> Seebeck discovered that an electrical voltage was formed with changing temperature across a metal when he saw a deflection of a compass needle while a closed loop was formed between the junctions of metals in changing temperature.<sup>5</sup> After the Seebeck effect was defined, French physicist Jean C. A. Peltier identified the reverse of Seebeck effect in 1834 that two different metals joined in a circuit were heated or cooled at each junction of two metals when a current flew.<sup>5</sup> The schematic drawings of both Seebeck effect and Peltier effect are shown in Figure 1.1.<sup>6</sup> Later in 1851, William Thomson found that any current-carrying conducting materials under a temperature difference between two points causes both heat and electrical flow between the

points.<sup>5</sup> This phenomenon was defined to be the Thomson effect.



**Figure 1.1 Schemes of a) Peltier effect for cooling and b) Seebeck effect for power generation.<sup>6</sup>**

Thermoelectric (TE) phenomena of above-mentioned effects became important in generating electricity. The application using thermoelectric materials could be a great way of converting waste heat, generated from home usage to industrial usage, into electricity, which would save energy and environment.

## 1.2 Thermoelectric application

A typical thermoelectric application can be found in a thermoelectric power generator as shown in Figure 1.2.<sup>7</sup> As can be seen in Figure 1.2, a device is with TE couples consisting of two different conducting materials, negative charge carriers (with free electrons) and positive charge carriers (with free holes) covered with ceramic plates to absorb heat. The mobile charge carriers tend to diffuse from the hot end to cold end, therefore, charge carriers build up at the cold end to produce an electrostatic potential, and there will be a flow to reach equilibrium within the device.<sup>6-9</sup> By applying a temperature difference, a heat flow across this device where the top plate absorbs and rejected via

bottom plate after generating electrical current through the external circuit.<sup>6-9</sup>

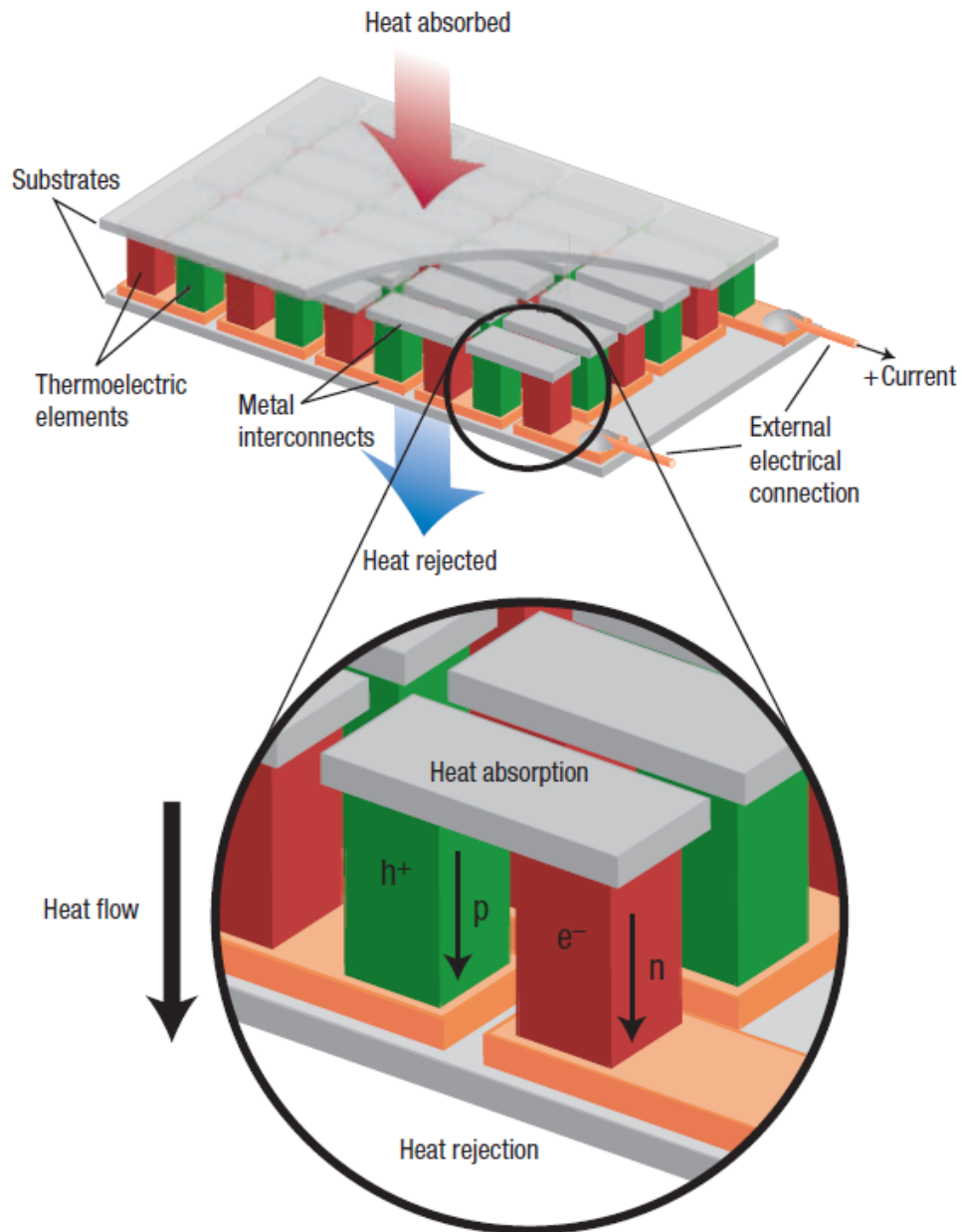


Figure 1.2 A module of thermoelectric power generator.<sup>7</sup>



Moreover, the application of TE material is not just limited to a simple TE module, which can be used in a refrigerator, but also for automobiles and spacecraft.<sup>10-12</sup> (Fig. 1.3) Some automobile companies such as GM<sup>10</sup> and BMW<sup>12</sup>, and NASA<sup>10-11</sup> have been working on applying TE phenomena to increase the efficiency of energy use which are lost through waste heat.

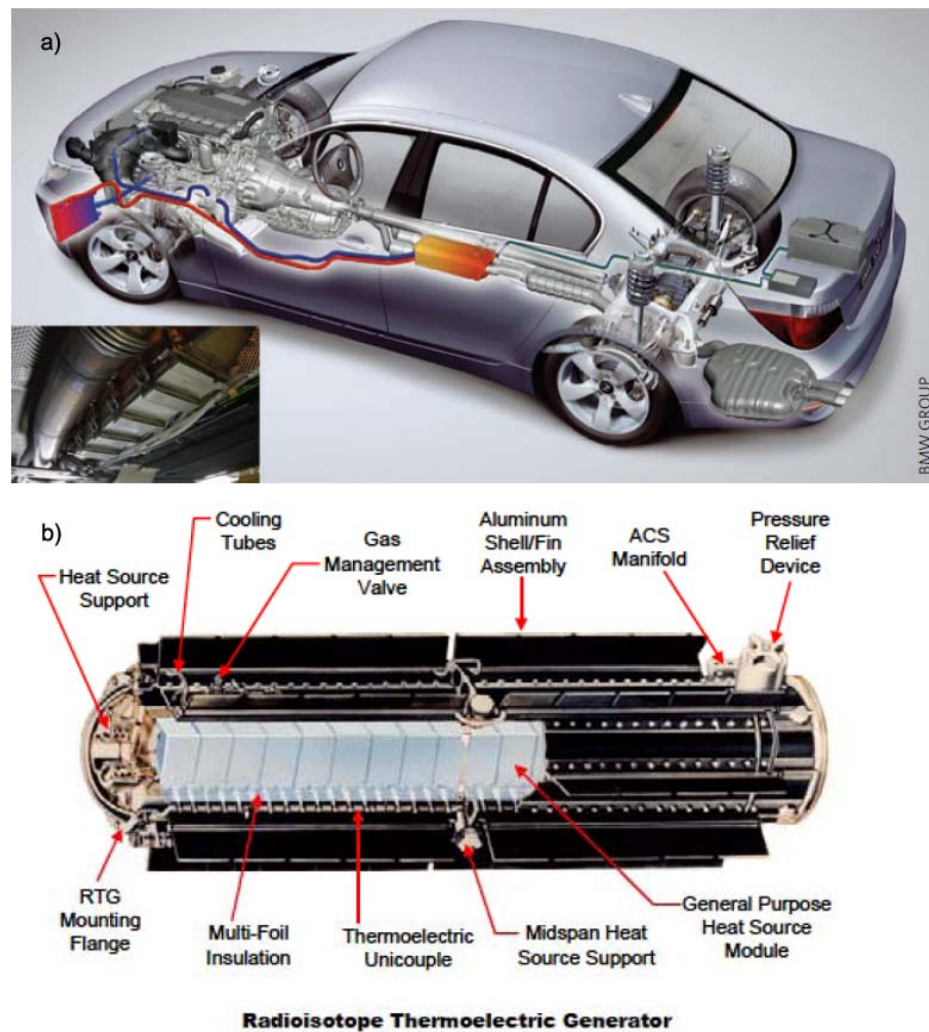


Figure 1.3 a) Vehicle with a thermoelectric generator device.<sup>12</sup> b) A scheme of a thermoelectric generator for spacecrafts.<sup>11</sup>

Figure 1.4<sup>10</sup> clearly illustrates how much of energy from gasoline fueled vehicle is used for mobility, and surprisingly only 25% of total energy is used while the rest of energy being lost in a form of waste heat through various reasons such as exhaust gas, coolant, and other resistances. A huge amount of energy losses may be necessary, but not efficient. Industry has achieved 5% conversion efficiency through using TE generator, and is targeting to achieve 10% fuel reduction by optimizing materials and changing critical conditions.<sup>10</sup> Not only TE generators decrease a reduction of energy usage, but they are also reliable, scalable, reasonable in size, and making no noise or vibration. While automobile companies interested in using TE generator device to recover waste heat to increase the fuel efficiency, the U.S. space program, NASA is using radioisotope thermoelectric generators known as RTGs (Fig. 1.3 b)) to generate electrical power from waste heat in spacecrafts.<sup>10-11</sup> The difference of RTG from a general thermoelectric generator is that the waste heat is released from the nuclear decay of radioactive isotopes,<sup>10-</sup>  
<sup>11</sup> The conversion efficiency of RTGs is about 6%.<sup>10-11</sup>

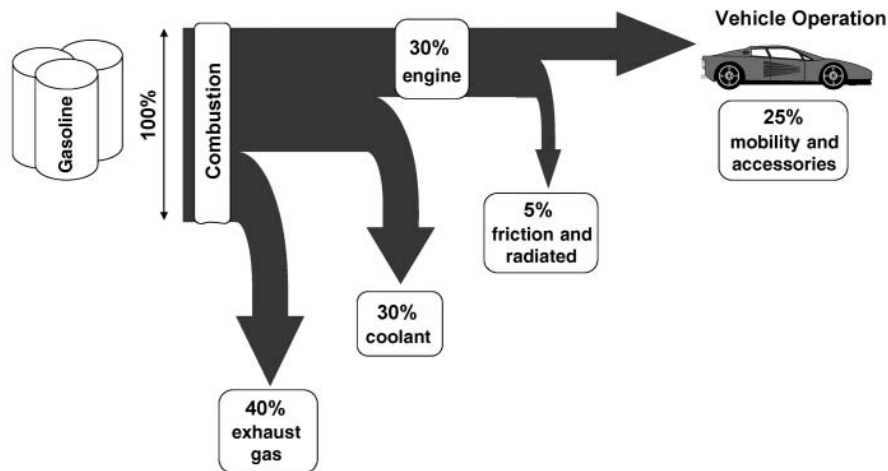


Figure 1.4 Typical energy path of fuel usage in vehicle.<sup>10</sup>

### 1.3 Thermoelectric efficiency and parameters involved in the research

The efficiency of TE materials is the most important to be considered in a field of TE research as it is the key point to determine whether the material can be adapted to a real life or not. There are various parameters involved in determining the efficiency such as figure-of-merit ( $ZT$ ), the Seebeck coefficient ( $S$ ), the electrical conductivity ( $\sigma$ ), the thermal conductivity ( $\kappa$ ), and the power generation efficiency ( $\eta$ ). Among those parameters, the one is expecting to achieve maximum  $ZT$  with a large Seebeck coefficient and electrical conductivity while the thermal conductivity stays as low.

#### 1.3.1 Figure-of-merit ( $ZT$ ) and thermoelectric efficiency

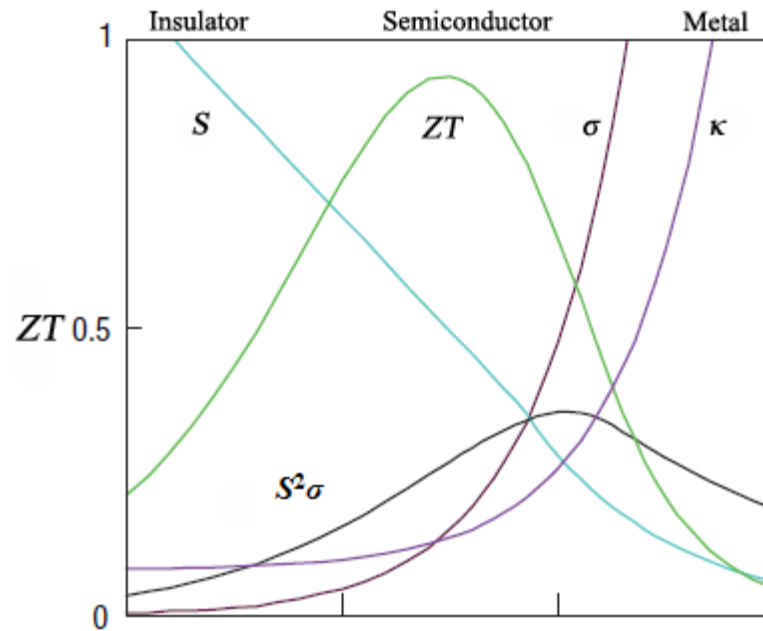
The performance of thermoelectric materials can be evaluated (analyzed) using relationships between various parameters to form a dimensionless figure-of-merit ( $ZT$ ) which is defined to be the following,

$$ZT = \frac{S^2 \sigma T}{\kappa} \quad (1.1)$$

where  $S$  is the Seebeck coefficient,  $\sigma$  is the electrical conductivity,  $\kappa$  is the thermal conductivity, and  $T$  is the average absolute temperature of hot and cold side respectively.<sup>1-10,</sup>

<sup>15</sup> The relationship between parameters can be seen from the definition of  $ZT$  that high values of the Seebeck coefficient and electrical conductivity along with low thermal conductivity are required to achieve maximum  $ZT$ .

The following figure (Fig. 1.5) depicts overall relation comparison of thermoelectric parameters, which can also demonstrates the properties of different types of material; insulator, semiconductor and metal.



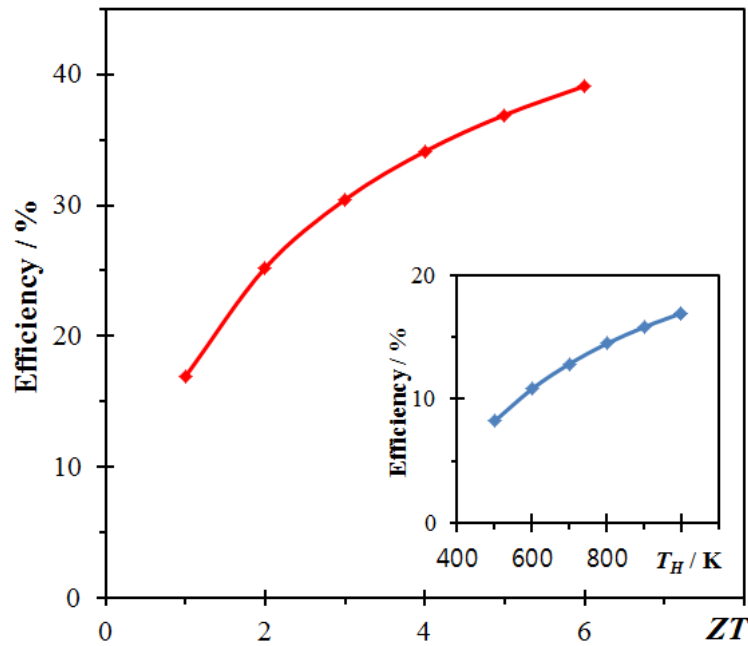
**Figure 1.5 Comparison of thermoelectric parameters,  $S$ ,  $\sigma$ ,  $\kappa$ ,  $S^2\sigma$ , and  $ZT$ .<sup>21</sup>**

Insulators are not good to be used as TE material as shown in figure 1.5 that they have a poor electrical conductivity despite of high Seebeck coefficient. Metals are also not good either even with a high electrical conductivity because they have a high thermal conductivity and low Seebeck coefficient which will decrease the performance of TE material. This leaves semiconductors to be considered. The peak of  $S^2\sigma$  indicates that semiconductor will be an excellent candidate for TE material with a maximum  $ZT$  value among other.

While the dimensionless figure-of-merit,  $ZT$  determines the performance of TE materials, the power generation efficiency,

$$\eta = \frac{T_H - T_C}{T_H} \cdot \frac{\sqrt{1 + ZT} - 1}{\sqrt{1 + ZT} + T_C/T_H} \quad (1.2)$$

is used to calculate the efficiency of the generating device where  $T_H$  and  $T_C$  are the temperatures of hot side and cold side respectively. In order to acquire high power generation efficiency, definitely, a high  $ZT$  value is required. Figure 1.6 illustrates the relationship between the power generation efficiency versus  $ZT$ , and the power generation efficiency versus  $T_H$  when  $T_C$  is assumed to be 300K and  $ZT$  remains as 1. The calculation used in Figure 1.6 is based on the Equation (1.2).



**Figure 1.6 The power generation efficiency dependence of the  $ZT$  and  $T_H$  based on the calculation.**

The graph of power generation efficiency depending on the  $ZT$  was calculated between the temperature of 300 and 100K that the power generation efficiency increases with increasing  $ZT$ .

### **1.3.2 Seebeck coefficient**

The Seebeck coefficient of a material is also known as thermopower which was briefly mentioned with a Figure 1.5 in a previous page. When the material is being heated, carriers (electrons-negative charges or holes-positive charges) migrate from the hot side to cold side,<sup>6, 19</sup> causing an increase of the thermoelectric voltage.<sup>6</sup> The Seebeck coefficient is the measurement of an induced voltage magnitude over a temperature in difference of the material with a unit of volts per Kelvin (V/K). However, the unit of microvolts per Kelvin ( $\mu\text{V/K}$ ) will be used in this thesis.

By doping or substituting, the Seebeck coefficient can be optimized through creating extrinsic semiconductors with either donor or acceptor elements to obtain a large value of  $S$ . Thermoelectric material with negative charge carriers causes negative Seebeck coefficient, and TE material with holes causes positive Seebeck coefficient where 150-250  $\mu\text{V/K}$  will be a desirable range to be observed.

### **1.3.3 Electrical conductivity**

The electrical conductivity ( $\sigma$ ) represents the behavior of charge carriers in a compound where a high and reasonable value is needed to acquire desired TE material because electrical conductivity is proportional to the Seebeck coefficient and overall,  $ZT$ , the performance of the material from the definition. The electrical conductivity is not

directly measured, but acquired from the electrical resistivity ( $\rho$ ) where  $\sigma$  is the inverse of  $\rho$ . The electrical conductivity has a unit of  $\Omega^{-1}\text{cm}^{-1}$ .

$$\sigma = \frac{1}{\rho} \quad (1.3)$$

The conductivity of semiconducting TE materials is generally intermediate, but it may vary depending on degrees of doping as impurity of material leads to a higher electrical conductivity. Also  $\sigma$  is highly dependent on the band gap of the material where semiconductor exhibits a narrow or small band gap because electrons are the only available carriers with enough thermal energy for excitation across the band gap.<sup>19</sup> However, this band gap energy tends to decrease with increasing temperature<sup>19</sup>, and this is why doping (introducing impurities) or displacement of guest atoms is necessary because it will build a heat resistivity with a high melting point by adjusting band gaps.

#### 1.3.4 Thermal conductivity

While both  $S$  and  $\sigma$  are expected to show high values, the thermal conductivity ( $\kappa$ ) has to stay low as possible. Thermal conductivity is the measurement of the heat transfer with the unit of Watts per meter per Kelvin ( $\text{Wm}^{-1}\text{K}^{-1}$ ). Thermal conductivity is consisting of two factors, the electronic thermal conductivity ( $\kappa_e$ ) of an electron or a hole transporting, and the lattice thermal conductivity ( $\kappa_l$ ) of phonon transporting as shown in Equation (1.4). The electronic thermal conductivity can be calculated with the Lorenz number ( $L$ ),  $2.44 \times 10^{-8} \text{ W}\Omega\text{K}^{-2}$  for free electron as defined in Equation (1.5) by Wiedemann-Franz law, which can later be used to find  $\kappa_l$  by substituting back into Equation (1.4) with measured thermal conductivity. The total thermal conductivity equation is described in Equation (1.6) with  $\alpha$

thermal diffusivity ( $\text{cm}^2/\text{s}$ ),  $\rho$  density of the sample ( $\text{g}/\text{cm}^3$ ) and  $C_p$  the heat capacity ( $\text{J}/\text{g}\cdot\text{K}$ ).

Thermal diffusivity is a measured parameter.

$$\kappa = \kappa_e \text{ (electron or hole carrier)} + \kappa_l \text{ (phonon carrier)} \quad (1.4)$$

$$\kappa_e = L\sigma T \quad (1.5)$$

$$\kappa = \alpha\rho C_p \quad (1.6)$$

Achieving a low thermal conductivity without changing electrical conductivity significantly is important to acquire a high thermoelectric performance. Many TE research works have been focusing on optimizing thermal conductivity to obtain lowest possible value for  $\kappa$ , but the task is very challenging to be achieved because most of  $\kappa$  is coming from electronic thermal conductivity. The lattice thermal conductivity of semiconductors depends on the type of dopant or substituting atoms because scattering of phonon charge carrier is coming from dopants. A typical range of thermal conductivity for a good thermoelectric material is  $0.25 - 0.5 \text{ Wm}^{-1}\text{K}^{-1}$ .



## 2 Motivation and research background

Even though thermoelectric materials were discovered long ago, the development and application of the materials were slow in process due to their low efficiency. However, the application of thermoelectric materials has been of great interest since the development of the phonon-glass-electron-crystal (PGEC) concept by Slack in 1995.<sup>13-15</sup> Slack proposed in his concept that a good thermoelectric material should conduct heat like a glassy material, and electricity like a crystal.<sup>9, 13</sup> A random substitution of other atoms in a pre-existed semiconducting material creates disorder causing inharmonic phonon scattering, which can reduce thermal conductivity without affecting electrical conductivity. Since then, researchers have studied how to obtain high efficient thermoelectric materials including type-I clathrates wherein guest atoms are encapsulated in a cage “rattle” to lower the electronic thermal conductivity ( $\kappa_e$ ) more.<sup>1-3, 19, 26</sup> This concept is also explained by using the relationship between parameters determining dimensionless Figure of Merit (in Section 1.3), which is used to evaluate the efficiency of TE materials.

### 2.1 Type-I clathrates

The first introduction of clathrates (compounds consisting of a cage structure that traps guest atoms or molecules.) was reported by Davy about 200 years ago,<sup>13</sup> and the X-ray crystal structure was later discovered by Pauling in 1935.<sup>18</sup> Hydrated clathrates are water-based solids trapping gases such as methane or carbon dioxide to form cage structures, found as naturally occurring compounds at the ocean floor and in the ice-cores of the Arctic and Antarctic.<sup>19</sup> The purpose of studying clathrates in the beginning was to find the capacity of clathrate hydrates to store large volumes of gas.<sup>13, 20-21</sup> Further studies

on clathrate hydrates found that they are taking a role in climate change such as global warming because of their encapsulated methane.<sup>21-24</sup> Methane is a greenhouse gas, which is directly related to global warming in the present. Ever since the discovery of the capacity of clathrate hydrates causing global warming as there are huge amounts existing in the artic, the research work is more focused on the structure trapping of the gases. There are total seven different classified structures discovered up to present. Types I - VII were first found in hydrated clathrates, and there are type VIII and IX were discovered later.<sup>19, 25-26</sup> Figure 2.1 demonstrates the crystal structures of various classified clathrates with different types of polyhedra.

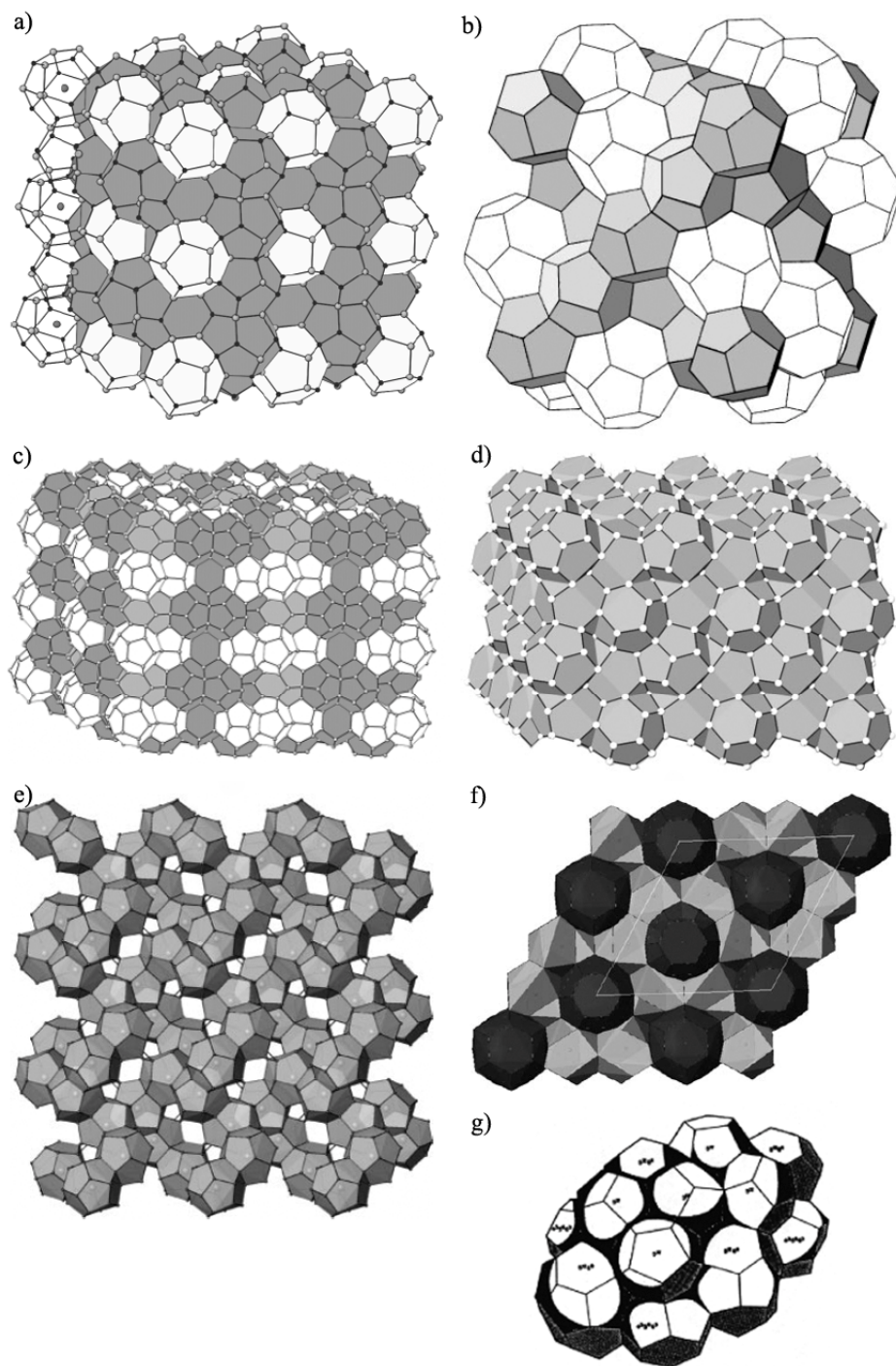
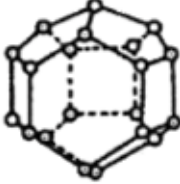
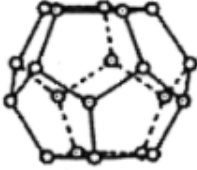
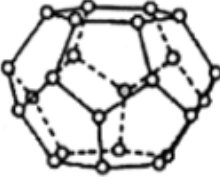

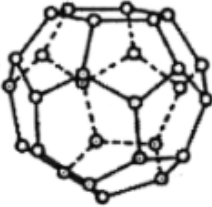
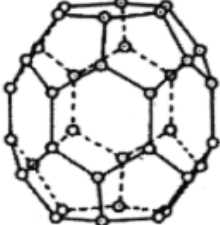


Figure 2.1 The crystal structures of individual types; a) type-I<sup>26</sup> b) type-II<sup>32</sup> c) type-III<sup>26</sup> d) type-VIII<sup>26</sup> e) type-IX<sup>26</sup> f) type-X<sup>33</sup> g) type-H<sup>17</sup>.

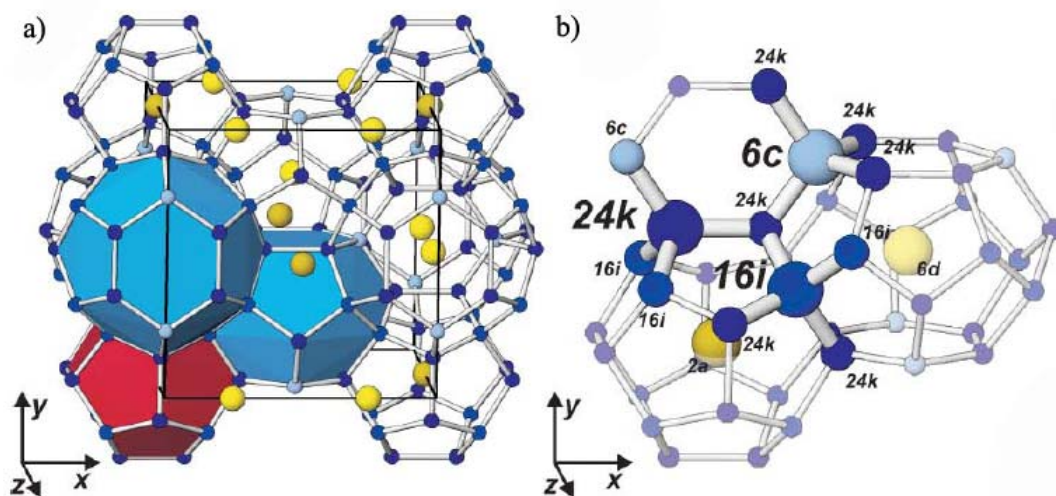
Strong interests in structure of clathrate hydrates as the cage can encapsulate atoms in contrast to zeolite have extended the research on inorganic clathrates. Among different types of classified structures of clathrate hydrates, only type-I form is considered as potential material in thermoelectric studies.<sup>19, 27-28, 31</sup> Inorganic type-I clathrates are composed of the host atoms from the groups 13 and 14, transition metal and the guest atoms from the group 2 elements, where the formula of the compounds can generally be  $A_8M_{16}X_{30}$  with A = Sr, Ba; M = Al, Ga; and X = Ge, Sn, space group  $Pm\bar{3}n$ .<sup>1-3, 15, 19</sup> The host atoms of M and X form two pentagonal dodecahedron cages and six larger tetrakaidecahedron cages (Table 2.1) per unit cell to encapsulate the guest atoms near the cage centres.<sup>1-3, 19</sup>

**Table 2.1 Polyhedra forming clathrates.**<sup>17, 26</sup>

Name	Graphical representation	Notation	Observed in clathrates
Irregular dodecahedron		$[4^3 5^6 6^3]$	H
Pentagonal dodecahedron		$[5^{12}]$	I, II, III, VIII, <sup>a</sup> IX, H
Tetrakaidecahedron		$[5^{12} 6^2]$	I, III, X
Pentakaidecahedron		$[5^{12} 6^3]$	III
Hexakaidecahedron		$[5^{12} 6^4]$	II
Icosahedron		$[5^{12} 6^8]$	H

<sup>a</sup> Distorted pentagonal dodecahedra for the type-VIII clathrate.

As the type-I clathrate is in cubic system,  $a$ ,  $b$ , and  $c$  axes have the same length, namely 10.785(2) Å in case of  $\text{Ba}_8\text{Ga}_{16}\text{Ge}_{30}$  reported by Chakoumakos *et al.*<sup>34</sup> The crystal structure of type-I clathrates can be seen in Figure 2.2 a). Figure 2.2 b) illustrates the occupancies of composed atoms where the host atoms occupies on the  $6c$ ,  $16i$  and  $24k$  positions while the guest atoms occur on the  $2a$  and  $6d$  position.<sup>13, 19</sup>



**Figure 2.2 The crystal structure of Type-I clathrates where blue balls are host atoms and yellow balls are guest atoms.**<sup>13, 19</sup>

The stoichiometry of the clathrate I is governed by the Zintl-Klemm rule<sup>2</sup> where the electropositive guest atoms donate their valence electrons to the electronegative host structure.<sup>2, 15, 19, 29</sup> As host atoms are tetrahedrally bonded, four electrons are needed for each host atom in the unit cell of the type-I clathrate.<sup>19, 29</sup> There are 46 host atoms present in the unit cell, and thus  $4 \times 46 = 184$  electrons must be present to form four bonds for each host atom in the unit cell to fulfill the octet rule. Moreover, while host atoms form covalent bonds, the host-guest interactions are presumed to be ionic.<sup>19, 29</sup>

## 2.2 Developments in type-I clathrates

The studies on inorganic type-I clathrate compounds have started from the formula,  $A_8(M, X)_{46}$  where A is the cationic guests of the group 1 or group 2 from elements of the group 13 and 14 to form frameworks; A = Na, K, Ba and M, X = Al, Ga, In, Si, Ge, Sn.<sup>1</sup> The most well studied compounds in the last few years are  $Sr_8Ga_{16}Ge_{30}$  and  $Ba_8Ga_{16}Ge_{30}$  because they have the ideal number of 184 valance-electrons according to the Zintl-Klemm rule of electron counting.<sup>1-2, 15, 19</sup> Ever since Nolas *et al.*<sup>31</sup> first reported on  $Sr_8Ga_{16}Ge_{30}$  as a possible thermoelectric material with an estimated  $ZT$  value exceeding 1.0 above 700 K, various compositions of type-I clathrates have been studied. However,  $ZT$  of  $Sr_8Ga_{16}Ge_{30}$  cannot exceed 1.0 as demonstrated by Cao *et al.*<sup>37</sup>, so they doped the framework with In to achieve  $ZT= 0.72$  at 800 K. On the other hand, Saramat *et al.*<sup>38</sup> have used the Czochralski method to grow a crystal of  $Ba_8Ga_{16}Ge_{30}$  which attained  $ZT = 1.35$  at 900 K, and could possibly reach 1.63 at 1100 K by extrapolation.  $ZT$  values of  $Ba_8Ga_{16}Ge_{30}$  also varied depending on the method and condition as Fujita *et al.*<sup>39</sup> reported 0.62 at 800 K, Toberer *et al.*<sup>40</sup> 0.8 at 1050 K with a polycrystalline sample, and Hou *et al.*<sup>41</sup> 0.93 at 850 K with a single crystal.

Reported high  $ZT$  values of other type-I clathrates are 0.87 at 870 K for  $Ba_8Ga_{16}Si_{30}$ ,<sup>42</sup> 1.03 at 943 K for  $Ba_8Ga_{10}In_6Ge_{30}$ ,<sup>43</sup> 0.61 at 760 K for  $Ba_8Ga_{16}Al_3Ge_{27}$ ,<sup>44</sup> 0.98 at 1000 K for  $Ba_8Ni_{0.32}Ga_{13.63}Ge_{31.71}$ <sup>2</sup> and 1.2 at 1000 K for  $Ba_8Ni_{0.31}Zn_{0.52}Ga_{13.06}Ge_{32.2}$ .<sup>2</sup> In the past, the optimization of the material was been more concentrated on doping the frameworks rather than tackling the guest atoms. Modification of the guest atoms, not only varying the types of elements, but double filling with two

different guest atoms can improve the performance of clathrates by lowering the thermal conductivity. Tang *et al.*<sup>3</sup> have demonstrated double atom fillings on Ge-based clathrates achieving the maximum  $ZT$  value of 1.09 for  $\text{Ba}_{7.5}\text{Yb}_{0.5}\text{Ga}_{16}\text{Ge}_{30}$  at 950 K. Two different cationic guest atoms, Ba and Yb, allegedly occupy the same sites without any detected. In Table 2.2, various type-I clathrate compounds along with the highest  $ZT$  values are presented.

**Table 2.2  $ZT_{\max}$  values of various type-I clathrates**

Compound (type)	$ZT_{\max}$	$T_{\max}$ (K)
$\text{Ba}_8\text{Ga}_{16}\text{Ge}_{30} (n)^{38}$	1.35	900
$\text{Ba}_8\text{Ga}_{16}\text{Ge}_{30} (n)^{41}$	0.93	850
$\text{Ba}_8\text{Ga}_{16}\text{Si}_{30} (n)^{42}$	0.87	873
$\text{Ba}_8\text{Al}_{16}\text{Ge}_{30} (n)^{45}$	0.24	800
$\text{Ba}_{7.5}\text{Yb}_{0.5}\text{Ga}_{16}\text{Ge}_{30} (n)^3$	1.09	950
$\text{Ba}_8\text{Ga}_{16}\text{Al}_3\text{Ge}_{27} (p)^{44}$	0.61	763
$\text{Ba}_8\text{Cu}_6\text{Si}_{17}\text{Ge}_{23} (n)^{46}$	0.31	520
$\text{Ba}_8\text{Ga}_{10}\text{In}_6\text{Ge}_{30} (n)^{43}$	1.03	943
$\text{Ba}_8\text{Ni}_{0.32}\text{Ga}_{13.63}\text{Ge}_{31.71} (n)^2$	0.98	1000
$\text{Ba}_8\text{Ni}_{0.31}\text{Zn}_{0.52}\text{Ga}_{13.06}\text{Ge}_{32.2} (n)^2$	1.2	1000
$\text{Sr}_8\text{Ga}_{15.5}\text{In}_{0.5}\text{Ge}_{30} (n)^{37}$	0.72	800

Even though, many of the above mentioned clathrates exhibit high  $ZT$  values, other physical properties such as the Seebeck coefficient, the electrical conductivity and the thermal conductivity can be quite different. For example for  $\text{Ba}_8\text{Ga}_{16}\text{Ge}_{30}$  the Seebeck coefficient, the electrical conductivity and the thermal conductivity of the material with the highest  $ZT$  values range from -42 to -175  $\mu\text{V}\cdot\text{K}^{-1}$ , from 1500 to 600  $\Omega^{-1}\text{cm}^{-1}$ , and from 1.85



to  $1.25 \text{ W}\cdot\text{m}^{-1}\text{K}^{-1}$  for 300 to 900 K respectively (Table 2.3).<sup>38</sup> Moreover,  $\text{Ba}_{7.5}\text{Yb}_{0.5}\text{Ga}_{16}\text{Ge}_{30}$  exhibits  $S = -60 \text{ }\mu\text{V}\cdot\text{K}^{-1}$ ,  $\sigma = 1030 \text{ }\Omega^{-1}\text{cm}^{-1}$  and  $\kappa = 1.5 \text{ W}\cdot\text{m}^{-1}\text{K}^{-1}$  at 300 K, and  $S = -198 \text{ }\mu\text{V}\cdot\text{K}^{-1}$ ,  $\sigma = 530 \text{ }\Omega^{-1}\text{cm}^{-1}$  and  $\kappa = 1.13 \text{ W}\cdot\text{m}^{-1}\text{K}^{-1}$  at 950 K.<sup>3</sup> However, there has been a doubt on the data.<sup>1, 55, 58</sup> The Seebeck coefficient of  $\text{Ba}_8\text{Ga}_{16}\text{Si}_{30}$  is  $-47 \text{ }\mu\text{V}\cdot\text{K}^{-1}$ ,<sup>42</sup> of  $\text{Sr}_8\text{Ga}_{16}\text{Ge}_{30}$   $-70 \text{ }\mu\text{V}\cdot\text{K}^{-1}$ <sup>42</sup> or  $-156 \text{ }\mu\text{V}\cdot\text{K}^{-1}$ <sup>31</sup>, of  $\text{Ba}_8\text{Ga}_{16}\text{Al}_3\text{Ge}_{27}$ <sup>44</sup>  $190 \text{ }\mu\text{V}\cdot\text{K}^{-1}$  and of  $\text{Sr}_8\text{Ga}_{15.5}\text{In}_{0.5}\text{Ge}_{30}$ <sup>37</sup>  $-80 \text{ }\mu\text{V}\cdot\text{K}^{-1}$  at room temperature. Typical values for the electrical conductivity are of the order of  $10^3 \text{ }\Omega^{-1}\text{cm}^{-1}$ , and for the thermal conductivity is below  $2 \text{ W}\cdot\text{m}^{-1}\text{K}^{-1}$ .

**Table 2.3 Physical properties ( $S$ ,  $\sigma$ , and  $\kappa$ ) at room temperature and maximal  $ZT$  values for different  $\text{Ba}_8\text{Ga}_{16}\text{Ge}_{30}$  samples along with the sample type.**

Sample type	$S$ ( $\mu\text{V}\cdot\text{K}^{-1}$ )	$\sigma$ ( $\Omega^{-1}\text{cm}^{-1}$ )	$\kappa$ ( $\text{W}\cdot\text{m}^{-1}\text{K}^{-1}$ )	$ZT_{\text{max}}$
Crystal <sup>38</sup>	-42	1500	1.85	1.35
Crystal <sup>41</sup>	-40	1770	2.19	0.93
Polycrystalline <sup>47</sup>	-90	320	1.30	0.65
Polycrystalline <sup>43</sup>	-70	714	2.10	0.50
Powder <sup>48</sup>	-40	683	1.00	0.03
Pellet <sup>48</sup>	-79	133	1.00	0.04

### 2.3 Overview

Research on prospective thermoelectric (noting as TE) materials focuses on finding a material with a high thermoelectric figure-of-merit, noting that it is difficult to control and enhance electrical conductivity and thermopower while keeping the thermal conductivity as low as possible.<sup>2</sup> The maximum  $ZT$  value of the clathrates studied to date remains a slightly above one, even though clathrates exhibit very low thermal conductivity values compared to other semiconducting thermoelectric materials due to inclusion of guest atom A in a framework of cages formed by M and X atoms.

In order to increase the efficiency of the clathrates, the host frameworks of type-I clathrates have been optimized by doping or changing the composition host atoms to achieve the maximum performance as numeric values of physical properties are discussed in section 2.2. The efforts on those modifications did not yield major improvements. Later, the study has moved on to quaternary compounds, especially to substitution of additional second guest atoms into the original clathrates. The thermal conductivity of polycrystalline type-I clathrates which are substituted with Eu is lower than that of Sr substituted ternary clathrates.<sup>50</sup> A report by Cohn *et al.*<sup>51</sup> indicates that the heavier elements and double atom fillings comprises a good concept to lower the lattice thermal conductivity. A high  $ZT$  value was observed for using Yb as a second guest atom along with Ba. The advantages of substituting lanthanide series as second elements are similar size as Ba with more electrons (so one can modify carrier concentration), heavier than Ba (thus generally lower thermal conductivity, especially when mixed with Ba), and lanthanoid with a higher periodic number has electrons in  $f$  orbitals to possibly give higher thermopower.<sup>3</sup> As no

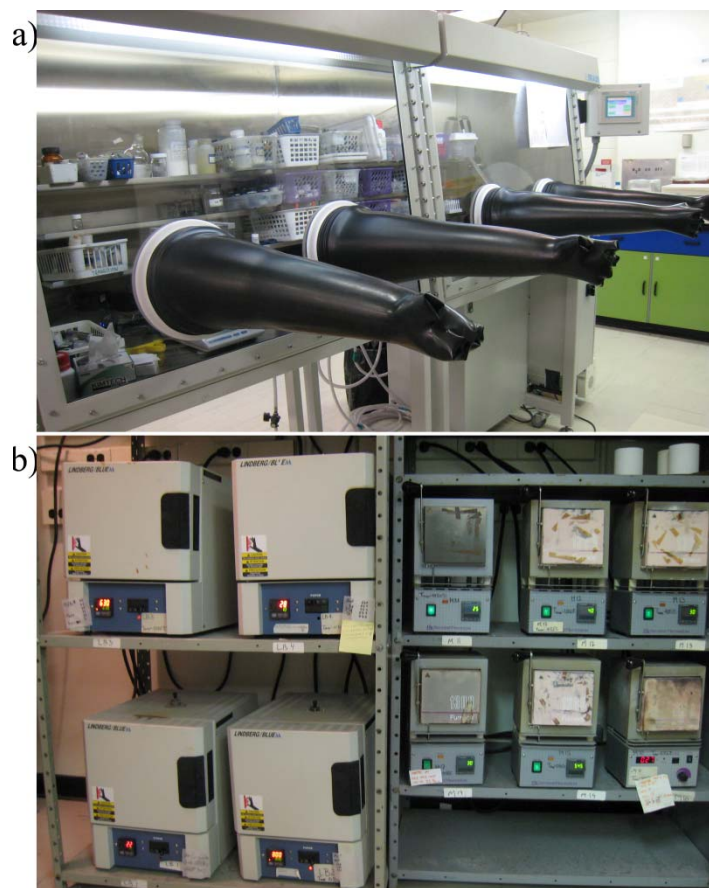
comprehensive work has been done on quaternary clathrates, substitution of an element from lanthanoid as second guest atom will be performed to acquire a high electrical conductivity along with thermopower while lowering thermal conductivity. The continuous change of Ba/lanthanoid (guest atoms) will give variations in the structural and physical properties, and will ideally lead towards finding new quaternary clathrates with excellent thermoelectric parameters.

The research of this thesis was concentrated on developing homogeneous quaternary systems from ternary systems of clathrates via adding lanthanoids. Not many elements were used from the lanthanoid to study as thermoelectric materials in the past, so it was a challenge to develop such compounds with trivalent lanthanoids. In this thesis, I successfully synthesized quaternary type-I clathrates with a formula of  $\text{Ba}_{8-x}\text{Ln}_x\text{Ga}_{16+x}\text{Ge}_{30-x}$  for  $\text{Ln}^{3+}$ , and  $\text{Ba}_{8-x}\text{Ln}_x\text{Ga}_{16}\text{Ge}_{30}$  for  $\text{Ln}^{2+}$ . As type-I clathrates are considered to be Zintl compounds, 184 electrons must be present as there are 46 host atoms in the unit cell.<sup>15, 19, 29</sup> Therefore, the stoichiometric formula for quaternary compound also followed the rule of electron counting.<sup>29</sup> Various syntheses were performed to form homogeneous quaternary compounds, and the products were analyzed by powder X-ray diffraction (XRD) and energy dispersive X-ray (EDX) analysis for finding their purity, structural, and compositional information. Moreover, physical properties,  $S$ ,  $\sigma$  and  $\kappa$  of successfully formed compounds were measured using the ULVAC ZEM-3 and the Anter Flashline 3000 on both cold-pressed and hot-pressed annealed pellets. Unfortunately, the thermal conductivity of several samples was not measured due to instrumental problem.

### **3 Experimental techniques and physical property measurements**

#### **3.1 Synthesis**

Type-I clathrate compounds are prepared from the stoichiometric amounts of high purity elements (Alfa Aesar, 99.99%; Sigma Aldrich , 99.9%). These elements are weighed in an argon-filled glove box (Figure 3.1 a)), as they are sensitive to oxygen, followed placing them in a carbon crucible before putting them into silica tubes for sealing. Before taking the tubes out of the glove box, they are closed with vacuum-tight valves, and then they are placed under a vacuum line for evacuation until the pressure reaches around  $1 - 3 \times 10^{-3}$  mbar. The tubes are then sealed and placed in programmable box furnaces (Figure 3.1 b)) for various heating and cooling programs in order to obtain the desired compounds. The high melting point of germanium (one of the elements used) of 945°C suggests using 1000 °C as the maximum temperature, to ensure melting of all components, followed by with slow cooling for formation of a crystalline product. However, the synthesis conditions are optimized to obtain the desired materials quantitatively. Finally, the samples are ground before any analyses such as powder X-ray diffraction analysis, energy dispersive X-ray analysis, thermal analysis and other physical property measurements.



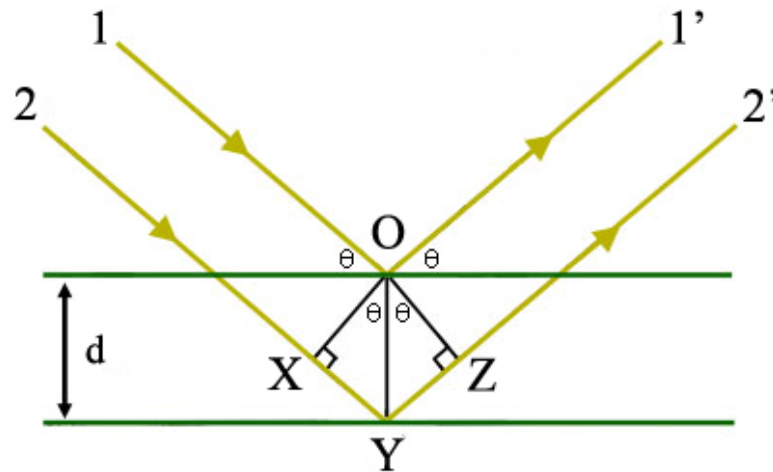
**Figure 3.1 Equipment used in the syntheses: a) an argon-filled glove box, b) programmable box furnaces with  $T_{\max} = 1050^{\circ}\text{C}$ .**

## **3.2 Analysis**

### **3.2.1 Powder X-ray diffraction (XRD) analysis**

After synthesis, the samples are routinely evaluated using powder X-ray diffraction analysis for phase purity and structural verification. Diffraction patterns of samples are then compared with known phases through using programs containing databases such as ICSD (the inorganic crystal structure database) and ICDD (the international center for diffraction data). In this research, WPA<sup>60</sup> and MATCH<sup>61</sup> are used.

In order to use x-rays for diffraction, x-rays generated by the bombardment of an anode metal such as Cu with electrons are monochromatized before striking the crystalline sample using a filter or monochromator.<sup>49</sup> As every crystal has its own pattern of oriented repeating unit cells, when a beam of monochromatic x-rays strikes the planes of atoms within the crystal, the x-rays are then reflected (or scattered) from the planes (Figure 3.2) to form diffraction patterns in respect to the source and detector,<sup>53, 62</sup> and therefore, can be distinguished one from another.<sup>59</sup> X-ray diffraction (XRD) patterns are made through accumulating intensities and angles of the diffracted radiation.



**Figure 3.2 Bragg's Law – Diffraction of X-rays.**

Incident beams of x-rays, 1 and 2 strike adjacent planes A and B in a crystal separated by a distance with  $d$  where beams can be reflected to give scattered x-rays of 1' and 2' if they are in phase. The result of reflected rays is called the constructive interference. When the radiation is being reflected, the path difference XYZ equals to  $n\lambda$  as reflected beams are at certain  $\lambda$  while x-ray beams are generated in a range of  $\lambda$ .<sup>63</sup>

Considering  $\angle XOY = \angle ZOY = \theta$

$$d \sin \theta = XY \text{ and } d \sin \theta = ZY,$$

therefore,  $XY = ZY$ .

$$2 XY = 2 d \sin \theta \text{ and } n\lambda = XYZ,$$

$$n\lambda = 2 d \sin \theta \tag{3.1}$$

The last equation is known as Bragg's law where  $d$  represents the distance between two adjacent planes in a crystal, and  $\theta$  is the angle of incidence.<sup>62, 64</sup> The process of acquiring a good diffraction pattern involves the number of electrons interacting with x-rays that more electrons cause stronger scattering.

The efficiency in scattering x-rays correlates with the scattering factor,  $f$  as expressed in Equation (3.2).

$$f = \frac{\text{Amplitude of wave scattered by an atom}}{\text{Amplitude of wave scattered by an electron}} \tag{3.2}$$

As each atom in a crystal scatters the x-rays, each peak from a diffraction pattern of intensity vs.  $2\theta$  corresponds to specific positions of atoms sitting on a particular plane ( $hkl$ ). This combined wave scattered by all the atoms in a unit cell on the plane ( $hkl$ ) is defined as the structure factor  $F(hkl)$  expressed in Equation (3.3). The structure factor depends on the position ( $x_j, y_j, z_j$ ) and the scattering factors of the atoms.

$$F(hkl) = \sum f_j \exp [2\pi i (hx_j + ky_j + lz_j)] \tag{3.3}$$

This finding contributed to possible investigation of various crystal structures and

developing X-ray diffraction. Even though, the PXRD (defines powder X-ray diffraction) cannot detect impurities of less than 5%, it is still very useful to check yields. Unlike for a single crystal, X-ray diffraction analysis, a polycrystalline powder sample is used for the PXRD where a large number of lattice planes of  $(hkl)$  with the angle  $\theta$  exist for scattering. Therefore, powder X-ray diffraction is one of the commonly used techniques to study structural information of a crystalline compound. An INEL XRG 3000 powder diffractometer with position-sensitive detector shown in figure 3.3 is used for the analysis.



**Figure 3.3 INEL XRG 3000 powder diffractometer**

As the project is on modifying ternary type-I clathrate compounds with lanthanoids to form new quaternary products, the detailed information of created polycrystalline samples are studied via X-ray diffraction analysis and Rietveld refinements as its diffraction pattern shares the same with the ternary compounds. Thus both Le Bail and



Rietveld refinement methods are used to acquire the detailed structural information such as lattice parameter, atomic position and other parameters.

Le Bail method is a simpler method than Rietveld refinement which can be used to determine the unit cell size, but they are not accurate enough for thorough understanding of the sample.

Rietveld refinement is first developed for refining crystal structures from neutron diffraction patterns,<sup>65-69</sup> and then extended to powder X-ray diffraction patterns.<sup>67</sup> This method is based on refining profiles while comparing with the proposed structural model of reference. Also setting constraints are used for atoms sharing the same position to determine the occupancy of each atom sharing the same position. Rietveld refinements are similar to Le Bail method that profiles and parameters are refined according to the manual,<sup>68</sup> and the atomic position along with a lattice parameters can be determined. The GSAS (general structure analysis system)<sup>69</sup> program is used for conducting the Rietveld refinements.<sup>65-66</sup> In order to run GSAS program diffraction pattern was collected for over 15 hours.

### 3.2.2 Energy dispersive X-ray analysis (EDX)

Energy dispersive X-ray spectroscopy is a technique for both qualitative and quantitative analysis of samples. The elements can be identified, and the elemental composition can be determined. This technique is used in conjunction with scanning electron microscope (SEM).

The characteristic x-rays are emitted from the sample when a beam of high energy strikes the surface of materials to eject a core electron of the atoms from the inner. This creates a hole and the energy difference between the higher energy level from outer shell and the lower energy level from inner shell is released in the form of x-rays when an electron from the outer shell fills this hole.<sup>70</sup> Emitted x-rays have their own characteristics which will then be interpreted in the form of spectrum for identification. Moreover, the integration of the area under the peaks of each element present gives the composition of each element in the sample in percentage, which can then be used to determine the stoichiometry of the sample. The numeric values which are obtained through this technique may not be precise enough. LEO 1530 FESEM integrated with EDX Pegasus 1200 in the Department of Chemistry at the University of Waterloo is used for the EDX analysis. (Figure 3.4) A typical range of 20-25 k eV is used as an electron beam.



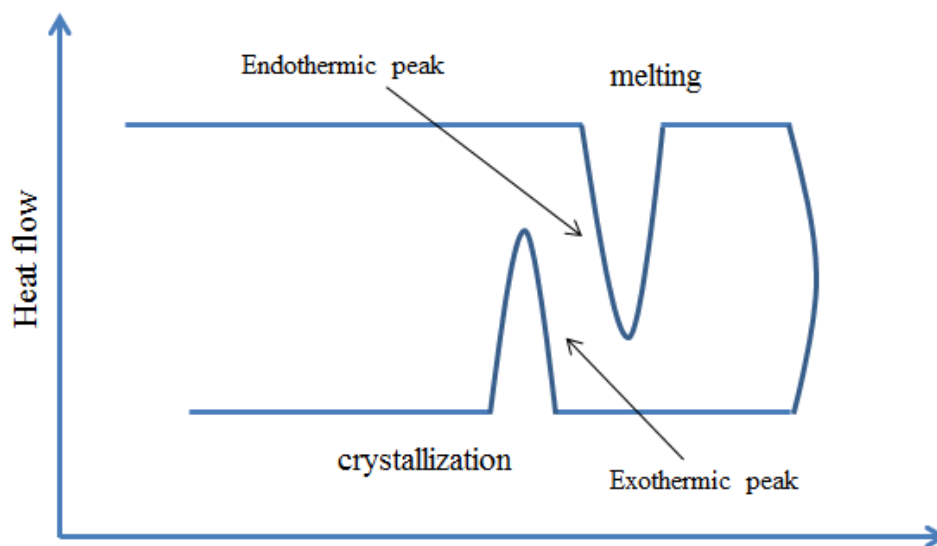
**Figure 3.4 LEO 1530 FESEM integrated with EDX Pegasus 1200.**

### **3.2.3 Thermal analysis**

Thermal analysis is used to investigate the thermal stability of a sample by employing differential scanning calorimetry (DSC) along with thermogravimetry (TG). Differential scanning calorimetry is a thermoanalytical technique which was developed by E. S. Watson and M. J. O'Neill in 1960.<sup>62</sup>

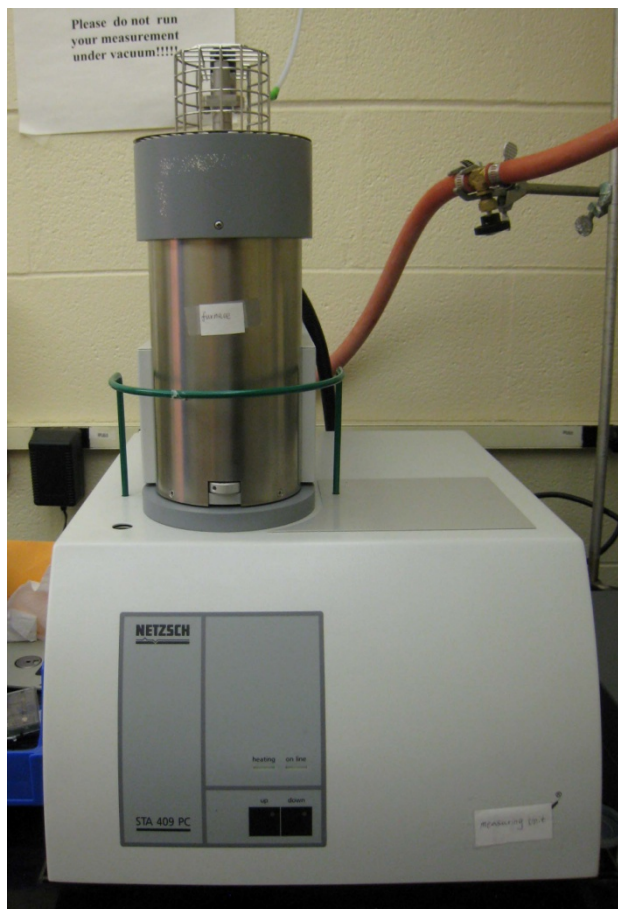
The technique of this analysis is to detect any occurring during the heating and cooling process by measuring the differential energy required to keep both the reference and sample. DSC detects the melting point of the sample during the endothermic reaction as more heat is absorbed, and crystallization point during the exothermic reaction because

heat is being generated. Figure 3.4 illustrates a scheme of DSC curve as a result. TG determines a change in the weight of a sample in a function of temperature while a flow of heat is applied.



**Figure 3.5 Scheme of DSC curve for endothermic and exothermic reactions.**

Both techniques are conducted on a NETZSCH STA 409PC Luxx instrument under a flow of argon as shown in Figure 3.5. The measurement can be done in an operating temperature range of 30-1600 °C with a minimum sample amount of 10 mg in an alumina crucible.



**Figure 3.6 NETZSCH STA 409PC Luxx differential scanning calorimetry (DSC).**

### 3.3 Physical property measurements

#### 3.3.1 Seebeck coefficient and electrical conductivity measurements

The Seebeck coefficient and the electrical conductivity are simultaneously measured using ULVAC-RICO ZEM-3 instrument as can be seen in Figure. 3.7.



**Figure 3.7 ULVAC-RICO ZEM-3 for the Seebeck coefficient and the electrical conductivity measurements.**

In order to measure such physical properties, the sample is pressed in a rectangular pellet with cold pressing instrument or hot-pressed in cylinder-like pellet with 30 ton press capability by Oxy-Gon industries shown in Figure 3.8 then cutting into a rectangular pellet. The pellet length ranges from 6 mm to 20 mm. The pellet is placed vertically on an electrode of the furnace chamber, which will be closed tight from the top to the bottom, and two thermocouple probes are moved into contact to the pellet from the side. Prior to the measurement of the Seebeck coefficient and the electrical conductivity, V-I plot of the

sample is obtained to determine if there is any defects on the sample. A linear plot is expected for V-I plot. Once the set up for the measurement is done, the furnace chamber is being evacuated and filled with helium to prevent oxidization of the sample during the measurement.



**Figure 3.8 Hot pressing instrument of high temperature vacuum furnace system with 30 ton press capability by Oxy-Gon industries.**

The ZEM-3 instrument measures the voltage difference between two sides of the pellet using two thermocouples while increasing the temperature, and the Seebeck coefficient can then be calculated using measured voltages and temperature with the following equation where  $dV$  is the potential difference<sup>64</sup>,

$$\text{The Seebeck coefficient} = \frac{dV}{T_2 - T_1} \quad (3.4)$$

$$\text{Measurement } T = \frac{(\text{temperature } T_1 + \text{temperature } T_2)}{2}$$

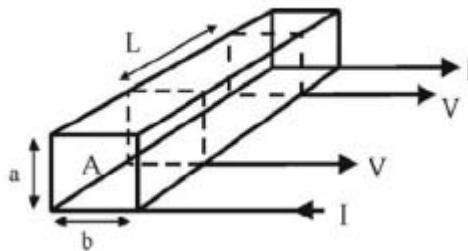
$$(3.5)$$

While the Seebeck coefficient is conducted, the electrical resistivity  $\rho$  will also be measured with the known values of dimensions ( $a \times b = A$ ,  $L$ ), which are obtained through the integrated microscope accessory. A current ( $I$ ) will be applied to the pellet to measure voltages while increasing the temperature. And resistance,  $R$  is calculated from the measured voltages along with a constant current where  $R$  can be expressed with Ohm's law in Equation (3.6) to determine the electrical conductivity as can be seen in Equation (3.7). Figure 3.9 illustrates the schematic view of measuring the electrical resistivity where  $a$ ,  $b$  and  $L$  are dimensional parameters of the pellet.

$$R = V/I \text{ (Ohm's law)} \quad (3.6)$$

$$\rho = (R \cdot A)/L$$

$$\sigma = \frac{1}{\rho} \quad (3.7)$$



**Figure 3.9 Schematic view of measuring the electrical resistivity with the dimensional parameters of a sample pellet shown.<sup>71</sup>**

### 3.3.2 Thermal conductivity measurements

The thermal conductivity measurement is conducted on the Flash Line 3000



thermal diffusivity system under argon (ANTER Corporation, viz) as can be seen in Figure 3.10.



**Figure 3.10 Flash Line 3000 thermal diffusivity system under argon (ANTER Corporation, viz).**

A thin cylinder-like pellet with a diameter of approximately 13 mm is used for this experiment, and liquid nitrogen is frequently added to cool down the IR detector. The thermal conductivity is calculated using the thermal diffusivity  $\alpha$  as measured by the instrument. A short pulse of the laser flash irradiates one side of the pellet, while the temperature of the opposite face is monitored using the IR detector. The following equations are used to calculate the thermal conductivity.

$$\kappa = \alpha \times \rho \times C_p \quad (3.8)$$

$\alpha$  is the thermal diffusivity,  $\rho$  is the density of a sample, and  $C_p$  is the molar specific heat. The thermal diffusivity is determined based on the following equation,<sup>64</sup>

$$\alpha = 0.1388 \left( \frac{L^2}{t_{1/2}} \right) \quad (3.9)$$

Where  $L$  is the thickness of a sample pellet and  $t_{1/2}$  is the half rise time. Moreover, the specific heat of each sample can be determined by the Dulong-Petit law<sup>72</sup> as expressed in Equation (3.10),

$$C_p = \frac{3R}{M} \quad (3.10)$$

where  $R$  is the gas constant and  $M$  is the averaged molar mass of the sample compound.

#### 4 Preparation of new quaternary clathrate compounds:



The site occupancy of the guest, Ba in ternary clathrates is one for each composed cage, dodecahedron and tetrakaidecahedron. A lanthanoid, in this paper, La, Ce or Eu, is substituted increasingly into the system of clathrates while the amount of the main guest atom, Ba decreases, and there will be changes in fractional site occupancies of the hosts because of two different guest atoms. The smaller sized atom, here the lanthanoid, will likely preferably occupy in a smaller cage. A substitution of 2<sup>nd</sup> guest atom will form new quaternary clathrate compounds, but will not change the structure of the compound. As the covalent radius of 2<sup>nd</sup> guest atoms is smaller than the main host, Ba, a decrease of the size of the unit cell is expected. The substitution might also lead to a lower thermal conductivity.<sup>3, 51</sup> The compound,  $\text{Ba}_{8-x}\text{Ln}_x\text{Ga}_{16}\text{Ge}_{30}$ , is an example formula of this project when Ln = Eu has a charge of 2+, and  $\text{Ba}_{8-x}\text{Ln}_x\text{Ga}_{16+x}\text{Ge}_{30-x}$  when Ln = La, and Ce have a charge of 3+. In the past, the compound  $\text{Ba}_{8-x}\text{Yb}_x\text{Ga}_{16}\text{Ge}_{30}$  was studied with  $x \leq 1.3$ .<sup>3</sup> However, there had been a doubt about a successful incorporation of Yb substituting into the system. Therefore, thorough and further studies on substitution of lanthanoid described in this thesis will provide more understanding of the system containing 2<sup>nd</sup> guest atoms that they are fully incorporate into clathrates.<sup>1, 55, 58</sup> In the following section, the structure and physical properties of Europium substituted quaternary clathrate compounds will be discussed.

#### 4.1 Syntheses and Analyses

All necessary elements are prepared from the stoichiometric amounts of high purity elements (Ba-granules under oil, 99%, Sigma Aldrich; La-powder type with -325 mesh, 99.9%, Alfa Aesar; Ce--powder type with -325 mesh, 99.9%, Alfa Aesar; Eu-ingot, 99.9%, Alfa Aesar; Ga-metal basis, 99.999%, Sigma Aldrich; Ge-metal basis pieces < 3.2mm, 99.999%, Alfa Aesar) though an excess amount of Ba is used to compensate the loss during the reaction where Ba, Ga, Ge are use in a ratio of 10 : 16 : 30.<sup>42</sup> The starting elements are weighed, placed in a carbon crucible, and put into a quartz tube in an Ar-filled glove box. The so prepared tubes are then evacuated under a vacuum line, and sealed with a hydrogen torch. At first, about 500 mg of samples of various quaternary clathrates, which included either La, Ce or Eu were formed in order to find the best condition to acquire homogeneous products, and then a larger quantity of 2~3 g samples were prepared for further property measurements.

The fused tubes were placed in a programmable furnace for heating up to 1000 °C within 24 hours, and they were kept at the same temperature for a day before a slow cooling to room temperature. The highest melting point of an element of the starting materials is 945 °C of germanium, so keeping samples for 24 hours at 1000 °C can offer enough time for them to melt and mix sufficiently. The samples are cooled down slowly over few days to 600 °C for crystallization, and then to a room temperature.

A substitution of Ce into Ba<sub>8</sub>Ga<sub>16</sub>Ge<sub>30</sub>, was prepared in the beginning, starting from 8-x Ba : x Ce : 16+x Ga : 30-x Ge where x = 0.1, 0.2, and 0.5 based on a stoichiometric ratio. However, the samples were not homogeneous, but mixed with different phases such

as  $Ba_{8-x}Ce_xGa_{16+x}Ge_{30-x}$ , single elements of Ga or Ge,  $Ba_8Ga_7$ ,  $Ba_6Ge_{25}$ ,  $Ba_5Ge_3$ ,  $BaGe_2$ . The reaction in respect to a stoichiometric ratio was not fully achieved as extra elements emerged on the product side according to the X-ray powder diffraction analysis where INEL XRG 3000 powder diffractometer was used as mentioned earlier. Then a formation of binary compounds of  $BaGe_2$  was tried based on a stoichiometric ratio, but this also did not work.

Later, I found that the use of an additional 25% of Ba as a starting material would lead to a homogeneous compound according to Hou et al.<sup>41</sup> So a sample compound of 9.8 Ba : 0.2 Ce : 16.2 Ga : 29.8 Ge was prepared. In the beginning, the main product of this sample was determined to be almost pure phase based on the X-ray powder diffraction analysis, but not pure enough for a structural and physical analysis. Therefore, various annealing temperatures and heating profiles were then tested in order to achieve the best condition to acquire a pure phase compound. It was found that a slow heating profile for the reaction along with annealing temperature of 600 °C for 8 days would increase the homogeneity of compounds.

Starting elements of Ba, Ce, Ga and Ge in with respect to a stoichiometric ratio of  $10-x : x : 16+x : 30-x$  when  $x = 0.1, 0.2, 0.3, 0.4, 0.5, 0.8,$  and  $1.0$  were used to form quaternary clathrate compounds. The product came out as a very solid ingot, and it was annealed once of a times at 600 °C for 8 days after being ground after each heating cycle. Successful results were obtained for such nominal stoichiometric amounts,  $x = 0.3, 0.5$  and  $1.0$ .

After the formation of some Ce-containing clathrates, lanthanum was used for the next investigation. A stoichiometric ratio of  $10-x : x : 16+x : 30-x$  for Ba, La, Ga and Ge respectively when  $x = 0.1, 0.2, 0.3, 0.4, 0.5, 0.8,$  and  $1.0$  was prepared. Lanthanum substituted compounds along with barium only exhibited few pure samples when  $x = 0.2, 0.3, 0.4$  and  $1.0$  of nominal stoichiometric values, like cerium substituted compounds even the samples were annealed for several times at  $600\text{ }^{\circ}\text{C}$ .

Along with the experiments of La and Ce, europium was also used to form quaternary clathrates, starting from  $10-x \text{ Ba} : x \text{ Eu} : 16 \text{ Ga} : 30 \text{ Ge}$  with  $x = 0.1, 0.2, 0.3, 0.4, 0.5, 0.8,$  and  $1.0$  of nominal stoichiometric values. The mixture of starting materials reacted in a slow reaction profile and was annealed at  $600\text{ }^{\circ}\text{C}$ . As europium has a charge of  $2+$ , the stoichiometric ratio is different than La and Ce. In the case of europium, most of reacted samples formed homogeneous compounds.

Since the substitution of a  $2^{\text{nd}}$  guest atom into a clathrate-I does not change the structure type, all newly formed quaternary compounds exhibit the same XRD pattern with a ternary clathrate, so all products were compared with a reference XRD pattern of  $\text{Ba}_8\text{Ga}_{16}\text{Ge}_{30}$  for the confirmation of purity. Identification of successfully reacted samples was determined through using various methods such as Le Bail method, Rietveld analysis, EDX-SEM analysis and thermal analysis. As expected, all formed quaternary compounds share the same space group of  $Pm\bar{3}n$ , but the size of the unit cell varies depending on the  $2^{\text{nd}}$  guest atom. However, as no pure products were obtained for  $x > 1.0$ , one can conclude that clathrates with the composition of  $x$  beyond  $1.0$  will not cooperate to form homogeneous quaternary compounds.

Differential scanning calorimetry (DSC) analyses, NETZSCH STA 409PC Luxx were carried out under a flow of Ar for several samples to find the melting points, which were found to be between 975 and 978 °C. Moreover, selected samples were also analyzed with scanning electron microscope (SEM) of LEO 1530 FESEM integrated with energy dispersive analysis of X-rays (EDX) of Pegasus 1200 where the compositions were determined through acquired atomic percentages.

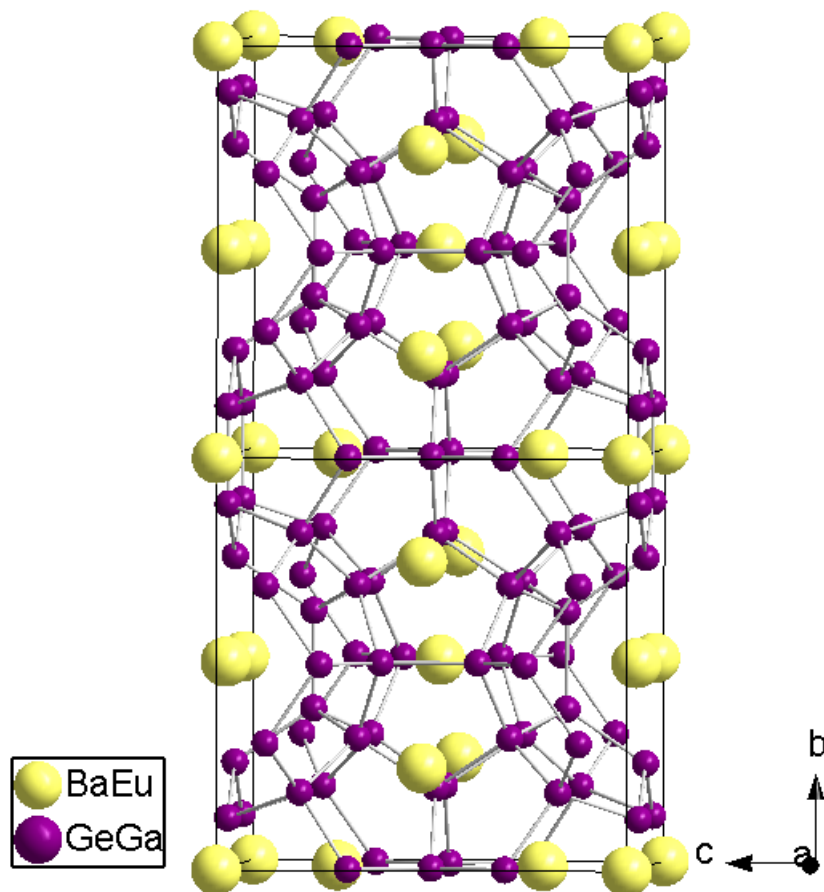
## **4.2 Structure and properties of $\text{Ba}_{8-x}\text{Eu}_x\text{Ga}_{16}\text{Ge}_{30}$**

### **4.2.1 Crystal structure**

The newly formed quaternary clathrate compounds are known to exhibit the same crystal structure as the ternary compounds with the space group of  $Pm\bar{3}n$ , where 2<sup>nd</sup> guest atom of europium shares the occupancy sites of the guest atoms with barium. Therefore, the structure type is well known as there have been many studies on ternary clathrates. However, changes can be found for the quaternary compounds, namely differential fractional occupancies for the guest atoms, and changes in the unit cell because of the introduction of 2<sup>nd</sup> guest atom into the system. Similar to the ternary compounds where Ga and Ge of the host frameworks share all three different Wyckoff sites, 6c, 16i and 24k, the 2a and 6d sites of Ba are now shared with Eu for the new compound. The two cages made with Ga-Ga bonds, Ga-Ge bonds and Ge-Ge bonds are flexible in terms of the size depending on the occupancy of a guest atom where occupied guests are loosely bonded to the frameworks.

The crystal structure of  $\text{Ba}_{8-x}\text{Eu}_x\text{Ga}_{16}\text{Ge}_{30}$  after a Rietveld refinement is shown in Figure 4.1 where yellow balls represent Ba/Eu, and purple balls represent the frameworks

of Ga/Ge.



**Figure 4.1** Crystal structure of  $Ba_{8-x}Eu_xGa_{16}Ge_{30}$ .

Rietveld refinements were carried out for confirmed homogeneous samples where no impurities are found from the XRD pattern because any unknown peaks in XRD pattern can cause wrong values for structural information of samples. The refinements were performed on the samples with the nominal compositions,  $Ba_{7.8}Eu_{0.2}Ga_{16}Ge_{30}$ ,  $Ba_{7.7}Eu_{0.3}Ga_{16}Ge_{30}$ ,  $Ba_{7.6}Eu_{0.4}Ga_{16}Ge_{30}$ ,  $Ba_{7.5}Eu_{0.5}Ga_{16}Ge_{30}$ , and  $Ba_{7.0}Eu_{0.5}Ga_{16}Ge_{30}$ . An example of a Rietveld refinement can be seen in Figure 4.2. The refinement result proves the structure of the newly formed quaternary clathrate compounds matches with the



calculated model based on the reference<sup>34</sup> very well without any side products.

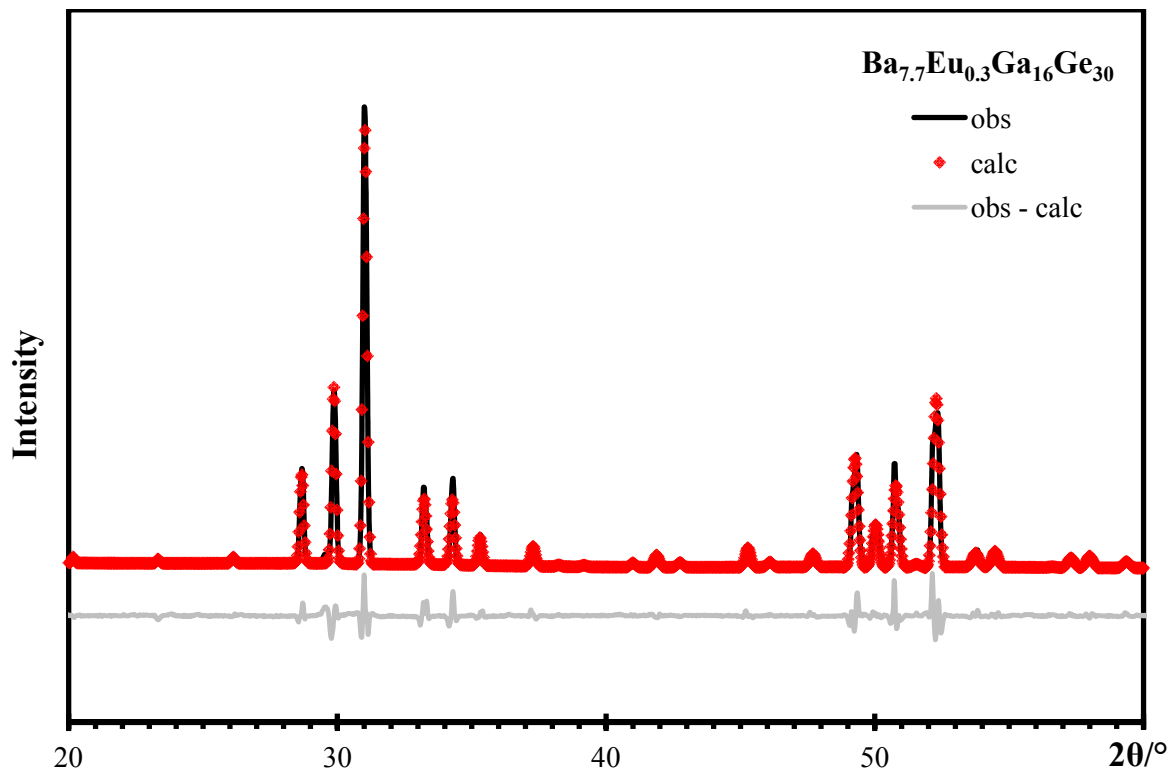


Figure 4.2 Rietveld refinement of  $\text{Ba}_{7.7}\text{Eu}_{0.3}\text{Ga}_{16}\text{Ge}_{30}$ .

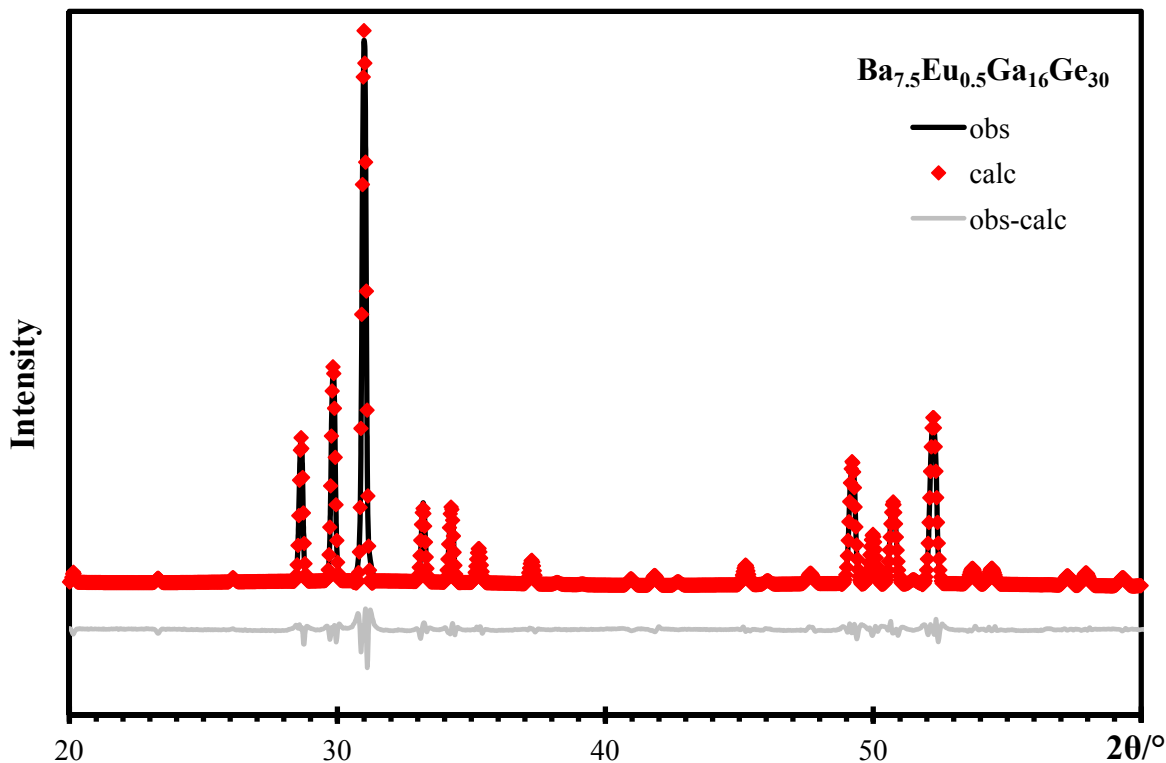


Figure 4.3 Rietveld refinement of  $\text{Ba}_{7.5}\text{Eu}_{0.5}\text{Ga}_{16}\text{Ge}_{30}$ .

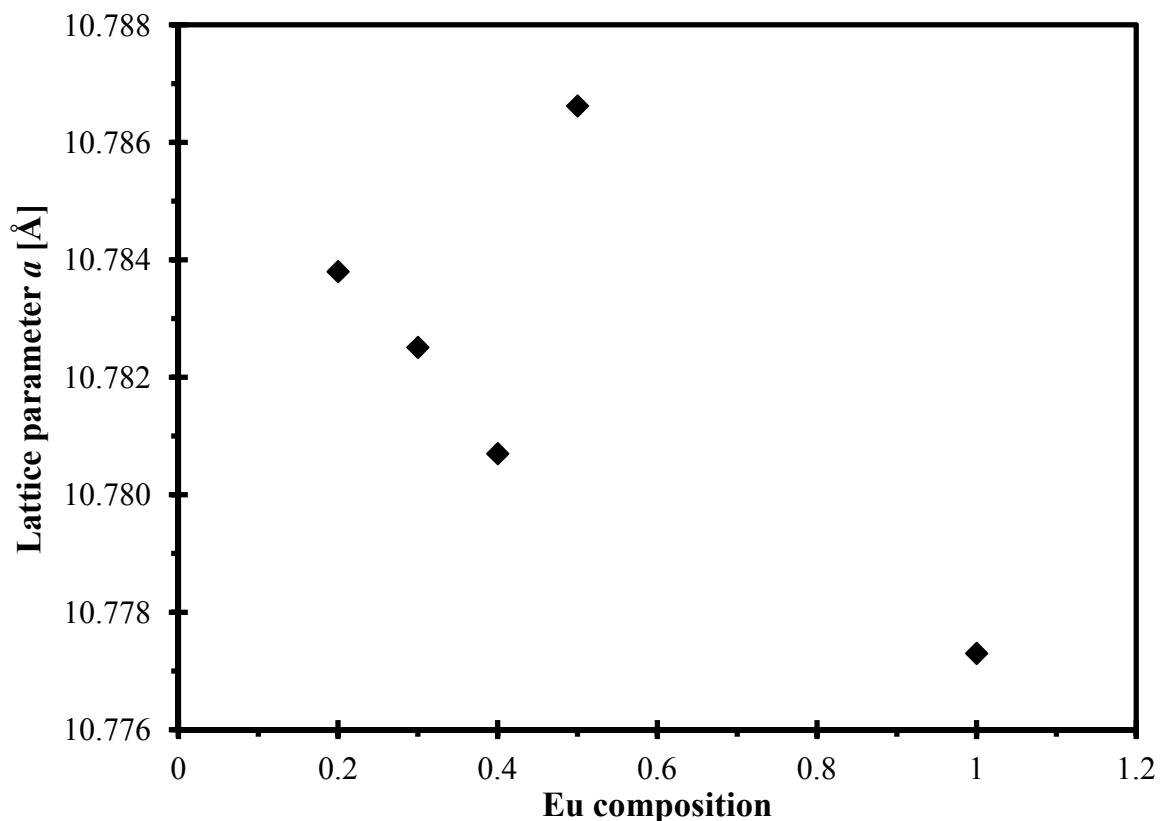
The occupancy, thermal displacement parameter, atomic positions and other parameters were refined to acquire the best values, however, some of parameters such as thermal displacement parameter and the occupancy couldn't be refined at the same time because of high correlation.  $\text{Ba}_{7.8}\text{Eu}_{0.2}\text{Ga}_{16}\text{Ge}_{30}$  has the lattice parameter  $a = 10.7838(1) \text{ \AA}$  and  $a$  decreases with increasing the amount of europium up to  $x < 0.5$ . The sample with  $x = 0.5$  appears to be an exception. Similar result was also found in the paper of Tang et al. where they substituted Yb.<sup>3</sup> Figure 4.3 depicts the relationship between  $x$  and the lattice parameter. More details of these refinements for  $\text{Ba}_{8-x}\text{Eu}_x\text{Ga}_{16}\text{Ge}_{30}$  are listed in Table 4.2 and 4.3.

**Table 4.1 Refinement details of Ba<sub>8-x</sub>Eu<sub>x</sub>Ga<sub>16</sub>Ge<sub>30</sub> when x = 0.2, 0.3 and 0.4.**

Refined formula	Ba <sub>7.8</sub> Eu <sub>0.2</sub> Ga <sub>16</sub> Ge <sub>30</sub>	Ba <sub>7.7</sub> Eu <sub>0.3</sub> Ga <sub>16</sub> Ge <sub>30</sub>	Ba <sub>7.6</sub> Eu <sub>0.4</sub> Ga <sub>16</sub> Ge <sub>30</sub>
Formula weight [g/mol]	4384.23	4352.88	4378.29
<i>T</i> for measurement [K]	296(2)	296(2)	296(2)
$\lambda$ [Å]	0.71073	0.71073	0.71073
Space group	<i>Pm</i> $\bar{3}$ <i>n</i>	<i>Pm</i> $\bar{3}$ <i>n</i>	<i>Pm</i> $\bar{3}$ <i>n</i>
<i>a</i> [Å]	10.78380(6)	10.78251(6)	10.78070(5)
<i>V</i> [Å <sup>3</sup> ]	1254.05(2)	1253.60(2)	1252.97(2)
<i>Z</i>	1	1	1
$\rho_{\text{cal}}$ [g/cm <sup>3</sup> ]	5.805	5.766	5.802
Rp / wRp	0.0526 / 0.0803	0.0574 / 0.0875	0.0513 / 0.0705

**Table 4.2 Refinement details of Ba<sub>8-x</sub>Eu<sub>x</sub>Ga<sub>16</sub>Ge<sub>30</sub> when x = 0.5, and 1.0.**

Refined formula	Ba <sub>7.5</sub> Eu <sub>0.5</sub> Ga <sub>16</sub> Ge <sub>30</sub>	Ba <sub>7.0</sub> Eu <sub>1.0</sub> Ga <sub>16</sub> Ge <sub>30</sub>
Formula weight [g/mol]	4398.85	4362.63
<i>T</i> for measurement [K]	296(2)	296(2)
$\lambda$ [Å]	0.71073	0.71073
Space group	<i>Pm</i> $\bar{3}$ <i>n</i>	<i>Pm</i> $\bar{3}$ <i>n</i>
<i>a</i> [Å]	10.78662(4)	10.7773(2)
<i>V</i> [Å <sup>3</sup> ]	1255.04(1)	1251.77(7)
<i>Z</i>	1	1
$\rho_{\text{cal}}$ [g/cm <sup>3</sup> ]	5.820	5.787
Rp / wRp	0.0368 / 0.0539	0.0497 / 0.0697



**Figure 4.4** Eu composition dependence of the lattice parameter  $a$  (Å) of  $\text{Ba}_{8-x}\text{Eu}_x\text{Ga}_{16}\text{Ge}_{30}$ .

The atomic positions and thermal displacement parameters of  $\text{Ba}_{7.54(1)}\text{Eu}_{0.46(1)}\text{Ga}_{16}\text{Ge}_{30}$  and  $\text{Ba}_{6.85(1)}\text{Eu}_{1.20(1)}\text{Ga}_{16}\text{Ge}_{30}$  are listed in Table 4.3 and 4.4. The constraints were used to refine the compounds of quaternary samples because Ba and Eu, and Ga and Ge share the same occupancy sites. Only the occupancy of the guest atoms was refined because the composition of the host atoms did not change. All thermal displacement parameters were refined, and a considerably large value was observed for  $6d$  site compared to the other occupancy sites because of the rattling motion of guests in tetrakaidecahedron cages where an increase in distance between the cage and the guest atom increases the thermal displacement parameter. Therefore, the thermal displacement parameter increases

with increasing amount of Eu.

**Table 4.3 Atomic coordinates, equivalent thermal displacement parameters and occupancy**

**factors of Ba<sub>7.54(1)</sub>Eu<sub>0.46(1)</sub>Ga<sub>16</sub>Ge<sub>30</sub>.**

Atom	site	x	Y	z	Uiso / Å <sup>2</sup>	occ.
Ba1	2a	0	0	0	0.014(1)	0.966(1)
Ba2	6d	0	1/4	1/2	0.017(1)	0.934(1)
Eu1	2a	0	0	0	0.014(1)	0.034(1)
Eu2	6d	0	1/4	1/2	0.017(1)	0.066(1)
Ga1	6c	1/4	0	1/2	0.010	0.35
Ge1	6c	1/4	0	1/2	0.010	0.65
Ga2	16i	0.1848(1)	0.1848(1)	0.1848(1)	0.010	0.35
Ge2	16i	0.1848(1)	0.1848(1)	0.1848(1)	0.010	0.65
Ga3	24k	0	0.3100(2)	0.1195(2)	0.010	0.35
Ge3	24k	0	0.3100(2)	0.1195(2)	0.010	0.65

**Table 4.4 Atomic coordinates, equivalent thermal displacement parameters and occupancy factors of  $\text{Ba}_{6.85(1)}\text{Eu}_{1.20(1)}\text{Ga}_{16}\text{Ge}_{30}$ .**

Atom	site	x	y	z	Uiso / Å <sup>2</sup>	occ.
Ba1	2a	0	0	0	0.0190(8)	0.922(1)
Ba2	6d	0	1/4	1/2	0.0151(8)	0.834(1)
Eu1	2a	0	0	0	0.0190(8)	0.084(1)
Eu2	6d	0	1/4	1/2	0.0151(8)	0.172(1)
Ga1	6c	1/4	0	1/2	0.010	0.35
Ge1	6c	1/4	0	1/2	0.010	0.65
Ga2	16i	0.1853(1)	0.1853(1)	0.1853(1)	0.010	0.35
Ge2	16i	0.1853(1)	0.1853(1)	0.1853(1)	0.010	0.65
Ga3	24k	0	0.3111(2)	0.1167(2)	0.010	0.35
Ge3	24k	0	0.3111(2)	0.1167(2)	0.010	0.65

The direct interactions only occurred within the frameworks, and the interaction between the frameworks and the guest atoms are bonded indirectly. Also, the Ga/Ge1 site does not have a connection with Ga/Ge2 site, but bonded to Ga/Ge3 site where a single bond distance between Ga/Ge1-Ga/Ge3 is 2.50 Å for  $\text{Ba}_{7.8}\text{Eu}_{0.2}\text{Ga}_{16}\text{Ge}_{30}$ , 2.51 Å for  $\text{Ba}_{7.5}\text{Eu}_{0.5}\text{Ga}_{16}\text{Ge}_{30}$ , and 2.49 Å for  $\text{Ba}_{7.0}\text{Eu}_{1.0}\text{Ga}_{16}\text{Ge}_{30}$ . The Ga/Ge2 site also bonds to Ga/Ge3 site with a distance of 2.49 Å for  $\text{Ba}_{7.8}\text{Eu}_{0.2}\text{Ga}_{16}\text{Ge}_{30}$ , 2.50 Å for  $\text{Ba}_{7.5}\text{Eu}_{0.5}\text{Ga}_{16}\text{Ge}_{30}$ , and 2.52 Å for  $\text{Ba}_{7.0}\text{Eu}_{1.0}\text{Ga}_{16}\text{Ge}_{30}$ . Table 4.1 shows selected interatomic distances of  $\text{Ba}_{8-x}\text{Eu}_x\text{Ga}_{16}\text{Ge}_{30}$  when  $x = 0.2, 0.5$  and  $1.0$ .

**Table 4.5 Selected interatomic distances [Å] of Ba<sub>8-x</sub>Eu<sub>x</sub>Ga<sub>16</sub>Ge<sub>30</sub>.**

Interaction	Multiplicity	d / Å [x = 0.2]	d / Å [x = 0.5]	d / Å [x = 1.0]
Ba/Eu1 – Ga/Ge2	8	3.4657(2)	3.4397(1)	3.4584(2)
Ba/Eu1 – Ga/Ge3	12	3.5605(2)	3.5799(2)	3.5810(3)
Ba/Eu2 – Ga/Ge1	4	3.8127(1)	3.8130(1)	3.8103(1)
Ba/Eu2 – Ga/Ge2	8	3.9982(2)	4.0066(1)	3.9973(2)
Ba/Eu2 – Ga/Ge3	8	3.6399(2)	3.6309(2)	3.6036(2)
Ga/Ge1 – Ga/Ge3	4	2.5041(2)	2.4864(1)	2.4915(2)
Ga/Ge2 – Ga/Ge2	1	2.4076(2)	2.4605(2)	2.4166(2)
Ga/Ge2 – Ga/Ge3	3	2.4970(2)	2.4980(2)	2.5242(3)
Ga/Ge3 – Ga/Ge1	1	2.5041(3)	2.4864(2)	2.4915(2)
Ga/Ge3 – Ga/Ge2	2	2.4970(2)	2.4980(2)	2.5242(3)
Ga/Ge3 – Ga/Ge3	1	2.5885(3)	2.5966(2)	2.5158(3)

#### 4.2.2 Thermal analysis and EDX analysis

Thermal analysis was performed with differential scanning calorimetry (DSC) on all of Eu-containing clathrates, and the measurements showed the melting points of  $\text{Ba}_{8-x}\text{Eu}_x\text{Ga}_{16}\text{Ge}_{30}$  are 977°C and 978°C as shown in Figure 4.4. The melting point of Eu containing clathrates is higher than of the ternary clathrates with 974°C.<sup>34</sup>

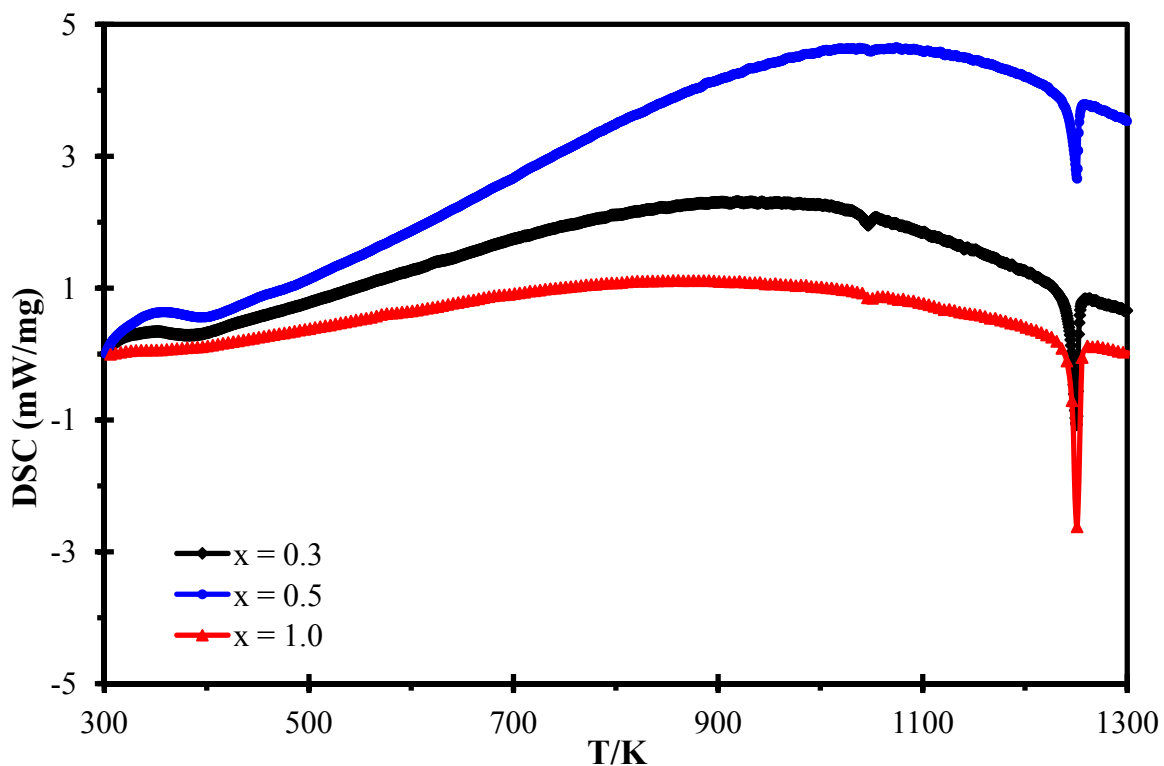


Figure 4.5 DSC curves of  $\text{Ba}_{8-x}\text{Eu}_x\text{Ga}_{16}\text{Ge}_{30}$ .

Energy dispersive X-ray analysis was also carried out for to obtain the atomic percentages of  $\text{Ba}_{8-x}\text{Eu}_x\text{Ga}_{16}\text{Ge}_{30}$ . Table 4.6 shows the EDX data obtained for  $\text{Ba}_{7.5}\text{Eu}_{0.5}\text{Ga}_{16}\text{Ge}_{30}$  that average atomic percentages of elements, 13.9: 0.9: 29.4: 55.8 were similar to the calculated atomic percentages. Moreover, 14.4: 0.5: 29.8: 55.4 for  $\text{Ba}_{7.8}\text{Eu}_{0.2}\text{Ga}_{16}\text{Ge}_{30}$ , 14.4: 0.5: 29.3: 55.8 for  $\text{Ba}_{7.7}\text{Eu}_{0.3}\text{Ga}_{16}\text{Ge}_{30}$ , 13.9: 0.9: 29.4: 55.8 for



Ba<sub>7.6</sub>Eu<sub>0.4</sub>Ga<sub>16</sub>Ge<sub>30</sub>, and 13.4: 1.5: 29.3: 55.9 for Ba<sub>7.0</sub>Eu<sub>1.0</sub>Ga<sub>16</sub>Ge<sub>30</sub> were obtained as can be seen in Table 4.7. EDX data were obtained via taking various spots for even distribution of values where the numbers are shown in Table 4.6.

**Table 4.6 Atomic percentages of elements from EDX data for Ba<sub>7.5</sub>Eu<sub>0.5</sub>Ga<sub>16</sub>Ge<sub>30</sub>.**

Element	Calculated	1	2	3	4	5	6	Avg.
Ba	13.9	14.1	13.9	15.3	15.3	12.9	12.0	13.9
Eu	0.9	0.6	0.5	0.9	0.3	1.3	1.7	0.9
Ga	29.6	29.3	29.7	29.6	27.9	29.6	29.9	29.4
Ge	55.6	56.0	56.0	54.2	56.6	56.1	56.5	55.8

**Table 4.7 Average element composition of the Ba<sub>8-x</sub>Eu<sub>x</sub>Ga<sub>16</sub>Ge<sub>30</sub> compounds. The actual composition was obtained by EDX analysis.**

Nominal Composition	Eu content x		Average Composition (atomic %)			
	Nominal	Actual	Ba	Eu	Ga	Ge
Ba <sub>7.8</sub> Eu <sub>0.2</sub> Ga <sub>16</sub> Ge <sub>30</sub>	0.2	0.2	14.4	0.5	29.8	55.4
Ba <sub>7.7</sub> Eu <sub>0.3</sub> Ga <sub>16</sub> Ge <sub>30</sub>	0.3	0.3	14.4	0.5	29.3	55.8
Ba <sub>7.6</sub> Eu <sub>0.4</sub> Ga <sub>16</sub> Ge <sub>30</sub>	0.4	0.4	13.9	0.8	29.5	55.8
Ba <sub>7.5</sub> Eu <sub>0.5</sub> Ga <sub>16</sub> Ge <sub>30</sub>	0.5	0.5	13.9	0.9	29.4	55.8
Ba <sub>7.0</sub> Eu <sub>1.0</sub> Ga <sub>16</sub> Ge <sub>30</sub>	1.0	0.8	13.4	1.5	29.3	55.9

### 4.2.3 Physical property measurements

For physical property measurements, cold-pressed pellets of the dimensions  $13 \times 2 \times 2$  mm of all homogeneous samples were prepared. The Seebeck coefficient,  $S$ , and the electrical conductivity,  $\sigma$  were determined utilizing the ULVAC-RICO ZEM-3 under a flow of helium between 300 K and 693 K. There is no a clear trend for the electrical conductivity with increasing  $x$  as shown in Figure 4.5 while the values increases gradually with increasing temperature. The maximum electrical conductivity among various compositions of Eu clathrates is found to be  $3.3 \Omega^{-1}\text{cm}^{-1}$  with  $x = 0.3$  for a cold-pressed pellet. Woods et al. reported that  $1.2 \Omega^{-1}\text{cm}^{-1}$  was achieved for  $\text{Eu}_4\text{Sr}_4\text{Ga}_{16}\text{Ge}_{30}$  at room temperature.<sup>73</sup>

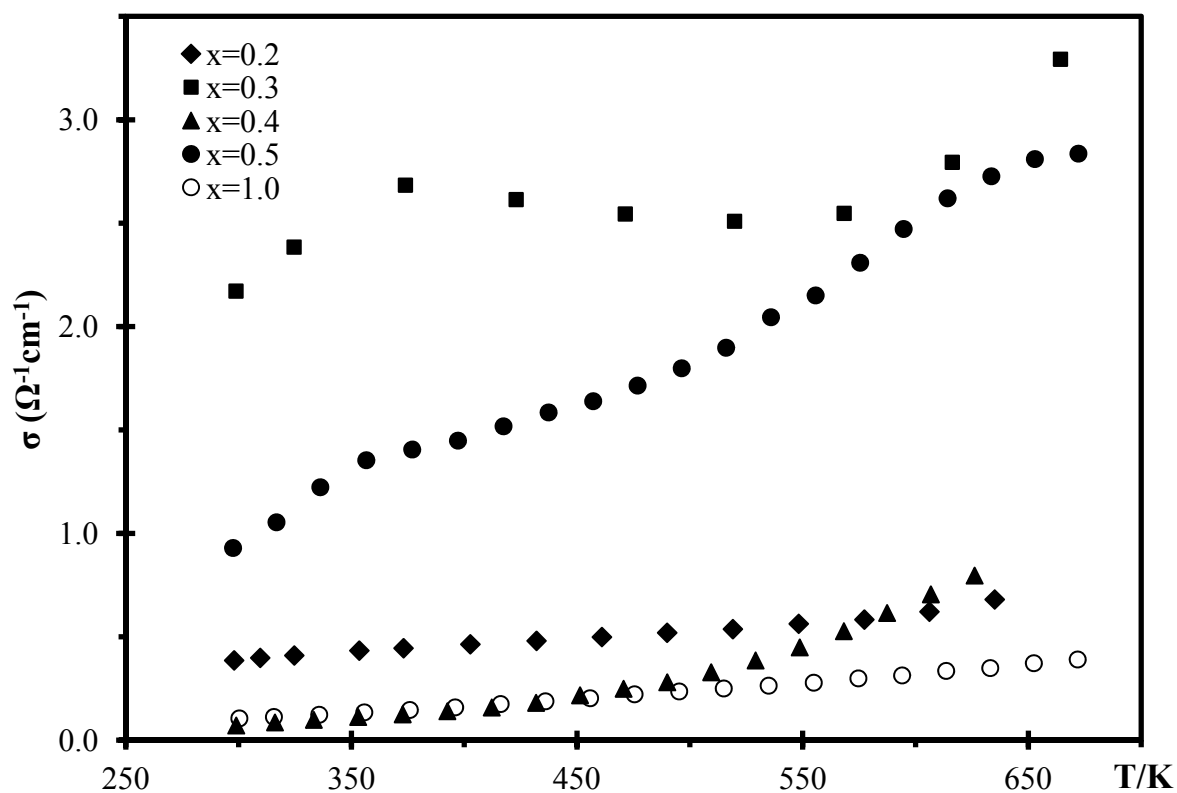
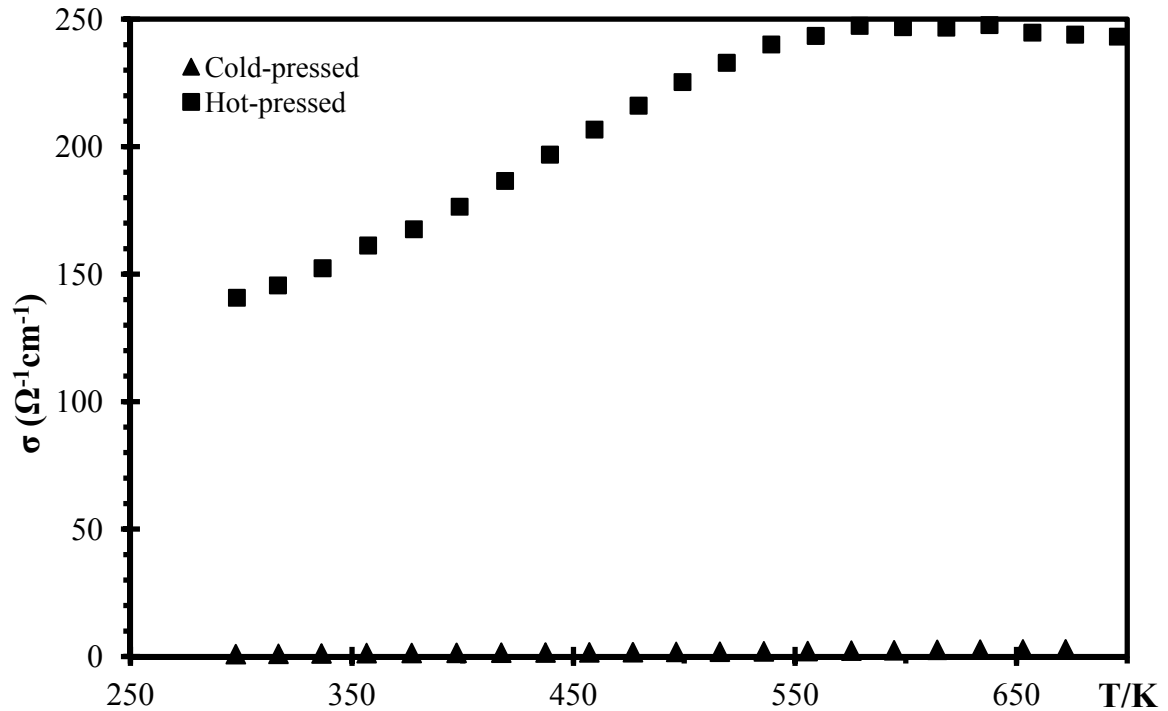


Figure 4.6 Electrical conductivity of  $\text{Ba}_{8-x}\text{Eu}_x\text{Ga}_{16}\text{Ge}_{30}$ .

A hot-pressed pellet of  $\text{Ba}_{7.5}\text{Eu}_{0.5}\text{Ga}_{16}\text{Ge}_{30}$  was prepared with Oxy-Gon's hot press, which became available during the last weeks of this thesis. A hot-pressed pellet was not in a rectangular form, so a diamond saw with a very slow speed was used to cut the pellet into dimensions of  $13 \times 2 \times 2$  mm. A comparison of physical properties for  $\text{Ba}_{7.5}\text{Eu}_{0.5}\text{Ga}_{16}\text{Ge}_{30}$  is shown below, demonstrating that a significant improvement for hot-pressed sample was achieved with the highest electrical conductivity of  $250 \Omega^{-1}\text{cm}^{-1}$  compared to  $2.8 \Omega^{-1}\text{cm}^{-1}$  of cold-pressed sample. This is due to the increased relative density and decreased grain boundaries.



**Figure 4.7** Electrical conductivity of cold-pressed and hot-pressed  $\text{Ba}_{7.5}\text{Eu}_{0.5}\text{Ga}_{16}\text{Ge}_{30}$ .

According to the Seebeck coefficient measurements, all europium substituted quaternary compounds are n-type semiconductor as the values are all negative. The values are between -100 and -450  $\mu\text{V}\cdot\text{K}^{-1}$  for the  $\text{Ba}_{8-x}\text{Eu}_x\text{Ga}_{16}\text{Ge}_{30}$  compounds. And these values of the Seebeck coefficient for cold-pressed pellets are great compared to 250  $\mu\text{V}\cdot\text{K}^{-1}$  of a general Seebeck coefficient of a good thermoelectric material.

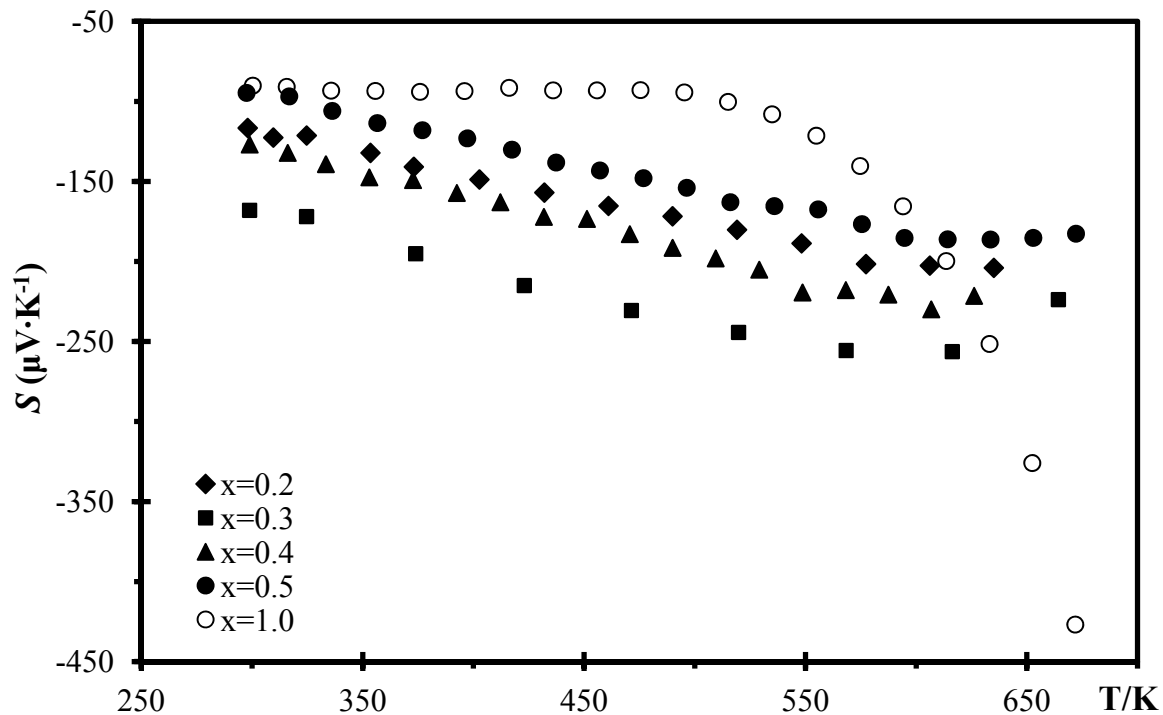
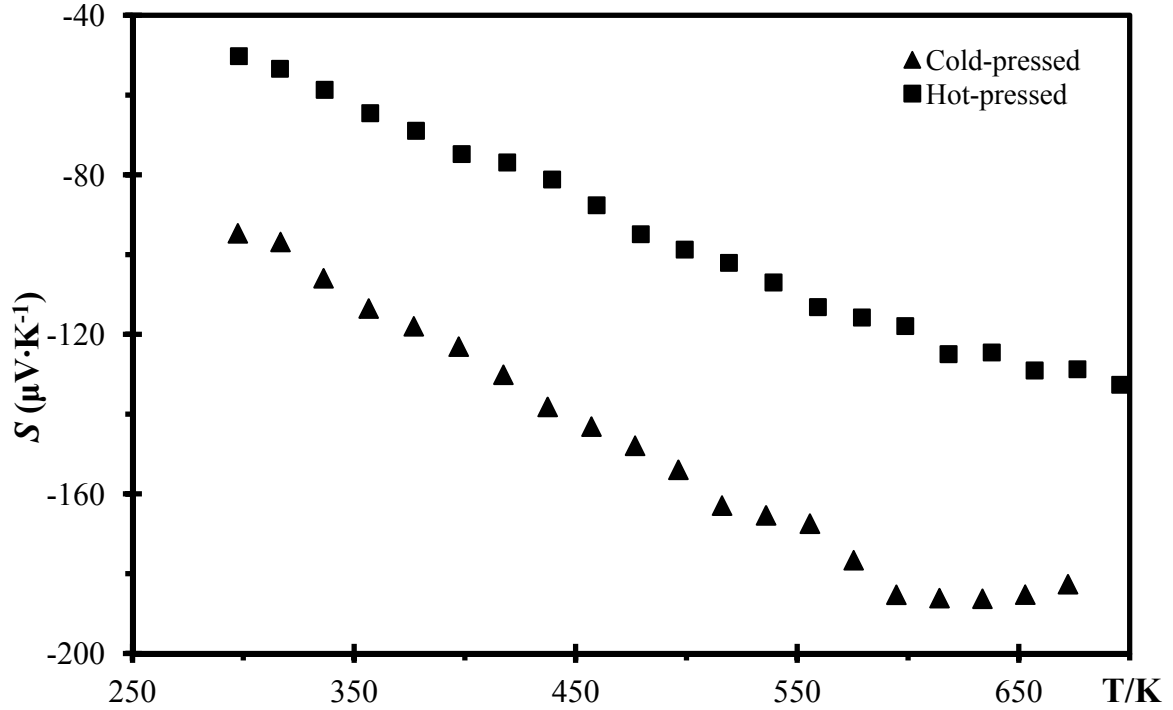


Figure 4.8 Seebeck coefficient of  $\text{Ba}_{8-x}\text{Eu}_x\text{Ga}_{16}\text{Ge}_{30}$ .



**Figure 4.8** Seebeck coefficient of cold-pressed and hot-pressed  $\text{Ba}_{7.5}\text{Eu}_{0.5}\text{Ga}_{16}\text{Ge}_{30}$ .

The power factor values, calculated via  $S^2\sigma$ , of  $\text{Ba}_{8-x}\text{Eu}_x\text{Ga}_{16}\text{Ge}_{30}$  are between  $0.00086 \mu\text{Wcm}^{-1}\text{K}^{-2}$  at 300 K and  $0.18 \mu\text{Wcm}^{-1}\text{K}^{-2}$  at 616 K. These values indicate the goodness of the material as a thermoelectric material, and the ternary clathrates exhibited in the range of  $2.2 - 3.2 \mu\text{Wcm}^{-1}\text{K}^{-2}$  at room temperature.<sup>74</sup> The cold-pressed samples do not show good power factor values. However, the value of a hot-pressed pellet for  $\text{Ba}_{7.5}\text{Eu}_{0.5}\text{Ga}_{16}\text{Ge}_{30}$  exhibits much higher values than cold-pressed pellet of the same sample that  $4.7 \mu\text{Wcm}^{-1}\text{K}^{-2}$  was achieved at 734 K when  $0.1 \mu\text{Wcm}^{-1}\text{K}^{-2}$  was obtained for a cold-pressed sample as. The comparison of cold-pressed and hot-pressed samples is shown in Figure 4.9. The increase in the power factor value means that the properties can be improved via hot pressing, and may obtain higher values for other compositions of the Eu compounds.

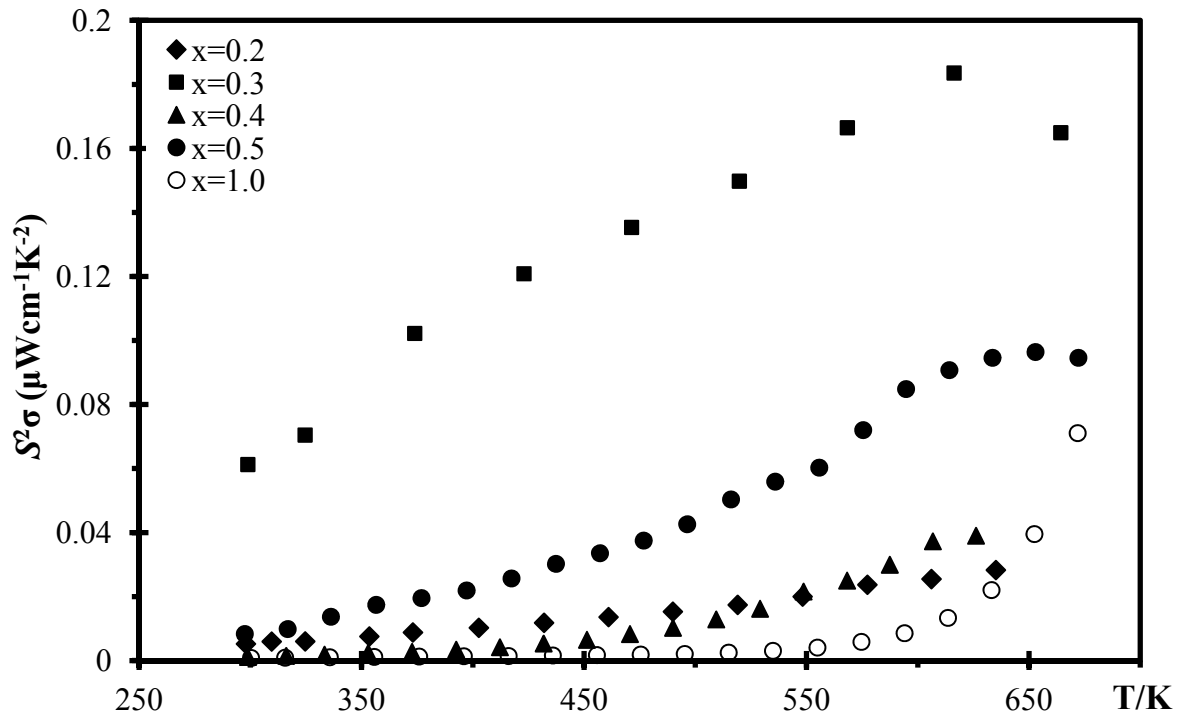


Figure 4.10 Power factor of  $\text{Ba}_{8-x}\text{Eu}_x\text{Ga}_{16}\text{Ge}_{30}$ .

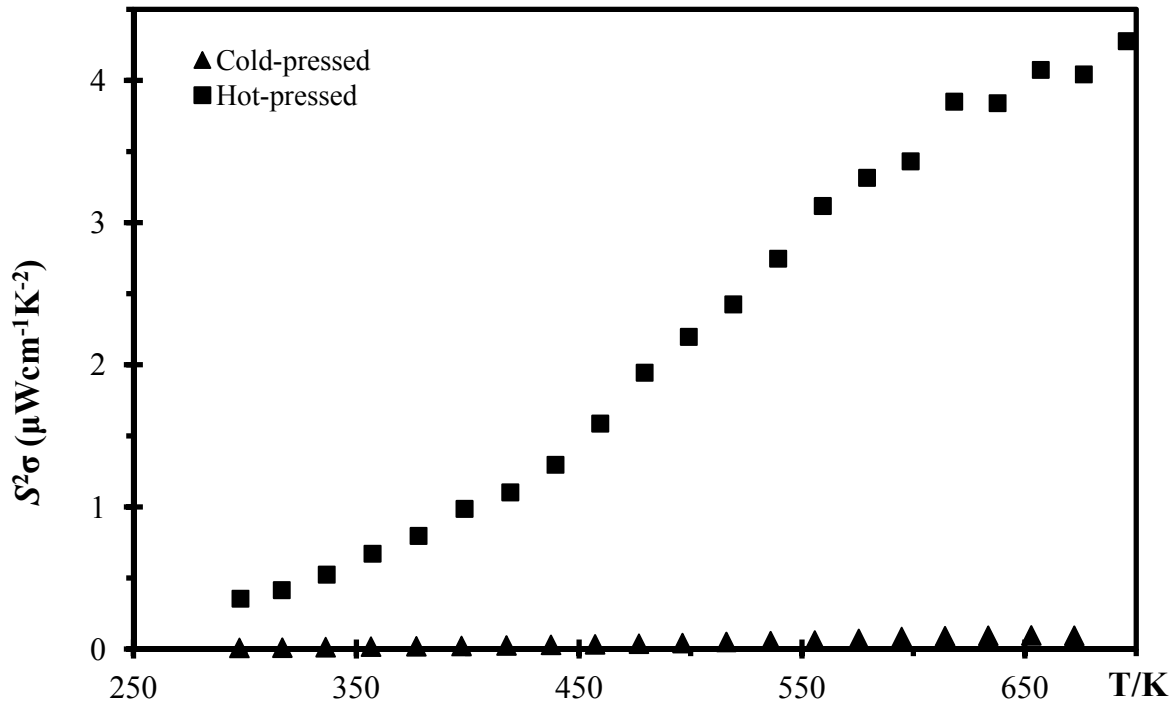


Figure 4.11 Power factor of cold-pressed and hot-pressed  $\text{Ba}_{7.5}\text{Eu}_{0.5}\text{Ga}_{16}\text{Ge}_{30}$ .

#### 4.2.4 Conclusions

The quaternary clathrate compounds of europium with  $0 < x \leq 1.0$  were studied with various analytical methods. The formation of homogeneous quaternary clathrates was successfully done. Even though the crystal structure of the quaternary compounds exhibits the same crystal structure of the ternary compounds, changes in the unit cell size depending on the amount of  $x$  along with displacements of atomic positions are discovered. The Rietveld refinements indicate the preferential occupancy of guest atoms that europium tend to occupy in a small cage because of the size effect. Moreover, the unit cell size of these compounds shrinks with increasing amount of Eu. The average single bond of Ga/Ge-Ga/Ge is found to be 2.5 Å. The thermoelectric properties as determined so far are not satisfactory, but may be improved upon hot-pressing of differently doped materials.

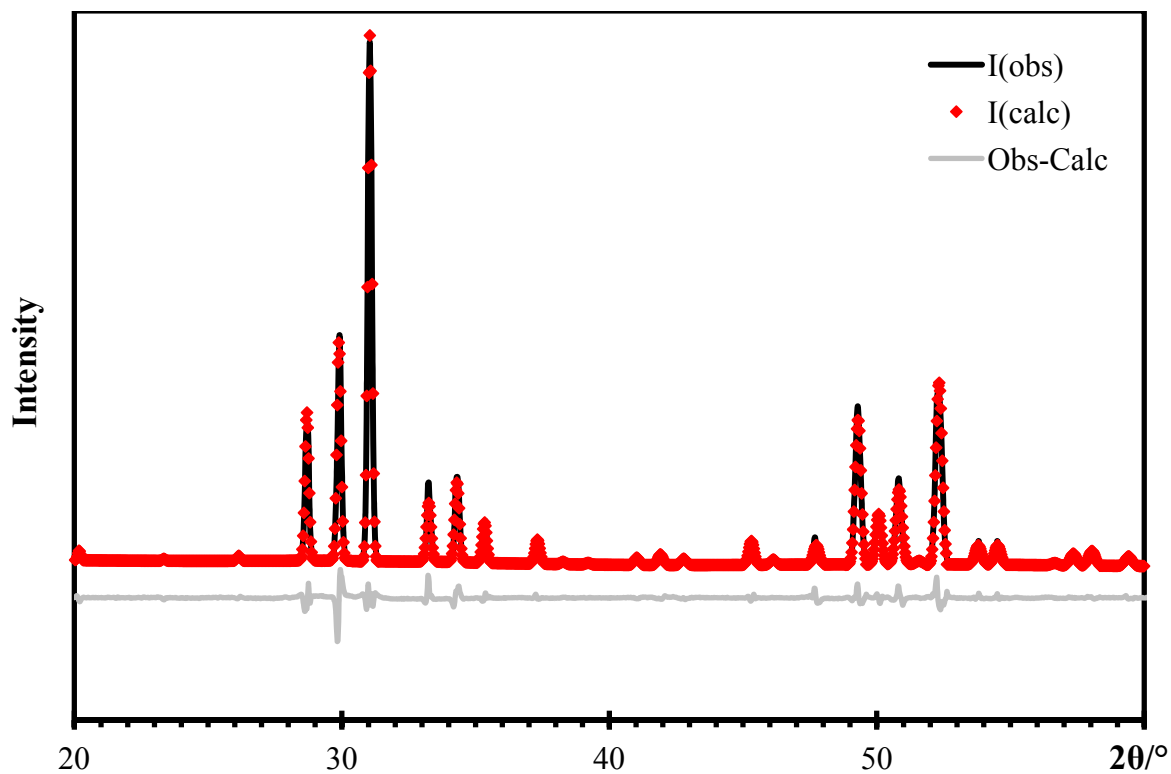
### 4.3 Structure and properties of $\text{Ba}_{8-x}\text{Ce}_x\text{Ga}_{16+x}\text{Ge}_{30-x}$

#### 4.3.1 Crystal structure

The  $\text{Ba}_{8-x}\text{Ce}_x\text{Ga}_{16+x}\text{Ge}_{30-x}$  compounds also crystallize in space group  $Pm\bar{3}n$ , like the previously mentioned compounds of  $\text{Ba}_{8-x}\text{Eu}_x\text{Ga}_{16}\text{Ge}_{30}$ . Electron counting suggests a slightly different stoichiometric ratio for the compound than Eu included clathrate compounds.

Rietveld refinements were also performed on samples with a homogeneous phase and the example of Rietveld refinement can be found in Figure 4.12 where the observed XRD pattern matches the calculated XRD pattern with a minimal difference. Through taking Rietveld refinements, one can have some understanding on the effects of Ce addition to the ternary clathrate system by studying composed elements within a compound. As expected, displacements of the host frameworks are observed as increasing the inclusion of cerium because the covalent radius of cerium is smaller than Ba. Both samples of  $\text{Ba}_{7.7}\text{Ce}_{0.3}\text{Ga}_{16.3}\text{Ge}_{29.7}$  and  $\text{Ba}_{7.0}\text{Ce}_{1.0}\text{Ga}_{17.0}\text{Ge}_{29.0}$  are carried out for the refinements where the details of refinement information are listed in Tables 4.9, 4.10, and 4.11. A decrease in the unit cell size was observed with increasing amount of cerium, that I found the lattice parameter  $a$  decreased from 10.79 Å for  $x = 0.3$  to 10.78 Å for  $x = 1.0$ . Only two samples of Ce series when  $x = 0.3$  and 1.0 were compared after the refinement, so this will definitely need a further study for a better understanding. The formation of Ce optimized ternary clathrate compounds confirms the possibility of having quaternary clathrate compounds for the future study as one of thermoelectric materials.





**Figure 4.12 Rietveld refinement of  $\text{Ba}_{7.7}\text{Ce}_{0.3}\text{Ga}_{16.3}\text{Ge}_{29.7}$ .**

When the samples were refined, fixed values were used for all occupancy factors because Ce shares a similar covalent radius with Ba with 204pm and 215pm respectively that a lack of changes in the unit cell was expected. The occupancy factors were calculated based on the nominal stoichiometric ratio. The thermal displacement parameters were also fixed with  $0.010 \text{ \AA}^2$ , the average value of parameters obtained from the samples with Eu to keep consistency of the refinements.

**Table 4.8 Refinement details of Ba<sub>7.7</sub>Ce<sub>0.3</sub>Ga<sub>16.3</sub>Ge<sub>29.7</sub> and Ba<sub>7.0</sub>Ce<sub>1.0</sub>Ga<sub>17.0</sub>Ge<sub>29.0</sub>.**

Refined formula	Ba <sub>7.7</sub> Ce <sub>0.3</sub> Ga <sub>16.3</sub> Ge <sub>29.7</sub>	Ba <sub>7.0</sub> Ce <sub>1.0</sub> Ga <sub>17.0</sub> Ge <sub>29.0</sub>
Formula weight [g/mol]	4392.37	4394.32
<i>T</i> for measurement [K]	296(2)	296(2)
$\lambda$ [Å]	0.71073	0.71073
Space group	<i>Pm</i> $\bar{3}$ <i>n</i>	<i>Pm</i> $\bar{3}$ <i>n</i>
<i>a</i> [Å]	10.791(1)	10.785(1)
<i>V</i> [Å <sup>3</sup> ]	1256.5(5)	1254.5(5)
<i>Z</i>	1	1
$\rho_{\text{cal}}$ [g/cm <sup>3</sup> ]	5.805	5.816
Rp / wRp	0.0716 / 0.1022	0.0689 / 0.1108

**Table 4.9 Atomic coordinates, equivalent thermal displacement parameters and occupancy factors of Ba<sub>7.7</sub>Ce<sub>0.3</sub>Ga<sub>16.3</sub>Ge<sub>29.7</sub>.**

Atom	site	x	y	z	U <sub>iso</sub> / Å <sup>2</sup>	occ.
Ba1	2a	0	0	0	0.010	0.96
Ba2	6d	0	1/4	1/2	0.010	0.96
Ce1	2a	0	0	0	0.010	0.04
Ce2	6d	0	1/4	1/2	0.010	0.04
Ga1	6c	1/4	0	1/2	0.010	0.35
Ge1	6c	1/4	0	1/2	0.010	0.65
Ga2	16i	0.1838(2)	0.1838(2)	0.1838(2)	0.010	0.35
Ge2	16i	0.1838(2)	0.1838(2)	0.1838(2)	0.010	0.65
Ga3	24k	0	0.3088(4)	0.1195(3)	0.010	0.35
Ge3	24k	0	0.3088(4)	0.1195(3)	0.010	0.65

**Table 4.10 Atomic coordinates, equivalent thermal displacement parameters and occupancy****factors of Ba<sub>7.0</sub>Ce<sub>1.0</sub>Ga<sub>17.0</sub>Ge<sub>29.0</sub>.**

Atom	site	x	y	z	U <sub>iso</sub> / Å <sup>2</sup>	occ.
Ba1	2a	0	0	0	0.010	0.88
Ba2	6d	0	1/4	1/2	0.010	0.88
Ce1	2a	0	0	0	0.010	0.12
Ce2	6d	0	1/4	1/2	0.010	0.12
Ga1	6c	1/4	0	1/2	0.010	0.37
Ge1	6c	1/4	0	1/2	0.010	0.63
Ga2	16i	0.1841(2)	0.1841(2)	0.1841(2)	0.010	0.37
Ge2	16i	0.1841(2)	0.1841(2)	0.1841(2)	0.010	0.63
Ga3	24k	0	0.3135(4)	0.1172(3)	0.010	0.37
Ge3	24k	0	0.3135(4)	0.1172(3)	0.010	0.63

The shortest single bond is found to be 2.47 Å for Ga/Ge2-Ga/Ge2 within Ba<sub>7.7</sub>Ce<sub>0.3</sub>Ga<sub>16.3</sub>Ge<sub>29.7</sub>, and 2.46 Å for Ga/Ge2-Ga/Ge2 within Ba<sub>7.0</sub>Ce<sub>1.0</sub>Ga<sub>17.0</sub>Ge<sub>29.0</sub>. Even though with a similar radius between the guest atoms, an increasing amount of Ce effects the size of cages, especially, tetrakaidehedra that a bond distance between Ga/Ge1 and Ga/Ge3 decreases from 2.50 Å to 2.47 Å.

**Table 4.11 Selected interatomic distances [Å] of Ba<sub>8-x</sub>Ce<sub>x</sub>Ga<sub>16+x</sub>Ge<sub>30-x</sub>.**

Interaction	Multiplicity	d / Å [x = 0.3]	d / Å [x = 1.0]
Ba/Ce1 – Ga/Ge2	8	3.4359(2)	3.4387(3)
Ba/Ce1 – Ga/Ge3	12	3.5730(4)	3.6097(4)
Ba/Ce2 – Ga/Ge1	4	3.8152(1)	3.8131(2)
Ba/Ce2 – Ga/Ge2	8	4.0106(2)	4.0071(3)
Ba/Ce2 – Ga/Ge3	8	3.6328(3)	3.5935(3)
Ga/Ge1 – Ga/Ge3	4	2.4980(2)	2.4693(4)
Ga/Ge2 – Ga/Ge2	1	2.4735(3)	2.4628(4)
Ga/Ge2 – Ga/Ge3	3	2.4971(4)	2.5319(5)
Ga/Ge3 – Ga/Ge1	1	2.4980(4)	2.4693(4)
Ga/Ge3 – Ga/Ge2	2	2.4971(3)	2.5319(4)
Ga/Ge3 – Ga/Ge3	1	2.5790(4)	2.5278(5)

### 4.3.2 Thermal analysis and EDX analysis

It is important to take a thermal analysis with DSC because the melting point obtained through the measurement is taking an important role in the heating profile of the reaction. These measurements were carried out under a flow of helium to avoid any oxidization. For the  $\text{Ba}_{8-x}\text{Ce}_x\text{Ga}_{16+x}\text{Ge}_{30-x}$  compounds, three samples of  $x = 0.3, 0.5$  and  $1.0$  were used for the measurements (Fig. 4.12). It was found that the melting points of  $\text{Ba}_{8-x}\text{Ce}_x\text{Ga}_{16+x}\text{Ge}_{30-x}$  are between  $973^\circ\text{C}$  and  $975^\circ\text{C}$ , and the values are reasonable compared to the ternary compounds of  $975^\circ\text{C}$ . The weak endothermic peaks appeared at  $770^\circ\text{C}$ , which may be attributed from an excess barium or a phase change.

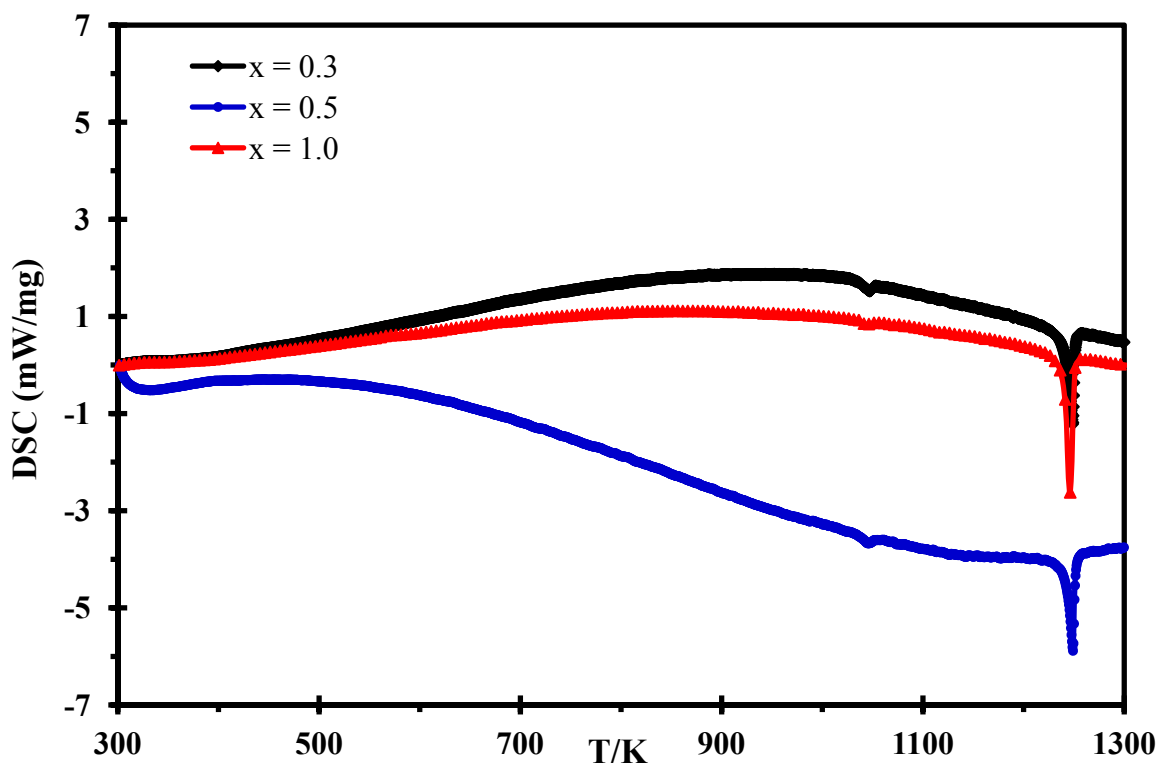


Figure 4.13 DSC curves of  $\text{Ba}_{8-x}\text{Ce}_x\text{Ga}_{16+x}\text{Ge}_{30-x}$  when  $x = 0.3, 0.5,$  and  $1.0$ .

All confirmed pure samples were taken for EDX analysis to obtain elemental

compositions of the  $Ba_{8-x}Ce_xGa_{16+x}Ge_{30-x}$  compounds in atomic percentages, and they were compared with calculated atomic percentages. Various spots were picked randomly for the analysis in order to avoid any bias. The atomic percentages of elements in Table 4.18 list the EDX data for  $Ba_{7.5}Ce_{0.5}Ga_{16.5}Ge_{29.5}$  where the average atomic percentages of elements are 13.8: 1.0: 29.5: 55.7 similar to the calculated atomic percentages, 13.9: 0.9: 30.6: 54.6. Nominal compositions of  $x = 0.3$ , and 1.0 are also examined with EDX analysis where 13.9: 0.5: 29.1: 56.4 for  $Ba_{7.7}Ce_{0.3}Ga_{16.3}Ge_{29.7}$ , and 13.7: 1.6: 31.7: 54.0 for  $Ba_{7.0}Ce_{1.0}Ga_{16}Ge_{29}$  were obtained as shown in Table 4.13.

**Table 4.12 Atomic percentages of elements from EDX data for  $Ba_{7.5}Ce_{0.5}Ga_{16.5}Ge_{29.5}$ .**

Element	Calculated	1	2	3	4	5	Avg.
Ba	13.9	12.9	13.2	14.3	14.5	14.3	13.8
Ce	0.9	1.1	0.2	1.8	1.0	1.8	1.0
Ga	30.6	28.5	29.5	29.8	29.1	29.8	29.5
Ge	54.6	57.5	57.0	54.1	55.4	54.1	55.7

**Table 4.13 Average element composition of the  $Ba_{8-x}Ce_xGa_{16+x}Ge_{30-x}$  compounds. The actual composition was obtained by EDX analysis.**

Nominal Composition	Ce content x		Average Composition (atomic %)			
	Nominal	Actual	Ba	Ce	Ga	Ge
$Ba_{7.7}Ce_{0.3}Ga_{16}Ge_{30}$	0.3	0.3	13.9	0.5	29.1	56.4
$Ba_{7.5}Ce_{0.5}Ga_{16}Ge_{30}$	0.5	0.5	13.8	1.0	29.5	55.7
$Ba_{7.0}Ce_{1.0}Ga_{16}Ge_{30}$	1.0	0.9	13.7	1.6	31.7	54.0

### 4.3.3 Physical property measurements

For Seebeck and electrical conductivity measurements, phase pure sample of  $\text{Ba}_{8-x}\text{Ce}_x\text{Ga}_{16+x}\text{Ge}_{30-x}$  with  $x = 0.3, 0.5$  and  $1.0$  were prepared as cold-pressed pellets in the shape of bars, where the dimensions are  $13 \times 2 \times 2$  mm. The pellets were annealed for 12 hours at  $440^\circ\text{C}$ , the maximum temperature of the measurements. The sample with  $x = 0.3$  was also prepared as a hot-pressed pellet. As mentioned earlier with Eu composed quaternary compounds, a hot-pressed pellet typically shows dramatic improvements in the Seebeck coefficient, electrical conductivity and power factor compared to a cold-pressed pellet of the same. In the case of Ce containing samples, both cold-pressed pellets and a hot-pressed pellet were compared in the same graph. The electrical conductivity measurements of Ce clathrates vary between  $0.2 \Omega^{-1}\text{cm}^{-1}$  and  $3.7 \Omega^{-1}\text{cm}^{-1}$  at room temperature.

In the electrical conductivity comparison, there isn't a huge difference in values between cold-pressed and hot-pressed samples of  $x = 0.3$  samples that the value changed from  $0.2 \Omega^{-1}\text{cm}^{-1}$  to  $3.7 \Omega^{-1}\text{cm}^{-1}$  at room temperature. However, there is a higher chance of increasing the electrical conductivity with increasing the amounts of Ce in the system because they cause changes in the position and size of the unit cell. Displacement of atoms in clathrates is closely related to the band gap of a material where an increase of impurities forms a better heat resistivity by adjustable band gaps. A hot-pressed pellet of  $x = 0.3$  does not show a good electrical conductivity compared to a cold-pressed Eu containing clathrates of the same amount, as  $4.5 \Omega^{-1}\text{cm}^{-1}$  for  $\text{Ba}_{7.7}\text{Ce}_{0.3}\text{Ga}_{16.3}\text{Ge}_{29.7}$  and  $3.3 \Omega^{-1}\text{cm}^{-1}$  for  $\text{Ba}_{7.7}\text{Eu}_{0.3}\text{Ga}_{16}\text{Ge}_{30}$ . Low electrical conductivity of hot-pressed  $\text{Ba}_{7.7}\text{Ce}_{0.3}\text{Ga}_{16.3}\text{Ge}_{29.7}$  may

be resulted from a pellet itself as it was prepared outside the lab. Therefore, lacking samples of Ce included compounds cause difficult to conclude any results.

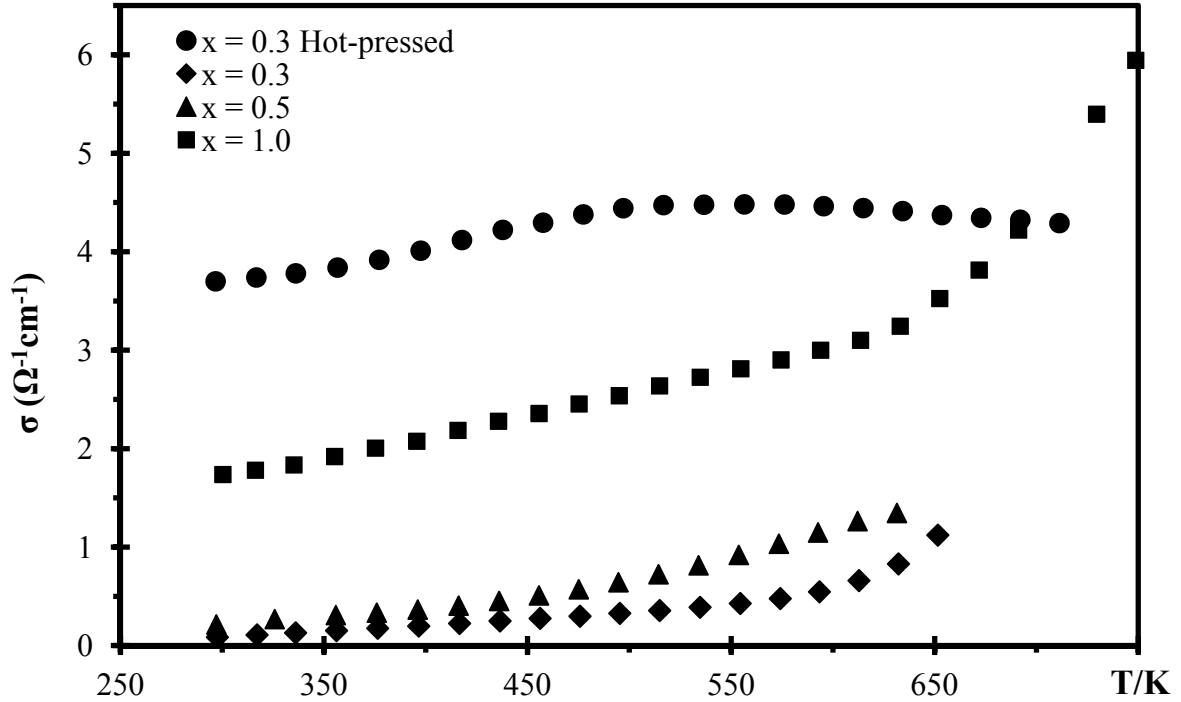


Figure 4.14 Electrical conductivity of  $\text{Ba}_{8-x}\text{Ce}_x\text{Ga}_{16+x}\text{Ge}_{30-x}$ .

Unlike the electrical conductivity comparison, the Seebeck coefficient of a hot-pressed pellet showed a great improvement as can be seen in Figure 4.15. All prepared samples were to be found n-type semiconductors, and the hot-pressed pellet of  $x = 0.3$  exhibited the maximum value of  $-734 \mu\text{V}\cdot\text{K}^{-1}$  at  $440^\circ\text{C}$  while only  $-123 \mu\text{V}\cdot\text{K}^{-1}$  was achieved at  $340^\circ\text{C}$  for  $x = 0.5$ ,  $-256 \mu\text{V}\cdot\text{K}^{-1}$  for  $\text{Ba}_{7.7}\text{Eu}_{0.3}\text{Ga}_{16}\text{Ge}_{30}$ , and  $-208 \mu\text{V}\cdot\text{K}^{-1}$  for  $\text{Ba}_{7.7}\text{Yb}_{0.3}\text{Ga}_{16}\text{Ge}_{30}$ .



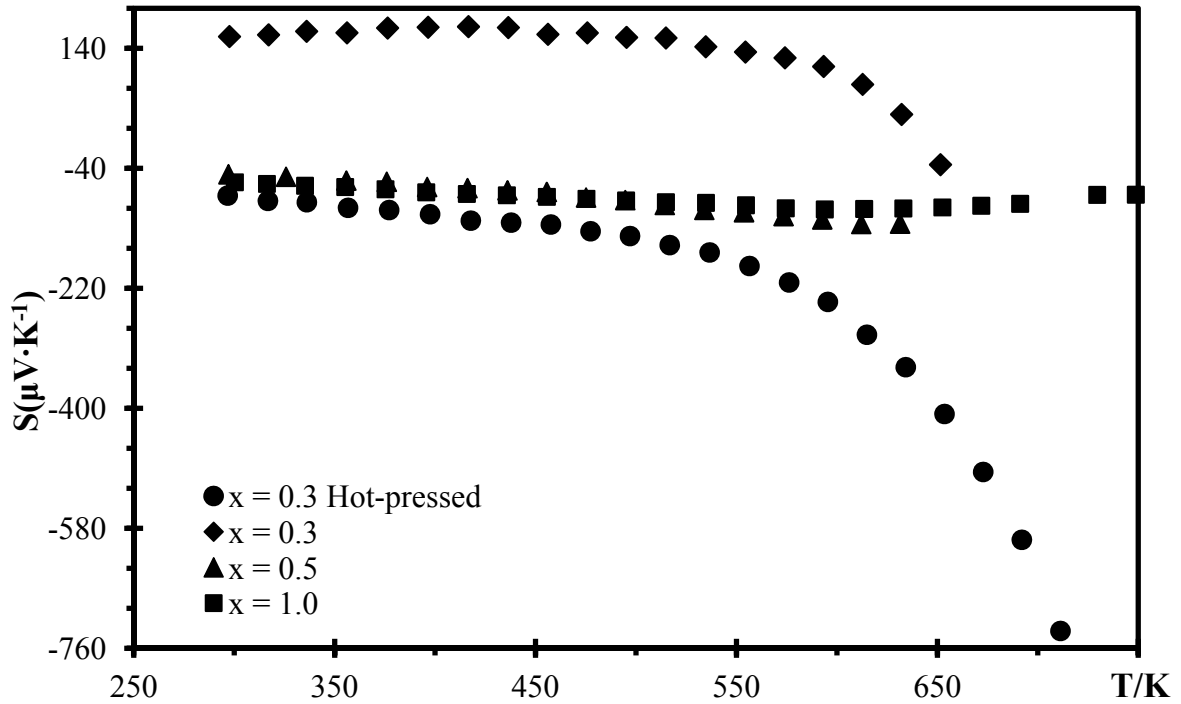


Figure 4.15 Seebeck coefficient of  $\text{Ba}_{8-x}\text{Ce}_x\text{Ga}_{16+x}\text{Ge}_{30-x}$ .

Because of the high value of Seebeck coefficient, the power factor of  $\text{Ba}_{7.7}\text{Ce}_{0.3}\text{Ga}_{16.3}\text{Ge}_{29.7}$  is also much higher than that of the cold-pressed samples. The maximum power factor value of  $\text{Ba}_{7.7}\text{Ce}_{0.3}\text{Ga}_{16.3}\text{Ge}_{29.7}$  was  $2.3 \mu\text{Wcm}^{-1}\text{K}^{-2}$  at  $440^\circ\text{C}$ , and cold-pressed pellets remained below  $0.02 \mu\text{Wcm}^{-1}\text{K}^{-2}$ .

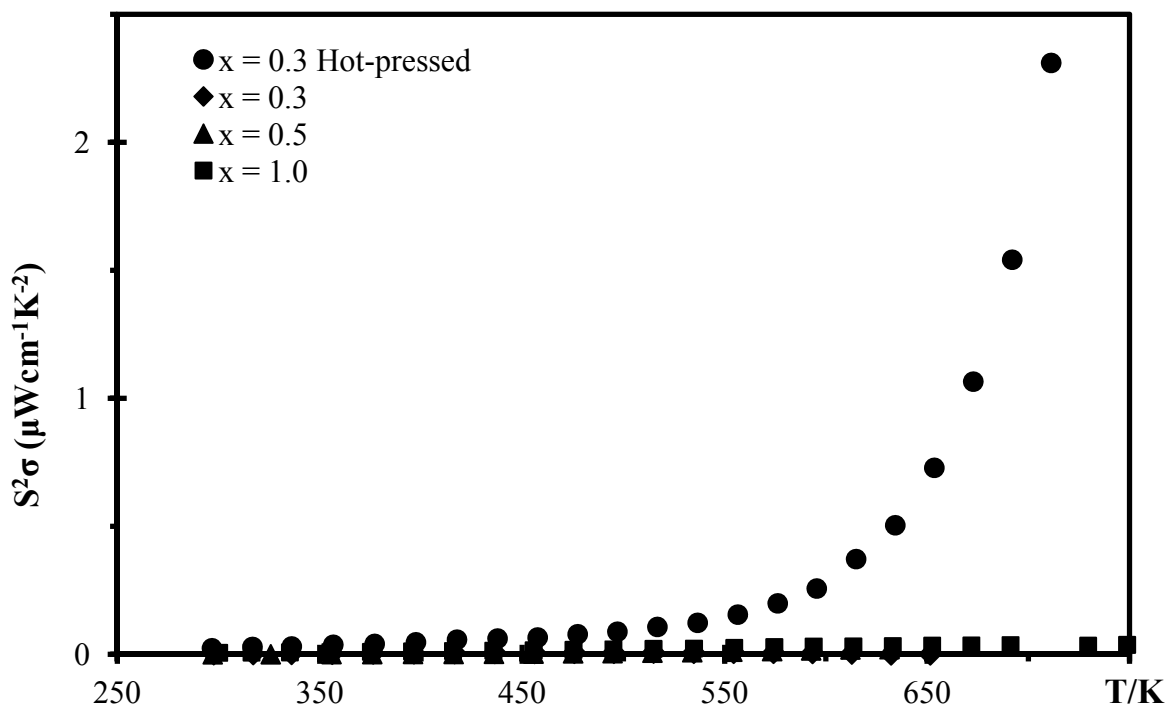


Figure 4.16 Power factor of  $\text{Ba}_{8-x}\text{Ce}_x\text{Ga}_{16+x}\text{Ge}_{30-x}$ .

#### 4.3.4 Conclusions

Only three variable compositions of cerium,  $x = 0.3, 0.5$  and  $1.0$  were achieved as homogeneous quaternary compounds. However, the formation of cerium optimized clathrates was successful, so that further developments and analytical studies can be done in the future.

Previously mentioned comparison of physical properties between cold-pressed samples and a hot-pressed sample enlighten the direction of study because a huge improvement was observed. However, cutting a bar out of a disk shaped pellet obtained after hot-pressing is challenging as the compound itself is brittle than any other thermoelectric materials.

## 4.4 Structure and properties of $\text{Ba}_{8-x}\text{La}_x\text{Ga}_{16+x}\text{Ge}_{30-x}$

### 4.4.1 Rietveld refinements

The crystal structure of  $\text{Ba}_{8-x}\text{La}_x\text{Ga}_{16+x}\text{Ge}_{30-x}$  also shares the same space group as other two quaternary clathrate compounds mentioned earlier in this chapter. The  $\text{Ba}_{8-x}\text{La}_x\text{Ga}_{16+x}\text{Ge}_{30-x}$  compounds with  $x = 0.2, 0.3, 0.4$  and  $1.0$  were prepared, and their homogeneities confirmed via XRD analysis before taking any further actions. However, only the Rietveld refinements of the compounds with  $x = 0.2$  and  $0.3$  will be discussed in this paper. Similar to the compounds of either Eu or Ce substituted, lanthanum optimized compounds exhibit the same pattern except changes in values.

Several parameters were considered during the refinement as the program is sensitive with just one parameter. The atomic coordinates, equivalent thermal displacement parameters, and occupancy were the main parameters to be refined to acquire right information. The Rietveld refinement of  $\text{Ba}_{7.8}\text{La}_{0.2}\text{Ga}_{16.2}\text{Ge}_{29.8}$  is shown in Figure 4.17 where the observed pattern matches the calculated pattern of XRD.

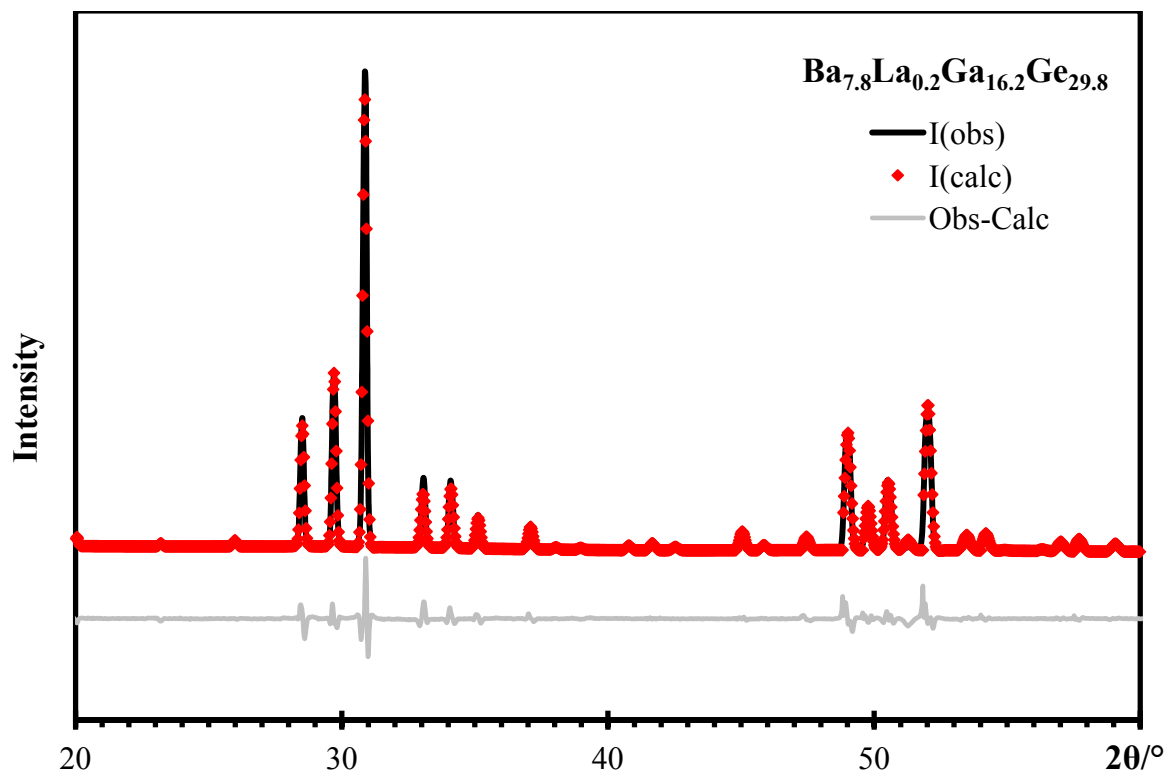


Figure 4.17 Rietveld refinement of  $\text{Ba}_{7.8}\text{La}_{0.2}\text{Ga}_{16.2}\text{Ge}_{29.8}$ .

Both volumes of  $\text{Ba}_{7.8}\text{La}_{0.2}\text{Ga}_{16.2}\text{Ge}_{29.8}$  and  $\text{Ba}_{7.7}\text{La}_{0.3}\text{Ga}_{16.3}\text{Ge}_{29.7}$  are  $1254 \text{ \AA}^3$  that there isn't a huge change with increasing lanthanum amounts in clathrates. This may be due to a similar atomic size between Ba and La as they are neighboring atoms. And their scattered X-rays are almost the same that the refinements of these compounds exhibit the same as the ternary clathrates,  $\text{Ba}_8\text{Ga}_{16}\text{Ge}_{30}$  where the volume is also  $1254 \text{ \AA}^3$ <sup>34</sup> As only the small amount of lanthanum is added, most of  $2a$  and  $6d$  sites are occupied by Ba atoms. Both thermal displacement parameters and occupancy factors were fixed because of a similar atomic size between the guest atoms. And the  $U_{iso}$  value of  $0.010 \text{ \AA}^2$  was from the value obtained from the average  $U_{iso}$  for samples containing Eu. The details of refinements are shown in Table 4.15.

**Table 4.14 Refinement details of Ba<sub>7.8</sub>La<sub>0.2</sub>Ga<sub>16.2</sub>Ge<sub>29.8</sub> and Ba<sub>7.7</sub>La<sub>0.3</sub>Ga<sub>16.3</sub>Ge<sub>29.7</sub>.**

Refined formula	Ba <sub>7.8</sub> La <sub>0.2</sub> Ga <sub>16.2</sub> Ge <sub>29.8</sub>	Ba <sub>7.7</sub> La <sub>0.3</sub> Ga <sub>16.3</sub> Ge <sub>29.7</sub>
Formula weight [g/mol]	4345.36	4365.78
<i>T</i> for measurement [K]	296(2)	296(2)
$\lambda$ [Å]	0.71073	0.71073
Space group	<i>Pm</i> $\bar{3}$ <i>n</i>	<i>Pm</i> $\bar{3}$ <i>n</i>
<i>a</i> [Å]	10.78506(6)	10.78494(6)
<i>V</i> [Å <sup>3</sup> ]	1254.49(2)	1254.45(2)
<i>Z</i>	1	1
$\rho_{\text{cal}}$ [g/cm <sup>3</sup> ]	5.752	5.779
Rp / wRp	0.0567 / 0.0830	0.0625 / 0.0849

**Table 4.15 Atomic coordinates, equivalent thermal displacement parameters and occupancy factors of Ba<sub>7.8</sub>La<sub>0.2</sub>Ga<sub>16.2</sub>Ge<sub>29.8</sub>.**

Atom	site	x	y	z	Uiso / Å <sup>2</sup>	occ.
Ba1	2a	0	0	0	0.010	0.98
Ba2	6d	0	1/4	1/2	0.010	0.98
La1	2a	0	0	0	0.010	0.02
La2	6d	0	1/4	1/2	0.010	0.02
Ga1	6c	1/4	0	1/2	0.010	0.35
Ge1	6c	1/4	0	1/2	0.010	0.65
Ga2	16i	0.1851(2)	0.1851(2)	0.1851(2)	0.010	0.35
Ge2	16i	0.1851(2)	0.1851(2)	0.1851(2)	0.010	0.65
Ga3	24k	0	0.3081(3)	0.1192(2)	0.010	0.35
Ge3	24k	0	0.3081(3)	0.1192(2)	0.010	0.65

**Table 4.16 Atomic coordinates, equivalent thermal displacement parameters and occupancy factors of Ba<sub>7.7</sub>La<sub>0.3</sub>Ga<sub>16.3</sub>Ge<sub>29.7</sub>.**

Atom	site	x	y	z	U <sub>iso</sub> / Å <sup>2</sup>	occ.
Ba1	2a	0	0	0	0.010	0.96
Ba2	6d	0	1/4	1/2	0.010	0.96
La1	2a	0	0	0	0.010	0.04
La2	6d	0	1/4	1/2	0.010	0.04
Ga1	6c	1/4	0	1/2	0.010	0.35
Ge1	6c	1/4	0	1/2	0.010	0.65
Ga2	16i	0.1836(2)	0.1836(2)	0.1836(2)	0.010	0.35
Ge2	16i	0.1836(2)	0.1836(2)	0.1836(2)	0.010	0.65
Ga3	24k	0	0.3074(3)	0.1200(2)	0.010	0.35
Ge3	24k	0	0.3074(3)	0.1200(2)	0.010	0.65

The shortest interatomic distance of Ba<sub>7.8</sub>La<sub>0.2</sub>Ga<sub>16.2</sub>Ge<sub>29.8</sub> was 2.49 Å of Ga/Ge1-Ga/Ge3 bond whereas Ga/Ge2-Ga/Ge3 bond was showing the shortest distance for Ba<sub>7.8</sub>La<sub>0.2</sub>Ga<sub>16.2</sub>Ge<sub>29.8</sub> with the same value (Table. 4.14).

**Table 4.17 Selected interatomic distances [ $\text{\AA}$ ] of  $\text{Ba}_{8-x}\text{La}_x\text{Ga}_{16+x}\text{Ge}_{30-x}$  when  $x = 0.2$  and  $0.3$ .**

Interaction	Multiplicity	$d / \text{\AA} [x = 0.2]$	$d / \text{\AA} [x = 0.3]$
Ba/La1 – Ga/Ge2	8	3.4575(1)	3.4295(1)
Ba/La1 – Ga/Ge3	12	3.5627(1)	3.5586(1)
Ba/La2 – Ga/Ge1	4	3.8131(1)	3.8131(1)
Ba/La2 – Ga/Ge2	8	4.0012(1)	4.0098(1)
Ba/La2 – Ga/Ge3	8	3.6341(1)	3.6413(1)
Ga/Ge1 – Ga/Ge3	4	2.5049(1)	2.5065(1)
Ga/Ge2 – Ga/Ge2	1	2.4251(1)	2.4811(1)
Ga/Ge2 – Ga/Ge3	3	2.4999(1)	2.4847(1)
Ga/Ge3 – Ga/Ge1	1	2.5049(1)	2.5065(1)
Ga/Ge3 – Ga/Ge2	2	2.4999(1)	2.4847(1)
Ga/Ge3 – Ga/Ge3	1	2.5709(1)	2.5875(1)

#### 4.2.2 Thermal analysis and EDX analysis

The melting points of  $\text{Ba}_{8-x}\text{La}_x\text{Ga}_{16+x}\text{Ge}_{30-x}$  are  $976^\circ\text{C}$  and  $978^\circ\text{C}$  for  $x = 0.3$  and  $0.4$ , respectively, (Fig. 4.17) which are comparable with the melting point of ternary clathrate compounds of  $974^\circ\text{C}$ <sup>21</sup> and other quaternary clathrate compounds of lanthanoid. The melting points of Eu containing clathrates and Ce containing clathrates are  $977^\circ\text{C}$  and  $975^\circ\text{C}$  respectively.

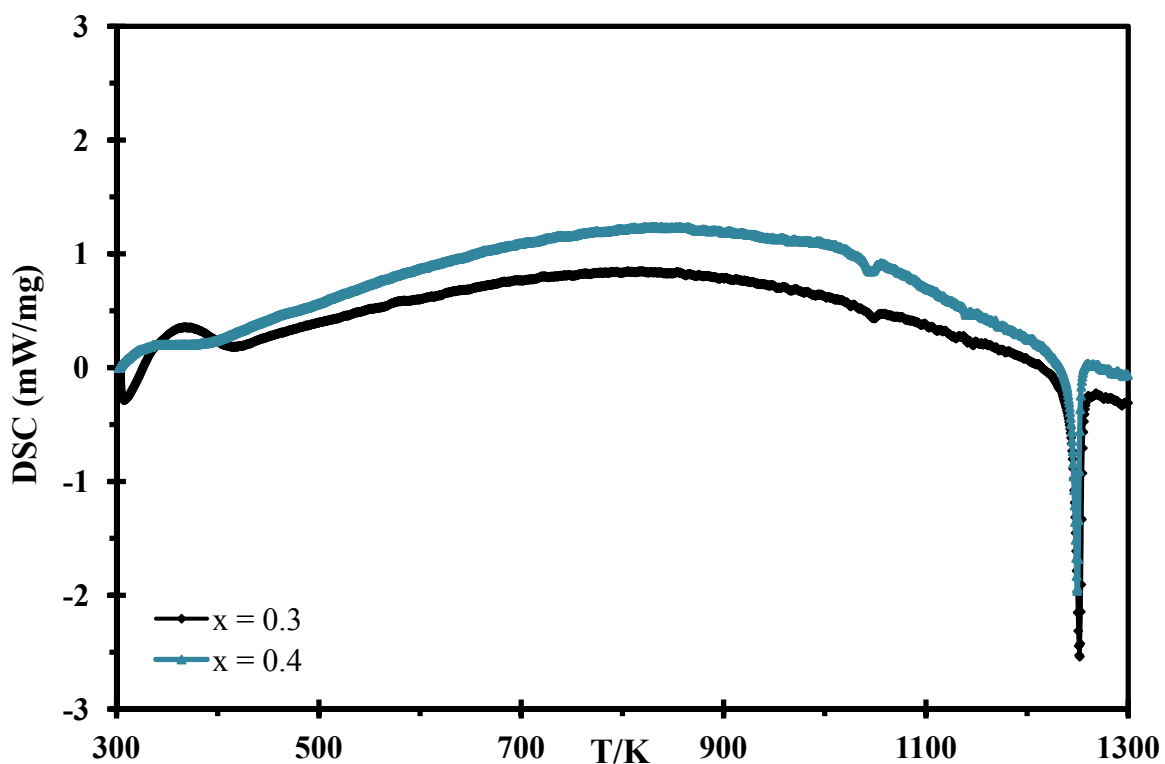


Figure 4.18 DSC curves of  $\text{Ba}_{8-x}\text{La}_x\text{Ga}_{16+x}\text{Ge}_{30-x}$  when  $x = 0.3$  and  $0.4$ .

While homogeneous compounds of La were analyzed via XRD and thermal analysis, they were also used for EDX analysis. Similar to the previous samples, random spots were picked for the analysis, and atomic percentages were obtained. The actual content  $x$  of La was calculated using atomic percentages for  $x = 0.3$ ,  $0.4$  and  $1.0$ . The atomic percentages of



elements can be obtained through EDX data and Table 4.18 shows the EDX data for  $\text{Ba}_{7.7}\text{La}_{0.3}\text{Ga}_{16.3}\text{Ge}_{29.7}$  where the average atomic percentages of elements are 14.3: 0.6: 29.7: 55.5. Seven random spots are picked for getting the data. The atomic percentages of the frameworks changed slightly, but the values for the guests showed the same as the calculated. Nominal compositions of  $x = 0.4$  and  $1.0$  are also examined with EDX analysis where 14.3: 0.7: 29.5: 55.4 for  $\text{Ba}_{7.6}\text{La}_{0.4}\text{Ga}_{16.4}\text{Ge}_{29.6}$  and 14.1: 1.5: 29.0: 55.4 for  $\text{Ba}_{7.0}\text{Eu}_{1.0}\text{Ga}_{17}\text{Ge}_{29}$  were obtained as shown in Table 4.19.

**Table 4.18 Atomic percentages of elements from EDX data for  $\text{Ba}_{7.7}\text{La}_{0.3}\text{Ga}_{16.3}\text{Ge}_{29.7}$ .**

Element	Calculated	1	2	3	4	5	6	7	Avg.
Ba	14.3	14.7	13.3	15.1	15.2	12.3	15.4	13.9	14.3
La	0.6	0.6	0.3	0.5	0.4	0.4	0.9	1.3	0.6
Ga	30.2	29.2	30.7	29.4	30.3	29.6	28.6	29.8	29.7
Ge	55.0	55.5	55.7	55.0	54.1	57.7	55.2	55.1	55.5

**Table 4.19 Average element composition of the  $\text{Ba}_{8-x}\text{La}_x\text{Ga}_{16+x}\text{Ge}_{30-x}$  compounds. The actual composition was obtained by EDX analysis.**

Nominal Composition	La content x		Average Composition (atomic %)			
	Nominal	Actual	Ba	La	Ga	Ge
$\text{Ba}_{7.7}\text{La}_{0.3}\text{Ga}_{16.3}\text{Ge}_{29.7}$	0.3	0.3	14.3	0.6	29.7	55.5
$\text{Ba}_{7.6}\text{La}_{0.4}\text{Ga}_{16.4}\text{Ge}_{29.6}$	0.4	0.4	14.3	0.7	29.5	55.4
$\text{Ba}_{7.0}\text{La}_{1.0}\text{Ga}_{17}\text{Ge}_{29}$	1.0	0.8	14.1	1.5	29.0	55.4

#### 4.4.3 Physical property measurements

The cold-pressed pellets with the dimensions are  $13 \times 2 \times 2$  mm were made with Phase pure sample of  $\text{Ba}_{8-x}\text{Ce}_x\text{Ga}_{16+x}\text{Ge}_{30-x}$ , and pellets were placed in a furnace of ULVAC-RICO ZEM-3 after being annealed for 12 hours at  $440^\circ\text{C}$ . The electrical conductivity, Seebeck coefficient and power factor were then measured for physical properties. Four samples with  $x = 0.2, 0.3, 0.4$  and  $1.0$  were used for the measurements.

In Figure 4.18, the electrical conductivity of samples with  $x = 0.2, 0.3,$  and  $0.4$  are compared.  $\text{Ba}_{7.6}\text{La}_{0.4}\text{Ga}_{16.4}\text{Ge}_{29.6}$  showed the highest value of  $1.0 \Omega^{-1}\text{cm}^{-1}$  at  $340^\circ\text{C}$ . And the electrical conductivity of a sample with  $x = 1.0$  was found to show the maximum value of  $420 \Omega^{-1}\text{cm}^{-1}$  at the room temperature and decreased as increasing the temperature. Decreasing electrical conductivity indicates a metallic behavior compared to other La containing clathrates where the values increase with increasing temperature. The physical properties of  $\text{Ba}_{7.0}\text{La}_{1.0}\text{Ga}_{17}\text{Ge}_{29}$  are plotted separately in Figure 4.19. In terms of cold-pressed samples with  $x = 0.3, 3.3 \Omega^{-1}\text{cm}^{-1}$  and  $1.1 \Omega^{-1}\text{cm}^{-1}$  are obtained for Eu and Ce containing clathrates respectively whereas  $0.4 \Omega^{-1}\text{cm}^{-1}$  for La-clathrates. Lanthanum contained clathrates except  $x = 1.0$  shows the lowest electrical conductivity among other optimized quaternary clathrates with Ln because La is a neighboring atom to Ba that there is not a big difference in the atomic size. Therefore, the substitution of La does not improve the electrical conductivity compared to other Ln substitutions for the inclusion of small amounts.

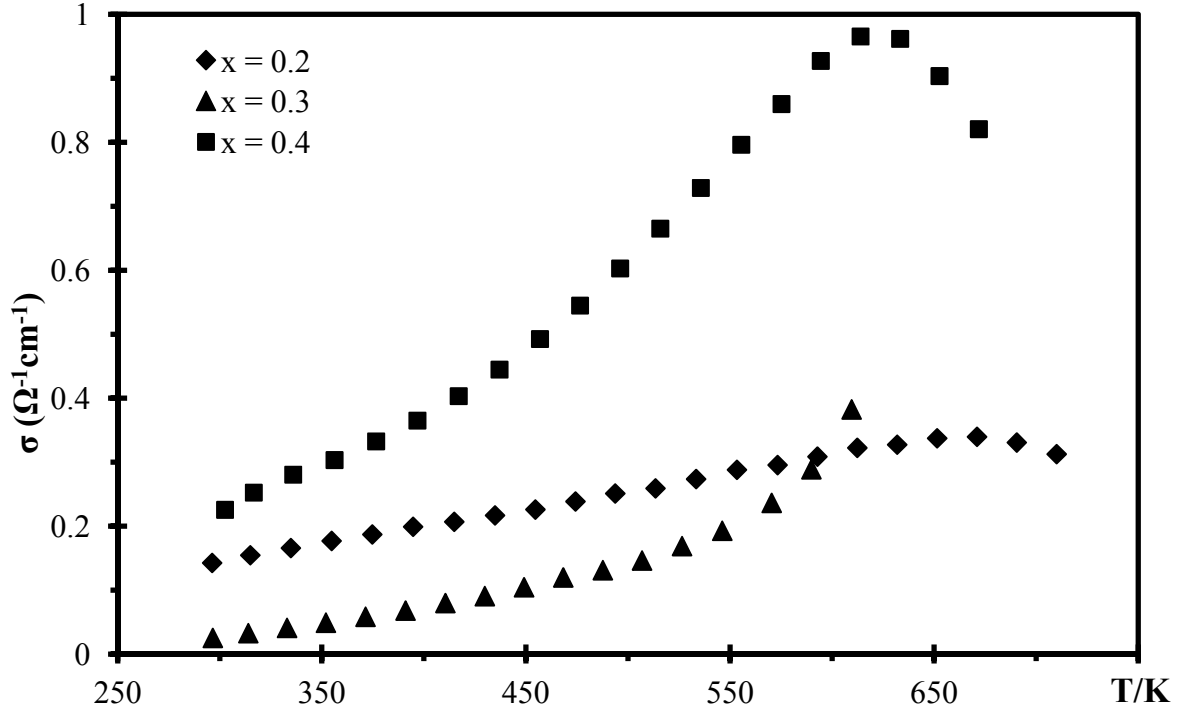


Figure 4.19 Electrical conductivity of  $\text{Ba}_{8-x}\text{La}_x\text{Ga}_{16+x}\text{Ge}_{30-x}$ .

Even though, the  $\text{Ba}_{7.0}\text{La}_{1.0}\text{Ga}_{17}\text{Ge}_{29}$  compound was not hot-pressed, its Seebeck coefficient and electrical conductivity are much higher than those of the other samples. It achieved a Seebeck coefficient of  $-760 \mu\text{V}\cdot\text{K}^{-1}$  at  $440^\circ\text{C}$ , compared to  $-670 \mu\text{V}\cdot\text{K}^{-1}$ ,  $-535 \mu\text{V}\cdot\text{K}^{-1}$ , and  $-135 \mu\text{V}\cdot\text{K}^{-1}$  for  $x = 0.2, 0.3$  and  $0.4$  respectively. The second measurements of the Seebeck coefficient, electrical conductivity, and power factor for  $\text{Ba}_{7.0}\text{La}_{1.0}\text{Ga}_{17}\text{Ge}_{29}$  have carried out for reproducibility, and both the trend and values are the same. Even though a La atom shares a similar atomic size with a Ba atom, increasing amounts of La in clathrates while decreasing the amount of Ba improve physical properties because of their charge differences and the unit cell size. La atoms donate three electrons whereas Ba atoms donate two electrons, which cause an active interaction between the guest atoms and the frameworks. Moreover, La atoms are smaller than Ba atoms, which can shrink the unit cell

as the amount of La increases.

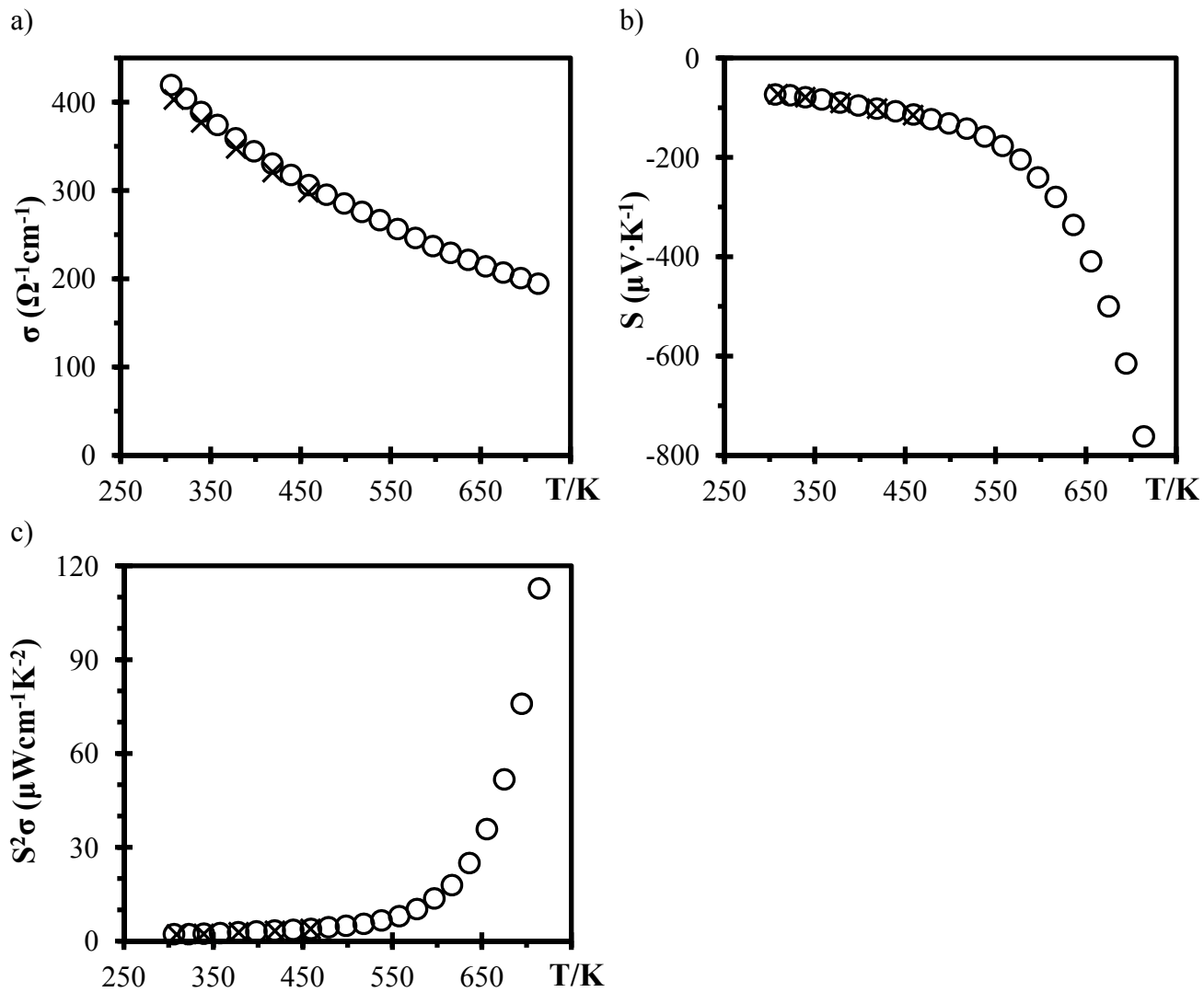
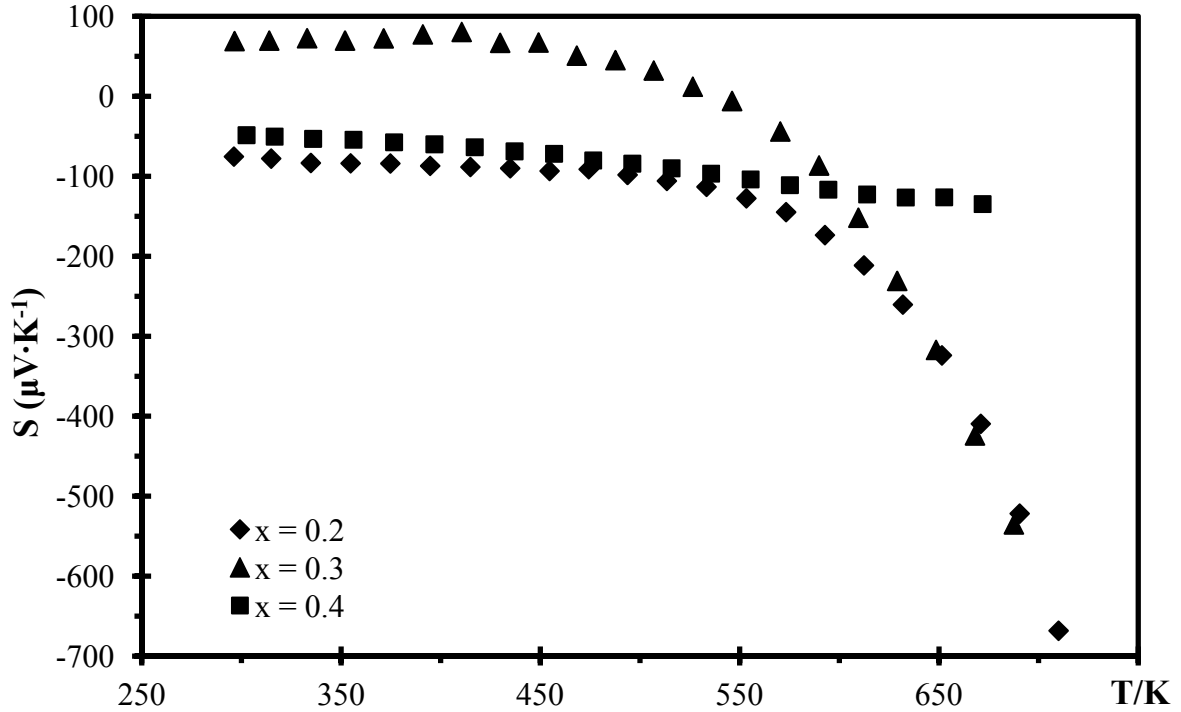


Figure 4.20 Physical properties of  $\text{Ba}_{7.0}\text{La}_{1.0}\text{Ga}_{17}\text{Ge}_{29}$  where a) electrical conductivity, b)

Seebeck coefficient and c) power factor where  $\times$  marks are reproduced data.



**Figure 4.21 Seebeck coefficient of  $\text{Ba}_{8-x}\text{La}_x\text{Ga}_{16+x}\text{Ge}_{30-x}$ .**

The sample with  $x = 1.0$  exhibits a high power factor of  $110 \mu\text{Wcm}^{-1}\text{K}^{-2}$ . The power factor increases rapidly with increasing temperature, comparable to the  $x = 0.2$  and  $0.3$  samples, where much lower maximum values of  $0.14 \mu\text{Wcm}^{-1}\text{K}^{-2}$  and  $0.21 \mu\text{Wcm}^{-1}\text{K}^{-2}$  were obtained (Fig. 4.22). The power factor values indicate that a high amount of La contained clathrates to be an excellent candidate for a TE material.

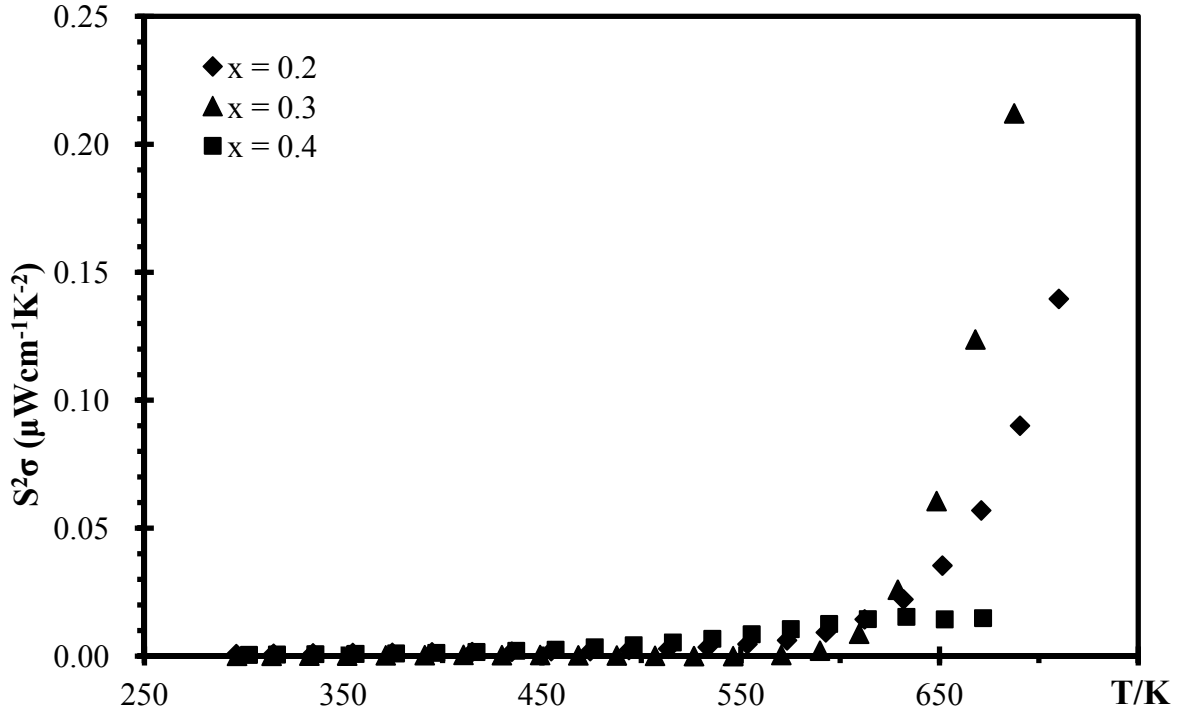


Figure 4.22 Power factor of  $\text{Ba}_{8-x}\text{La}_x\text{Ga}_{16+x}\text{Ge}_{30-x}$ .

#### 4.4.4 Conclusions

The newly made  $\text{Ba}_{8-x}\text{La}_x\text{Ga}_{16+x}\text{Ge}_{30-x}$  compounds are revealed. The substitution of La in  $\text{Ba}_{8-x}\text{La}_x\text{Ga}_{16+x}\text{Ge}_{30-x}$  was successful till  $x = 1.0$  while following the same reaction profile as other samples. The addition of small amounts of La does not affect either the unit cell or physical properties where the refinements of both  $x = 0.2$  and  $0.3$  samples show the same lattice parameter as the ternary clathrates,  $10.785 \text{ \AA}$ . However, increased amounts of La definitely change physical properties where both the Seebeck coefficient and electrical conductivity have improved significantly for  $x = 1.0$  compared to other La substituted clathrates.

## 5 Conclusion

During the research project of clathrates, the following new quaternary compounds were synthesized.

1.  $\text{Ba}_{8-x}\text{Eu}_x\text{Ga}_{16}\text{Ge}_{30}$
2.  $\text{Ba}_{8-x}\text{Ce}_x\text{Ga}_{16+x}\text{Ge}_{30-x}$
3.  $\text{Ba}_{8-x}\text{La}_x\text{Ga}_{16+x}\text{Ge}_{30-x}$

However, formation of phase pure compounds was challenging, so that not all variation of  $x$  was acquired.

X-ray diffraction analysis along with the Rietveld refinement was performed to study the structure and bonding of these compounds even though all quaternary compounds have the same space group as the ternary clathrate,  $\text{Ba}_8\text{Ga}_{16}\text{Ge}_{30}$ . This was to understand the effect of guest type and size on the clathrate structure compared to the ternary compounds. The common findings of all three series of quaternary compounds are that substituted lanthanoid elements prefer to occupy the  $2a$  site because of their sizes.

The ternary clathrate of  $\text{Ba}_8\text{Ga}_{16}\text{Ge}_{30}$ <sup>38</sup> is used as a reference to perform the Rietveld refinements of Ln containing quaternary clathrates where the lattice parameter  $a$  of the reference is 10.785 Å. The Eu series are showing a trend for  $0.2 \leq x \leq 0.4$  as the lattice parameter decreases with increasing the amount of Eu because the Eu atom is smaller than a Ba atom. Both samples of Eu series with  $x = 0.2$  and  $0.5$  have Ga/Ge2-Ga/Ge3 bond as the shortest interatomic distance while a sample of  $x = 1.0$  has Ga/Ge1-Ga/Ge3 bond as the shortest. On the other hand, both Ce and La do not show any relations.

The refinements of La series are done for  $x = 0.2$  and  $0.3$ , and the neighboring atom of La to Ba exhibits a similar behavior when a small amount of La is added to clathrates. However, this may change if the amount of La increases because a large replacement of Ba with La creates displacement of atoms causing a shrink of the unit cell. Moreover, as lanthanoid has a smaller atomic size than Ba, they prefer to occupy the smaller cage. There are only two samples being available to compare for Ce series and La series, so more variations are needed to confirm any types of trend.

Comparing the electrical conductivity for Ln containing clathrates, most samples are showing rather small values close to zero at room temperature even though the conductivity increases with increasing temperature except  $\text{Ba}_{7.0}\text{La}_{1.0}\text{Ga}_{17}\text{Ge}_{29}$  sample where the electrical conductivity decreases with increasing temperature.  $\text{Ba}_{7.0}\text{La}_{1.0}\text{Ga}_{17}\text{Ge}_{29}$  shows the highest value  $420 \Omega^{-1}\text{cm}^{-1}$ , whereas other samples of Ln clathrates exhibit values between  $0.3 \Omega^{-1}\text{cm}^{-1}$  and  $6 \Omega^{-1}\text{cm}^{-1}$ . While both Ce and La containing samples show a trend where the electrical conductivity increases with increasing the amount of Ln in clathrates, hot-pressed samples improve the property better than cold-pressed samples.  $1.1 \Omega^{-1}\text{cm}^{-1}$  and  $4.5 \Omega^{-1}\text{cm}^{-1}$  are achieved for cold-pressed and hot-pressed  $\text{Ba}_{7.7}\text{Ce}_{0.3}\text{Ga}_{16.7}\text{Ge}_{29.3}$  sample respectively, compared to  $2.6 \Omega^{-1}\text{cm}^{-1}$  and  $250 \Omega^{-1}\text{cm}^{-1}$  for  $\text{Ba}_{7.5}\text{Eu}_{0.5}\text{Ga}_{16}\text{Ge}_{30}$ .

Most formed clathrates are found to be n-type semiconductors as their Seebeck coefficient values lie between  $-60 \mu\text{V}\cdot\text{K}^{-1}$  and  $-760 \mu\text{V}\cdot\text{K}^{-1}$  of  $\text{Ba}_{7.0}\text{La}_{1.0}\text{Ga}_{17}\text{Ge}_{29}$  sample, which shows the highest Seebeck coefficient. A hot-pressed compound for  $x = 0.3$  shows fairly high values of Seebeck coefficients, but not a very high conductivity, so the material may not have a good efficiency as thermoelectric materials. Definitely, hot-pressed samples



exhibit better Seebeck coefficient. An increase in both electrical conductivity and Seebeck coefficient plays an important role to calculate the power factor, which decides the goodness of a material as thermoelectric. The maximum obtained for the power factor is  $120 \mu\text{Wcm}^{-1}\text{K}^{-2}$  for  $\text{Ba}_{7.0}\text{La}_{1.0}\text{Ga}_{17}\text{Ge}_{29}$  sample. Moreover, as the data is reproducible,  $\text{Ba}_{7.0}\text{La}_{1.0}\text{Ga}_{17}\text{Ge}_{29}$  becomes an excellent candidate for a good thermoelectric material. Further studies on the formation of Ln substituted compounds in various x along with measuring physical properties of hot-pressed samples are needed in the future work.

## Appendix A

Figure A.1 The electrical conductivity of  $\text{Ba}_{8-x}\text{Ln}_x\text{Ga}_{16}\text{Ge}_{30}$  and  $\text{Ba}_{8-x}\text{Ln}_x\text{Ga}_{16+x}\text{Ge}_{30-x}$ .

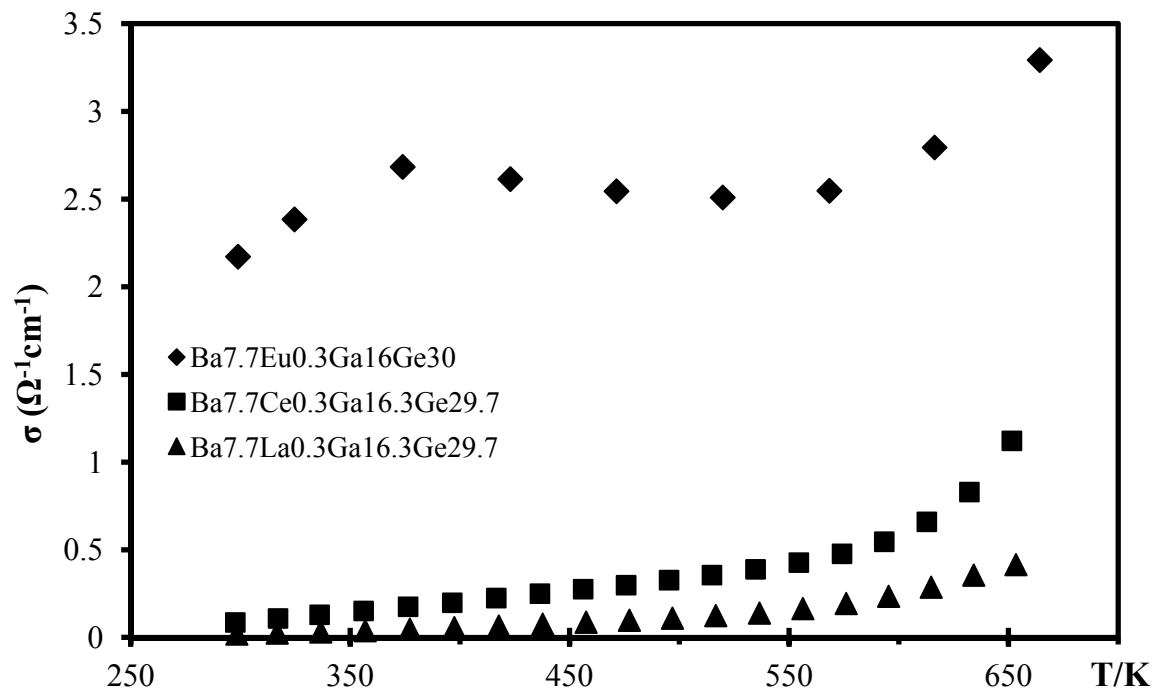


Figure A.2 The Seebeck coefficient of  $Ba_{8-x}Ln_xGa_{16}Ge_{30}$  and  $Ba_{8-x}Ln_xGa_{16+x}Ge_{30-x}$ .

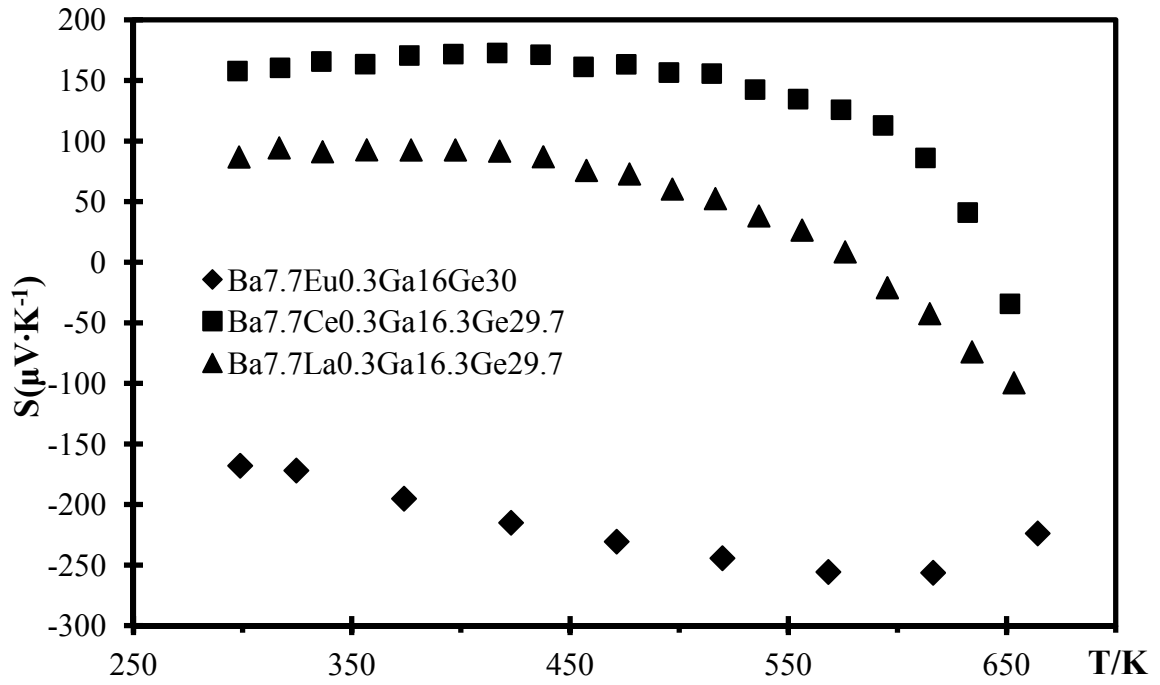
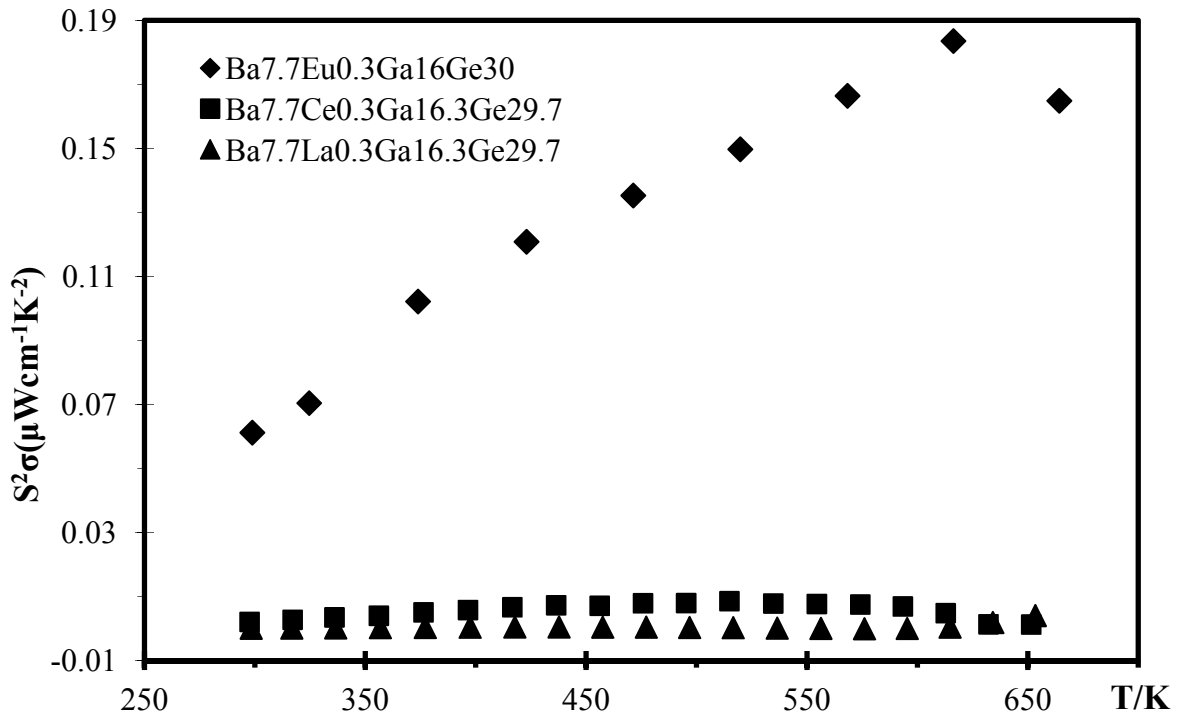


Figure A.3 The power factor of  $Ba_{8-x}Ln_xGa_{16}Ge_{30}$  and  $Ba_{8-x}Ln_xGa_{16+x}Ge_{30-x}$ .



## Bibliography

1. H. Kleinke. *Chem. Mater.* **22**, 604 (2010).
2. X. Shi, J. Yang, S. Bai, J. Yang, H. Wang, M. Chi, J. R. Salvador, W. Zhang, L. Chen, and W. Wong-Ng. *Adv. Funct. Mater.* **20**, 755 (2010).
3. X. Tang, P. Li, S. Deng, and Q. Zhang. *J. Appl. Phys.* **104**, 013706 (2008).
4. P. I. Ekwo, and C. E. Okeke. *Energy Convers. Mgmt.* **33**, 159 (1992).
5. B. Krys. *E-Futures* 1 (2010).
6. L. E. Bell. *Science* **321**, 1457 (2008).
7. G. J. Snyder, and E. S. Toberer. *Nat. Mater.* **7**, 105 (2008).
8. F. J. DiSalvo. *Science* **285**, 703 (1999).
9. B. C. Sales. *Science* **295**, 1248 (2002).
10. J. Yang, and T. Caillat. *MRS Bull.* **31**, 224 (2006).
11. NASA “*Space Radioisotope Power Systems – New Horizons Mission (Pluto)*,” U. S. Department of Energy (2008).
12. C. B. Vining. *Nat. Mater.* **8**, 83 (2009).
13. M. Christensen, S. Johnsen, M. Søndergaard, J. Overgaard, H. Birkedal, and B. B. Iversen. *Chem. Mater.* **21**, 122 (2009).
14. M. Falmbigl, G. Rogl, P. Rogl, M. Kriegisch, H. Müller, E. Bauer, M. Reinecker, and W. Schranz. *J. Appl. Phys.* **108**, 043529 (2010).
15. C. Gatti, L. Bertini, N. P. Blake, and B. B. Iversen. *Chem. Eur. J.* **9**, 4556 (2003).
16. H. Davy. *Philos. Trans. R. Soc. London*, **101**, 155 (1811).
17. A. K. Sum, C. A. Koh, and E. D. Sloan. *Ind. Eng. Chem. Res.* **48**, 7457 (2009).

18. L. Pauling. *J. Am. Chem. Soc.* **57**, 2680 (1935).
19. M. Christensen, S. Johnsen, and B. B. Iversen. *Dalton Trans.* **39**, 978 (2010).
20. B. A. Buffett. *Annu. Rev. Earth Planet. Sci.* **28**, 477 (2000).
21. A. A. Lacis, G. A. Schmidt, D. Rind, and R. A. Ruedy. *Science* **330**, 356 (2010).
22. K. A. Kvenvolden. *Chem. Geol.* **71**, 41 (1988).
23. D. A. Lashof, and D. R. Ahuja. *Nature* **344**, 529 (1990).
24. G. J. MacDonald. *Annu. Rev. Energy* **15**, 53 (1990).
25. Y. Mudryk, P. Rogl, C. Paul, S. Berger, E. Bauer, G. Hilscher, C. Godart, H. Noël, A. Saccone, R. Ferro. *Physica B* **328**, 44 (2003).
26. K. A. Kovnir and A. V. Shevelkov. *Russ. Chem. Rev.* **73**, 923 (2004).
27. J. R. Sootsman, D. Y. Chung, and M. G. Kanatzidis. *Angew. Chem. Int. Ed.* **48**, 8616 (2009).
28. A. A. Demkov, O. F. Sankey, K. E. Schmidt, G. B. Adams, and M. O'Keeffe. *Phys. Rev. B* **50**, 17001 (1994).
29. S. Paschen, V. Pacheco, A. Bentien, A. Sanchez, W. Carrillo-Cabrera, M. Baenitz, B. B. Iversen, Y. Grin, and F. Steglich. *Physica B.* **328**, 39 (2003)
30. J. Dong, O. F. Sankey, G. K. Ramachandran, and P. F. McMillan. *J. Appl. Phys.* **87**, 7726 (2000).
31. G. S. Nolas, J. L. Cohen, G. A. Slack, and S. B. Schujman. *Appl. Phys. Lett.* **73**, 178 (1998).
32. S. Bobev, and S. C. Sevov. *J. Solid State Chem.* **153**, 92 (2000).
33. M. A. Kirsanova, A. V. Olenov, A. M. Abakumov, M. A. Bykov, and A. V.

- Shevelkov. *Angew. Chem. Int. Ed.* **50**, 2371 (2011).
34. B. C. Chakoumakos, B. C. Sales, D. G. Mandrus, and G. S. Nolas. *J. Alloys Compd.* **296**, 80 (2000).
35. M. M. Shatruk, K. A. Kovnir, M. Lindsjl, I. A. Presniakov, L. A. Kloo, and A. V. Shevelkov. *J. Solid State Chem.* **161**, 233 (2001).
36. G. J. Miller, in *Chemistry, Structure, and Bonding of Zintl Phases and Ions*; S. M. Kauzlarich, Ed; VCH, New York 1 (1996).
37. W. -Q. Cao, Y. -G. Yan, X. -F. Tang, and S. -K. Deng. *J. Phys. D: Appl. Phys.* **41**, 215105 (2008).
38. A. Saramat, G. Svensson, A. E. C. Palmqvist, D. Platzek, D. M. Rowe, and G. D. Stucky. *J. Appl. Phys.* **99**, 023708 (2006).
39. I. Fujita, K. Kishimoto, M. Sato, H. Anno, and T. Koyanagi. *J. Appl. Phys.* **99**, 0093707 (2006).
40. E. S. Toberer, M. Christensen, B. B. Iversen, and G. J. Snyder. *Phys. Rev. B* **77**, 075203 (2008).
41. X. Hou, Y. Zhou, L. Wang, W. Zhang, W. Zhang, and L. Chen. *J. Alloys Compd.* **482**, 544 (2009).
42. V. L. Kuznetsov, L. A. Kuznetsova, A. E. Kaliazin, and D. M. Rowe. *J. Appl. Phys.* **87**, 7871 (2000).
43. N. L. Okamoto, K. Kishida, K. Tanaka, and H. Inui. *J. Appl. Phys.* **101**, 113525 (2007).
44. S. Deng, X. Tang, P. Li, and Q. Zhang. *J. Appl. Phys.* **103**, 073503 (2008).

45. K. Akai, T. Uemura, K. Kishimoto, M. Matsuura, and *et al.* *J. Electron. Mater.* **38** (7), 1412 (2009).
46. X. Yan, M. Falmbigl, S. Laumann, A. Grytsiv, E. Bauer, P. Rogl, and S. Paschen. *J. Electron. Mater.* **41** (6), 1159 (2012).
47. H. Anno, M. Hokazono, M. Kawamura, J. Nagao, and K. Matsubasa. *21<sup>st</sup> Int. Conf. on Thermoelectrics* 77 (2002).
48. J. D. Bryan, V. I. Srdanov, and G. D. Stucky. *Phys. Rev. B* **60** (5), 3064 (1999).
49. R. E. Dinnebier, and S. J. L. Billinge. *Powder Diffraction: Theory and Practice*; The Royal Society of Chemistry Publishing, Cambridge (2008).
50. B. C. Sales, B. C. Chakoumakos, D. Mandrus, and J. W. Sharp. *J. Solid State Chem.* **146**, 528 (1999).
51. J. L. Cohen, G. S. Nolas, V. Fessatidis, T. H. Metcalf, and G. A. Nolas. *Phys. Rev. Lett.* **82**, 779 (1999).
52. G. D. Mahan. in *Solid State Phys.* **51**, 81 (1998).
53. A. Bentien, A. E. C. Palmqvist, J. D. Bryan, S. Lattner, G. D. Stucky, L. Furenlid, and B. B. Iversen. *Angew. Chem. Int. Ed.* **39**, 3613 (2000).
54. S. B. Schujman, G. S. Nolas, R. A. Young, C. Lind, A. P. Wilkinson, G. A. Slack, R. Patschke, M. G. Kanatzidis, M. Ulutagay, and S. -J. Hwu. *J. Appl. Phys.* **87**, 1529 (2000).
55. S. Paschen, C. Gspan, W. Grogger, M. Dienstleder, S. Laumann, P. Pongratz, H. Sassik, J. Wernisch, and A. Prokofiev. *J. Cryst. Growth.* **310**, 1853 (2008).
56. A. Bentien, B. B. Iversen, J. D. Bryan, G. D. Stucky, A. E. C. Palmqvist, A. J.

- Schultz, and R. W. Henning. *J. Appl. Phys.* **91**, 5694 (2002).
57. L. -H. Li, L. Chen, J. -Q. Li, and L. Wu. *Chem. Mater.* **22**, 4007 (2010).
58. V. Pacheco, W. Carrillo-Cabrera, V. H. Tran, S. Paschen, and Y. Grin. *Phys. Rev. Lett.* **87** (9), 09960 (2001).
59. A. K. Cheetham and P. Day, *Solid-State Chemistry Techniques*; Oxford University Press, New York 45 (1987).
60. Inel, WPA manual
61. <http://www.crystalimpact.com/>
62. A. R. West, *Basic Solid State Chemistry*; John Wiley & Sons Ltd., New York 120 (1994).
63. L. E. Smart, and E. A. Moore. *Solid State Chemistry*; Chapman and Hall, London, UK. (1996).
64. D. M. Rowe, *Thermoelectrics Handbook: Macro to Nano*; CRC Press, Boca Raton, U. S. (2006).
65. H. M. Rietveld. *J. Appl. Cryst.* **2**, 65 (1969).
66. R. A. Young. *The Rietveld Method*; Oxford University Press, New York (2002).
67. G. Malmros, and J. O. Thomas. *J. Appl. Cryst.* **10**, 7 (1997).
68. L. Cranswick, and I. Swainson. *GSAS Rietveld Software Practicals*; 5<sup>th</sup> Canadian Powder Diffraction Workshop, Waterloo (2004).
69. L. C. Larson, and R. B. von Dreele. LANSCE, MSH805, Los Alamos National Laboratory, NM 87545, US. (1995).
70. B. Hafner. *Energy Dispersive Spectroscopy on the SEM: A Primer*; University of



Minnesota

71. T. Mu, Chem. *794 Research Proposal*, University of Waterloo (2008).
72. A. T. Petit, and P. L. Dulong, *Annal. Chim. Phys.* **10**, 395 (1819).
73. G. T. Woods, J. Martin, M. Beekman, R. P. Hermann, F. Grandjean, V. Keppens, O. Leupold, G. J. Long, and G. S. Nolas. *Phys. Rev. B* **73**, 174403 (2006).
74. J. Martin, H. Wang, and G. S. Nolas. *Appl. Phys. Lett.* **92**, 222110 (2008).
75. A. Bentien, E. Nishibori, S. Paschen, B. B. Iversen. *Phys. Rev.* **71**, 144107-1 (2005).
76. E. S. Toberer, A. F. May, and G. J. Snyder. *Chem. Mater.* **22**, 624 (2010).
77. G. A. Slack, in *CRC Handbook of Thermoelectrics*; D. M. Rowe, Ed.; CRC Press, Boca Raton, U. S. **146**, 528 (1999).
78. S. Kim, S. Hu, C. Uher, T. Hogan, B. Huang, J. D. Corbett, and M. G. Kanatzidis. *J. Solid State Chem.* **153**, 321 (2000).
79. G. S. Nolas, J. Sharp, and H. J. Goldsmid, in *Thermo-electrics: Basic Principles and New Materials Developments*; R. Hull, R. M. Osgood Jr., H. Sakaki, and A. Zunger, Ed.; Springer, Verlag Berlin Heidelberg, **45**, 91 (2001).